Axion search with high-energy gamma-ray observations

TAKAHASHI Haruki

Department of Particle and Nuclear Physics
School of High Energy Accelerator Science
The Graduate University for Advanced Studies, SOKENDAI

This dissertation is submitted for the degree of
Doctor of Philosophy

March 2026

Abstract

Dark matter is a massive and invisible piece in the Universe. Many candidates of dark matter have been developed beyond the Standard Model such as weakly interacting massive particles, primordial black holes, axions, and so on. Axion is a motivated candidate of dark matters and its searches are going on in several ways. Axion search with high-energy gamma-ray observations is an example. High-energy gamma rays are emitted from a source and undergo gamma-ray absorption and, if there exist axions, axion-photon conversions under magnetic fields in the Universe. This can alter the gamma-ray spectrum and have been used to constrain on axion mass and its coupling to photon. While one used gamma rays from extra-galactic sources to get information for axions, galactic objects such as pulsar wind nebulae (PWNe) have recently been used as sources for ALP search with gamma rays. For example, the Crab Nebula, one of the famous PWNe, was used to constrain on axions. However, effects of magnetic fields in the Crab Nebula on the axion-photon conversion have not been taken into account so far.

In this thesis, we derive new upper bounds on the coupling of axions with photon as a function of the mass by considering axion-photon conversion in the Crab Nebula. The magnetic field plays a crucial role through the Synchrotron Self-Compton (SSC) process, in which high-energy electrons produce synchrotron radiation that is subsequently upscattered by the same electrons via inverse Compton scattering to generate gamma rays. Therefore, neglecting the magnetic field in modeling leads to theoretical inconsistencies. We investigate the significance of the magnetic field effect and demonstrate that even differences in magnetic field modeling can substantially alter the conversion probability. We thus, for the first time, point out that proper consideration of the magnetic field is essential in axion searches using gamma rays from the Crab Nebula. The resulting constraints reach up to a coupling of $g_{a\gamma\gamma} \lesssim 1 \times 10^{-11}\mathrm{GeV}^{-1}$ for ALP masses in the range $10^{-10}\mathrm{eV} \lesssim m_a \lesssim 10^{-6}\mathrm{eV}$.

Contents

Chapter 1

Introduction

"What makes up the Universe?" This is one of the difficult questions, and we know some of its answers, namely elementary particles in the Standard Model (SM). We have observed three generations of the quarks and leptons, gauge bosons, and the Higgs particle in experiments. Their behavior can be mostly explained in the framework of the Standard Model. However, it still has some unresolved problems, such as neutrino masses, hierarchy problems, flavor puzzles, Higgs sector, and so on. Particle physicists have tried to solve these problems and go beyond the Standard Model. Dark matter also remains one of biggest questions as well as problems mentioned above not only for particle physicists but also for cosmologists and astrophysicists.

Dark matter is a massive and invisible piece in the Universe. Its existence is recognized through gravitational interaction and its coupling to ordinary matters is considered to be so weak. Fritz Zwicky said in 1937 that something massive and invisible should exist in order for a galaxy not to escape from its host galaxy [1]. In 1970's, observations of galaxy's rotational curves indicated the existence of dark matter. In 2001, Wilkinson Microwave Anisotropy Probe (WMAP) has observed cosmic microwave background (CMB), and then estimated energy density of baryons and dark matter. These measurements established the existence of dark matter. Nevertheless, we do not know who it is. A lot of dark matter candidates have been proposed and searched, for instance, weakly interacting massive particles (WIMPs), primordial black holes (PBHs), axions, and so on (e.g. [2]).

Axions are pseudo Nambu-Goldstone bosons appearing after an additional $U(1)_{\rm PQ}$ symmetry is spontaneously broken. It is a dynamical solution to the strong CP problem in quantum chromodynamics (QCD) [3, 4] and called QCD axions. QCD axions were soon found to work as dark matter in the Universe [5, 6], and models were developed such as KSVZ model [7, 8] and DFSZ model [9, 10] (see e.g. [11–13] for reviews). Axion-like

particles (ALPs) are a kind of generalizations of QCD axions and can be a candidate of dark matters. ALPs mass m_a and its coupling to photons $g_{a\gamma\gamma}$ do not have relations with each other as opposed to QCD axion whose mass is proportional to the coupling. ALPs appear in models beyond the Standard Model such as grand unified theories, higher-dimensional theories, and string theories [14–24] (e.g. [25–28] for reviews and lectures).

For axion searches (e.g. [29, 30] for reviews), photon is an important probe and couples to axions through the Chern-Simons coupling $-\frac{1}{4}g_{a\gamma\gamma}aF_{\mu\nu}\tilde{F}^{\mu\nu}$ where a is the axion field, $F_{\mu\nu}$ is the strength tensor of electromagnetic fields, and $\tilde{F}^{\mu\nu}$ is its dual. This coupling allows axions to convert into photons and vise versa. As proposed by Sikivie [31], helioscopes [32–42] and haloscopes [43–51] are experiments to look for axions from the Sun and axion dark matter in the galactic halo, respectively. CERN Axion Solar Telescope (CAST) [32–39] is one of helioscopes to detect solar axions produced in the core of the Sun through the Primakoff process. CAST has given upper bounds on the axion-photon coupling $g_{a\gamma\gamma} < 6.5 \times 10^{-11}\,\mathrm{GeV}^{-1}$ [39]. Axion Dark Matter eXperiment (ADMX) [43–50] is a haloscope to look for dark matter axions in our galactic halo within the mass range 2.66 to 3.1 μeV. It is able to explore models of the QCD axions such as the KSVZ model and the DFSZ model. Light-shining through a wall (LSW) experiments [52–55] such as Any Light Particle Search (ALPS) [52, 53] and ALPS II [54] have constrained axion parameters as well as the helioscopes and the haloscopes.

In addition to these experiments, observations of celestial objects also give us a hint for axions [56–84] ([85, 86] for a recent review). For example, gamma-ray observations are ways to get information of axions [60, 87–144] ([145–147] for recent reviews) as follows. High-energy gamma rays emitted from a source are absorbed by low-energy background photons, and can be converted to axions and vise versa under magnetic fields in the Universe. The gamma-ray absorption and the axion-photon conversion can alter gamma-ray spectra and give constraints on the axion mass m_a and the axion-photon coupling $g_{a\gamma\gamma}$. While extragalactic objects such as blazars and radio galaxies have been used for axion searches and given constraints on axion parameters (e.g. [132–138]), galactic sources including supernova remnants (SNRs) and pulsar wind nebulae (PWNe) have also been recently used in a similar way [139–144], such as the Crab Nebula [142–144]. The Crab Nebula is the brightest pulsar wind nebula in the Milky Way (MW) and powered by relativistic electron-positron wind from the Crab Pulsar at the center. Electromagnetic waves from the Crab Nebula have been observed in broad energy range from radio to gamma rays [132, 148–156]. These data sets allowed for developing emission models for the Crab Nebula (e.g. [157–159]).

When we use observations of gamma rays from some astrophysical sources for axion

searches, it is important to consider astrophysical models of magnetic fields precisely as far as possible. This is because magnetic fields affect on the axion-photon conversion and then the axion constraints with the gamma-ray observations. In this thesis, we investigate how the magnetic fields in the Crab Nebula affect on the axion-photon conversion. This effect has not been taken into account in the axion search with gamma rays from the Crab Nebula so far. As explained in Section 4.2, we consider a model for the magnetic field discussed in [159]. The magnetic field is important not only in the axion-photon conversion but also in photon emission process in the Crab Nebula, called the synchrotron self-Compton (SSC) process which will also be explained in Section 4.2. We find that this consideration significantly affects on the axion-photon conversion and then alter the resulting constraint on the axion parameters m_a and $g_{a\gamma\gamma}$. Finally, we obtain new constraints reaching down to $g_{a\gamma\gamma} \lesssim 1 \times 10^{-11}\,\mathrm{GeV}^{-1}$ at $m_a \simeq 10^{-8}\,\mathrm{eV}$ and exceeding the constraints by CAST in the axion mass range $10^{-10}\,\mathrm{eV} \lesssim m_a \lesssim 10^{-6}\,\mathrm{eV}$.

This thesis is organized as follows. In Chapter 2, we first review general properties of dark matter and briefly overview several candidates such as WIMPs and PBHs with their detection ideas. Chapter 2 also introduces the Peccei-Quinn mechanism and some models to realize it, accompanied by existing axion constraints by experiments and observations including the axion helioscopes, haloscopes and so on. We next discuss a framework where one explores axions with gamma-ray observations from astrophysical objects and then give some specific examples of existing axion limits obtained from observations of extragalactic and galactic sources in Chapter 3. It makes us understood background knowledge most relevant to the main contents of this thesis. In Chapter 4, we discuss emission models and magnetic fields of the Crab Nebula, and investigate their effects on axion search with gamma-ray observations of the Crab Nebula. Chapter 5 is devoted to the conclusion of the thesis.

Chapter 2

Dark Matter

In Chapter 2, we first introduce observational evidences and general properties of dark matter in Section 2.1. Section 2.2 shows brief overview of several dark matter candidates such as WIMPs and PBHs. Since axions are main topics of this thesis, Section 2.3 is devoted to discuss a theoretical motivation of axions, followed by their detection ideas such as axion haloscopes, helioscopes, and LSW experiments in Section 2.4. Section 2.5 summarizes this chapter.

2.1 Dark matter properties

2.1.1 Observational evidences

Zwicky's insight

In virial theorem, kinetic energy $E_{\rm kin}$ and potential energy $E_{\rm pot}$ of a dynamical system have a relation

$$\langle E_{\rm kin}\rangle = -\frac{1}{2}\langle E_{\rm pot}\rangle. \tag{2.1}$$

This is applicable to a galaxy cluster with mass M and radius R. $E_{\rm kin}$ and $E_{\rm pot}$ are then written as

$$\langle E_{\rm kin}\rangle = \frac{1}{2}M\langle v^2\rangle, \tag{2.2}$$

$$\langle E_{\rm pot}\rangle = -\frac{3}{5}\frac{GM^2}{R}, \tag{2.3}$$

assuming the density of the galaxy cluster is spherically homogeneous in order to get $\langle E_{\rm pot}\rangle$. From Eq. (2.1), the mass of the galaxy cluster is

$$M = \frac{5}{3}\frac{\langle v^2\rangle R}{G}. \tag{2.4}$$

Substituting observational values $\langle v^2\rangle^{1/2} \sim 1000\,\mathrm{km/s}$, $R \sim 10^{24}\,\mathrm{cm}$ and $G = 6.67 \times 10^{-8}\,\mathrm{cm^3 g^{-1} s^{-2}}$ into Eq. (2.4) find

$$M \sim 1.3 \times 10^{14} M_\odot \tag{2.5}$$

where $M_\odot \simeq 2 \times 10^{33}\mathrm{g}$ is the mass of the Sun. We can also estimate the galaxy cluster's mass $M_{\rm lum}$ under an assumption that it only includes shining galaxies. Averaged luminosity of galaxies in the galaxy cluster is $L_{\rm gal} \sim 10^9 L_\odot$ from observations. If the luminosity is composed of stars as massive as the Sun, a ratio of galaxy mass $M_{\rm gal}$ and luminosity becomes $(M_{\rm gal}/M_\odot)/(L_{\rm gal}/L_\odot) \sim 1$, and $M_{\rm lum}$ is given by

$$\begin{aligned} M_{\rm lum} &\sim 800 M_\odot \left(\frac{L_{\rm gal}}{L_\odot}\right)\left(\frac{M_{\rm gal}/M_\odot}{L_{\rm gal}/L_\odot}\right) \\ &\sim 8 \times 10^{11} M_\odot. \end{aligned} \tag{2.6}$$

This is much less than the mass M dynamically determined with virial theorem (Eq. (2.5)) so that Fritz Zwicky concluded that there should exist massive and invisible dark matter within the galaxy cluster [1].

Rotation curves of galaxies

Observing galactic rotation curves is an evidence to indicate the existence of dark matter in galactic scale. We live in the Milky Way (MW) which is a typical spiral galaxy. The solar system is located at a distance $\sim 8.5\,\mathrm{kpc}$ from the center of the MW. Stars and gas extend to a distance $\sim 10\,\mathrm{kpc}$ and are rotating around the MW. Their rotational speed $v(r)$ is roughly described as

$$v(r) = \sqrt{\frac{GM(r)}{r}} \tag{2.7}$$

where r is the distance from the center of the galaxy and $M(r)$ is total mass within the radius r. Eq. (2.7) implies that $M(r)$ becomes constant if the visible stars and gas are account for almost all of the galaxy mass and $v(r)$ decrease as $r^{-1/2}$ outside the MW.

However, observations have shown that this expectation was incorrect. Galactic rota-

tion curves become flat even far from the center of a galaxy. In Fig. 2.1, rotation curves of several galaxies are displayed. The observations indicate that something invisible should be distributed as $M(r) \propto r$ and dominant compared to visible components for $r \gtrsim 15\,\mathrm{kpc}$. This indicates that the existence of dark matter is universal in galactic scale.

Observations of galaxy clusters

Galaxy clusters are the largest gravitationally bound structures in the Universe and contains hundreds to thousands of galaxies. It is known that these galaxies are located within hot and X-ray emitting gas which makes galaxy clusters one of the brightest X-ray sources in the Universe. X-ray telescopes have observed galaxy clusters and found that the total mass inferred by the observations is larger than one obtained by sum of the baryonic components, namely galaxies and gas.

Considering spherical and hydrostatic equilibrium, gas pressure $p(r)$ and density $\rho(r)$ satisfies

$$\frac{\mathrm{d}p}{\mathrm{d}r} = -\frac{GM(r)\rho(r)}{r^2} \tag{2.8}$$

where $M(r)$ is the total mass within a radius r. This equation is used to infer the total mass M of the cluster as follows. With the following equation of state

$$p(r) = \frac{k_B T(r)\rho(r)}{\mu m_p}, \tag{2.9}$$

Eq. (2.8) becomes

$$\frac{k_B T(r)\rho(r)}{\mu m_p}\left(\frac{1}{\rho(r)}\frac{\mathrm{d}\rho}{\mathrm{d}r} + \frac{1}{T(r)}\frac{\mathrm{d}T}{\mathrm{d}r}\right) = -\frac{GM(r)\rho(r)}{r^2} \tag{2.10}$$

where $T(r)$ is the temperature profile of the gas, μ is the average molecular weight, and m_p is the proton mass. The total mass of the cluster is estimated as

$$M(r) = \frac{k_B T(r) r}{G\mu m_p}\left(-\frac{\mathrm{d}\ln\rho}{\mathrm{d}\ln r} - \frac{\mathrm{d}\ln T}{\mathrm{d}\ln r}\right), \tag{2.11}$$

indicating that profiles of the gas temperature $T(r)$ and density $\rho(r)$ determines the total mass $M(r)$. Assuming that the cluster has almost uniform distribution for temperature ($T(r) \sim T$) and its value is typically $10\,\mathrm{keV}$, the total mass is given by

$$M(r) \sim 10^{15} M_\odot \left(\frac{r}{\mathrm{Mpc}}\right)\left(\frac{T}{\mathrm{keV}}\right). \tag{2.12}$$

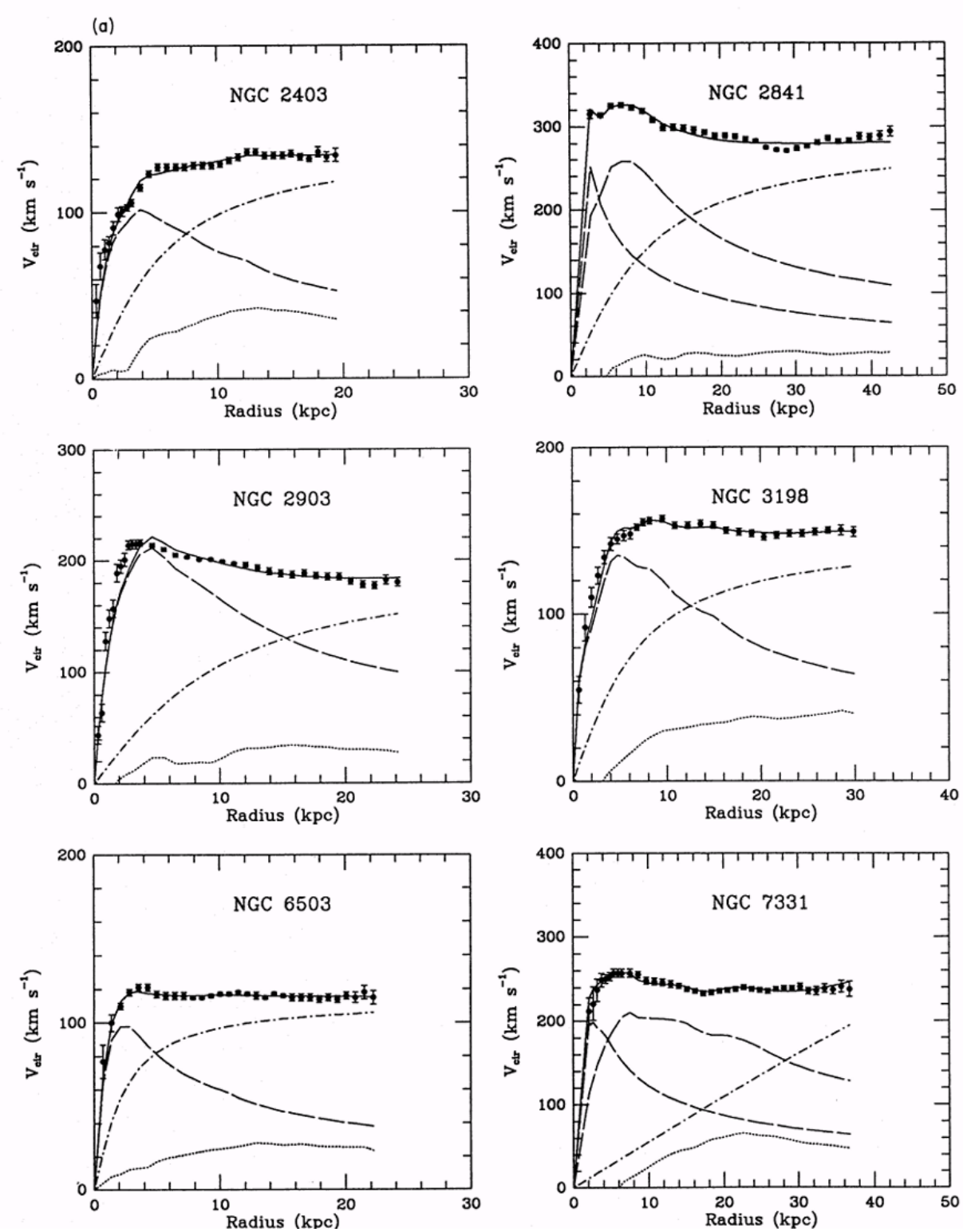

Figure 2.1: Rotation curves of several galaxies. The dashed (dotted) curves show the visible (gas) components while the dash-dotted curves correspond to the dark matter halo. Figure from [160].

The mass of the baryonic components is smaller than the value. This is a dark matter evidence in the scale of galaxy clusters.

CMB observations

We can also obtain information of dark matter from observations of cosmic microwave backgrounds (CMB). CMB temperature anisotropy is given by

$$\delta T(\theta, \phi) = T(\theta, \phi) - \bar{T} \tag{2.13}$$

in a position (θ, ϕ) on the sky. It can be expanded as

$$\frac{\delta T}{T}(\theta, \phi) = \sum_{l,m} a_{l,m} Y_{l,m}(\theta, \phi) \tag{2.14}$$

with spherical harmonic functions $Y_{l,m}$. The spherical harmonic coefficients $a_{l,m}$ define angular power spectrum

$$C_l = \langle |a_{l,m}|^2 \rangle = \frac{1}{2l+1} \sum |a_{l,m}|^2. \tag{2.15}$$

We can theoretically calculate the angular power spectrum C_l. The resulting prediction depends on cosmological parameters such as the baryon density Ω_b, the dark matter density $\Omega_{\rm DM}$, and other parameters. Precise measurements of the angular power spectrum allow us to fit them to the theoretical prediction and determine the values of these cosmological parameters. For example, the density parameters for dark matter and baryon were given as

$$\Omega_{\rm DM} h^2 = 0.120 \pm 0.001 \tag{2.16}$$

$$\Omega_b h^2 = 0.0224 \pm 0.0001 \tag{2.17}$$

based on CMB observation by Planck collaboration. Here, h is dimensionless Hubble parameter

$$h \equiv \frac{H_0}{100\,\mathrm{km/s/Mpc}} = 0.674 \pm 0.005 \tag{2.18}$$

with observational value of the Hubble parameter

$$H_0 = (67.4 \pm 0.5)\,\mathrm{km/s/Mpc}. \tag{2.19}$$

It is found that $\Omega_{\rm DM} \simeq 0.26$ and $\Omega_b \simeq 0.049$. This indicates that the Universe is fulled

with dark matter whose amount is roughly five times larger than ones of baryons.

general properties

Observations have revealed that the existence of dark matter at various scales in the Universe, as we have seen. Let us next review conditions which a dark matter candidate should satisfy. Dark matter should be

- stable, or long-lived than the Universe if unstable
- neutral and invisible
- cold (non-relativistic)
- weakly interacting with itself and ordinary matters

We have been looking for dark matter fulfilling the properties to explain observational evidences now that there exist a lot of dark matter candidates. Fig. 2.2 shows dark matter candidates (or frameworks) and their motivated mass scales span from 10^{-22} eV to solar mass scales. From the next section, we will discuss several dark matter candidates.

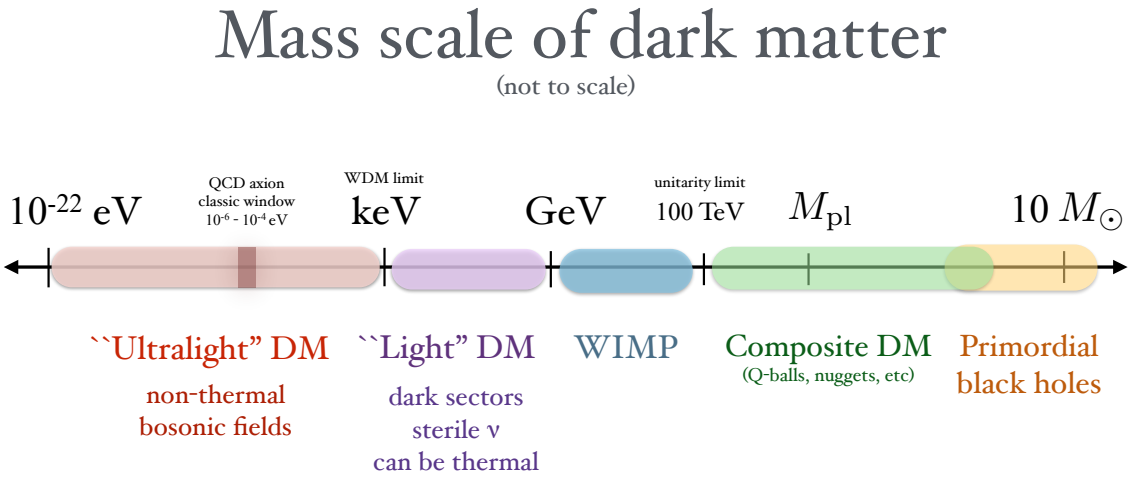

Figure 2.2: Dark matter candidates and their mass scales. Figure taken from [161].

2.2 Dark matter candidates

In Section 2.1, we have seen that the existence of dark matter is implied by various observations such as galaxy rotation curves, galaxy clusters, CMB temperature anisotropy and so on. These observations encourage us to explore dark matter and understand what it is. In Section 2.2, we introduce some candidates of dark matter such as WIMPs and PBHs with their characteristic properties and observational constraints.

2.2.1 Weakly interacting massive particles

It would be great if we have a dark matter candidate in the SM. Neutrinos were first investigated as a dark matter candidate but it is now known that they cannot account for all amount of dark matter in the Universe. In order to find a candidate of dark matter, one can try to go beyond the SM such as introducing supersymmetry, extra-dimension, and so on. WIMPs are one of the well-studied dark matter candidates, and an example is considered, for instance, along with supersymmetry which is the symmetry between bosons and fermions. Supersymmetric extensions of the SM have superpartners corresponding to the SM fermions and bosons, such as scalar quarks, scalar leptons, gauginos, Higgsinos and so on. Supersymmetry has been discussed as a remedy of so-called gauge hierarchy problem, one of the unresolved problems in the SM. In addition, supersymmetric grand unified theory indicate unification of gauge couplings in the SM.

These have motivated supersymmetry which can also give a dark matter candidate. For example, Bino, Wino, and Higgsinos can mix with each others and are called neutralinos. R-parity conservation is considered in the minimal supersymmetric extension of the SM. The SM particles are R-parity even while their superpartners are R-parity odd. This indicates that unstable supersymmetric particles decay to some supersymmetric particles, meaning that the lightest supersymmetric particle (LSP) should be stable and can become a candidate of dark matter. The lightest neutralino can be LSP, for instance. These supersymmetric particles can be thermally produced in early Universe. Freeze out mechanism is a possibility of WIMPs to explain all amount of dark matter. WIMPs have been searched in direct and indirect ways, or with colliders. We will give an overview of indirect detections with gamma rays, neutrinos, and other cosmic rays below.

Indirect detection with gamma rays

Gamma ray is an important probe in indirect detections and can be produced, for instance, by pair annihilation of WIMPs χ into photons γ where $\chi + \chi \to \gamma + \gamma$. Naively, we expect

line emission of gamma rays at WIMP's mass m_χ. However, gamma-ray signals originated from pair annihilation can appear as gamma-ray spectra with a cutoff $E_c \sim m_\chi$ because they can also be produced as secondary particles from hadrons and leptons produced primally by WIMPs. Gamma-ray flux is given by

$$\Phi_\gamma(E_\gamma) = \frac{\langle \sigma v \rangle}{m_\chi^2} \frac{\mathrm{d}N_\gamma}{\mathrm{d}E_\gamma} \cdot \mathcal{J}, \tag{2.20}$$

$$\mathcal{J} = \int d\Omega \int_{\text{l.o.s.}} ds\, \rho_\chi^2 \tag{2.21}$$

where $\langle \sigma v \rangle$ is the average of the cross section for pair annihilation process σ times relative velocity v, $\mathrm{d}N_\gamma/\mathrm{d}E_\gamma$ is the spectrum of a gamma ray in a pair annihilation process, ds is the integration over distance in a line of sight (l.o.s.), and $d\Omega$ is unit solid angle. While $\mathcal{J}$ factor is determined by dark matter distribution of a source, the other part of Eq. (2.21) can be characterized by WIMP's properties as particles.

The center of a galaxy can be a target for the indirect detection with gamma rays because regions denser with dark matters can emit more gamma rays with pair annihilation. However, there exist many sources of gamma rays as astrophysical backgrounds around the center of a galaxy. Also, dark matter distribution in the center of a galaxy has a lot of uncertainties. Simulations indicate that the distribution is given by the Navarro-Frenk-White (NFW) profile

$$\rho_{\text{DM}}(r) = \frac{4\rho_s}{(r/r_s)(1 + r/r_s)^2} \tag{2.22}$$

where $r_s \sim 20\,\text{kpc}$ for the MW and ρ_s is the density at r_s. We can obtain ρ_s by matching $\rho_{\text{DM}}(r)$ with the observed density around the Sun $\rho_\odot \sim 0.3\,\text{GeV}\,\text{cm}^{-3}$. Baryons may make the distribution around the galactic center flatter if the galaxy has a lot of baryons. In order to avoid these kinds of astrophysical backgrounds and uncertainties as far as possible, one can use dwarf galaxies as better targets for indirect detections. For example, dark matter searches with dwarf spheroidal galaxies have been conducted by several groups for gamma-ray observations, such as Fermi-LAT, Major Atmospheric Gamma-ray Imaging Cherenkov (MAGIC) telescopes, High Energy Stereoscopic System (H.E.S.S.), Very Energetic Radiation Imaging Telescope Array System (VERITAS) (e.g. [162]). Fig. 2.3 shows recent results of their combined analyses to put upper limits on $\langle \sigma v \rangle$ as a function of the dark matter mass for seven annihilation channels.

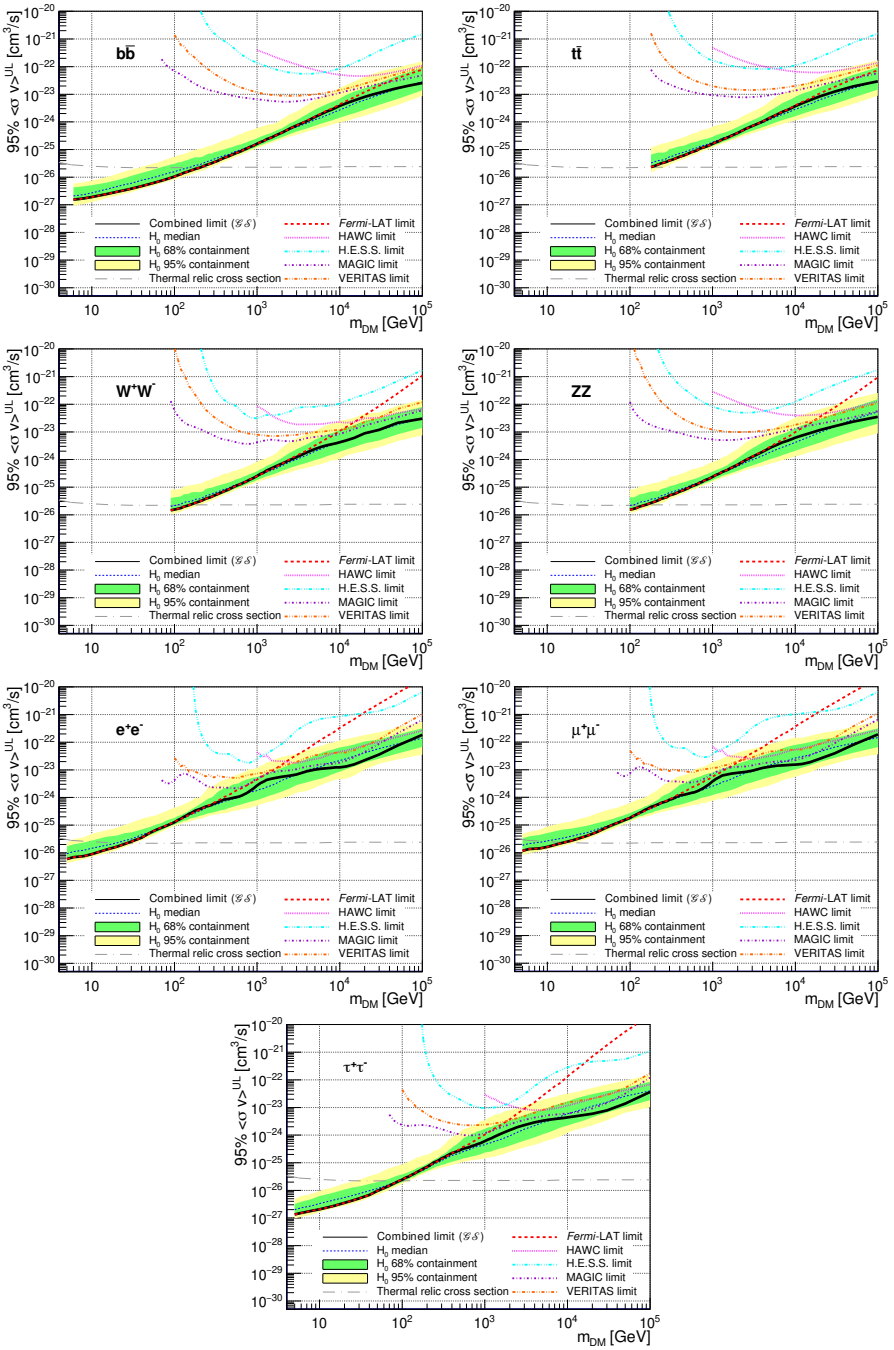

Figure 2.3: Upper limits at 95% confidence level (C.L.) on $\langle\sigma v\rangle$ for seven annihilation channels. The black solid line represents the observed combined results obtained for 20 dwarf spheroidal galaxies. The green and yellow bands are the 68% and 95% containment bands. The blue dashed line shows the median of the null hypothesis. This figure includes individual upper limits set by each gamma-ray experiments. The horizontal gray dotted-dashed line corresponds to the value of the thermal relic cross section. Figure taken from [162].

Indirect detection with neutrinos

Neutrinos can also be a hint for WIMP searches. WIMPs in the halo can collide with matters in stars and planets such as the Sun and the Earth. Then, they can be gravitationally captured and their density increases in the center of the astrophysical objects. Annihilation processes occurs and produce many particles including neutrinos which can escape from the Sun or the Earth. Observing such neutrinos can be indirect hints or hopefully evidence of WIMPs. For example, IceCube experiment have observed the Sun and the Earth and then given constraints on spin-dependent and spin-independent cross section of WIMPs with protons or nucleons [163, 164]. While limits with direct experiments generally surpass IceCube ones for spin-independent case (Figs. 2.5 and 2.6), IceCube put stronger constrains on spin-dependent cross sections in higher mass scale (Fig. 2.4).

Indirect detection with positrons

Observing positrons is a good way for indirect detections. Since the Universe is fulled with matters rather than anti-matters, positrons may be observed as excess compared with expectations by astrophysical models. High-energy electrons and positrons lose their energy through synchrotron process and inverse-Compton (IC) scattering after pair annihilation of dark matters. We could observe the positrons produced inside the Milky Way (MW). As shown in Fig. 2.7, observations of positrons (and also electrons) have been performed with balloons and recently with space air-crafts such as the Fermi-LAT, Alpha Magnetic Spectrometer (AMS) and so on [165]. They reported excesses in positron flux. However, the observed excess may have astrophysical origins, such as accelerated electrons and positrons produced by pulsars.

Indirect detection with anti-protons

Not only positrons but also anti-protons have been observed by the AMS. Anti-protons $\bar{p}$ can be produced secondly by a process $p + p \to p + p + p + \bar{p}$ where cosmic-ray protons p collide with interstellar medium. WIMPs can also produce protons p and anti-protons $\bar{p}$ through their pair annihilation. This could be observed as anti-proton excess over expectations of secondly anti-protons. Fig. 2.8 shows expected anti-proton spectra produced by WIMP's annihilation in addition to secondly flux as background [166]. Observational data is slightly exceeding the background around 10 GeV and this excess might be explained by assuming additional contributions are coming from WIMPs whose mass is about 50 GeV. However, we still have uncertainties for calculations of secondly anti-protons. This does not allow us to get statistically significant results yet.

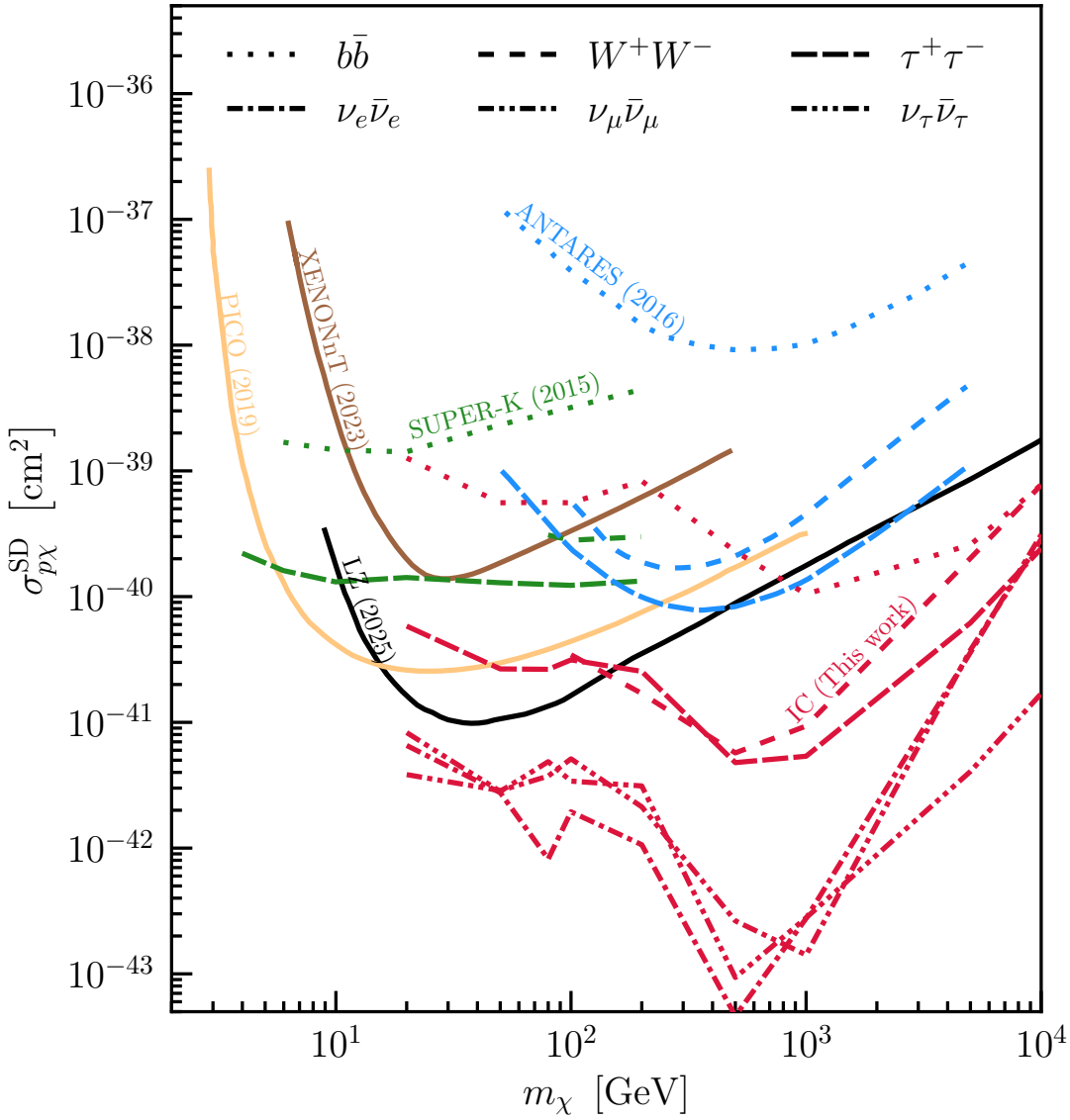

Figure 2.4: Limits on the spin-dependent WIMP-proton cross section. Solid lines are limits by direct detection experiments while other-type lines show ones by indirect detection experiments ([164] and references therein). For indirect ones, each line style corresponds to different annihilation channel. The IceCube experiment used ten-years datasets observing neutrinos from the Sun. Figure taken from [164].

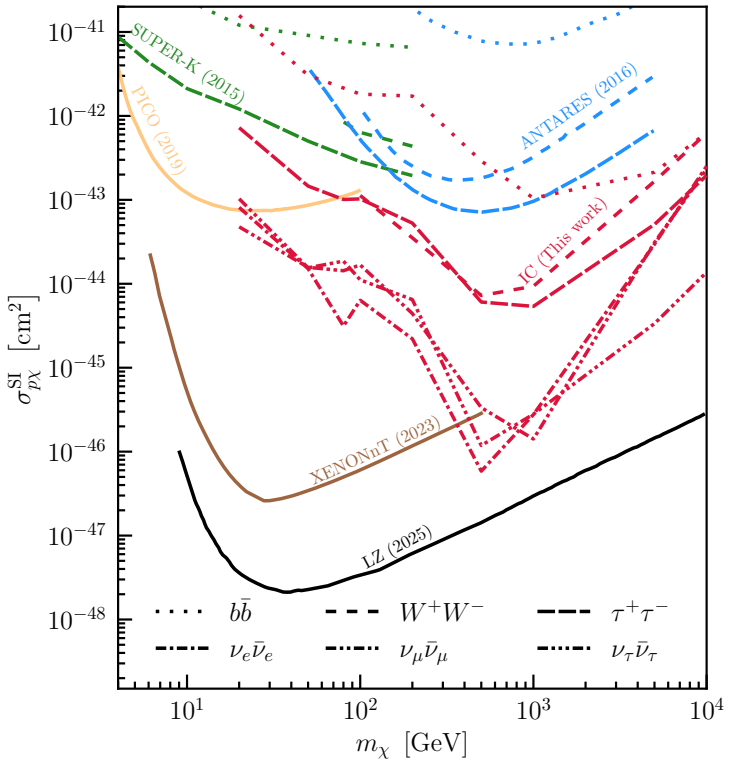

Figure 2.5: Same as Fig. 2.4 but on the spin-independent WIMP-proton cross section. Figure taken from [164].

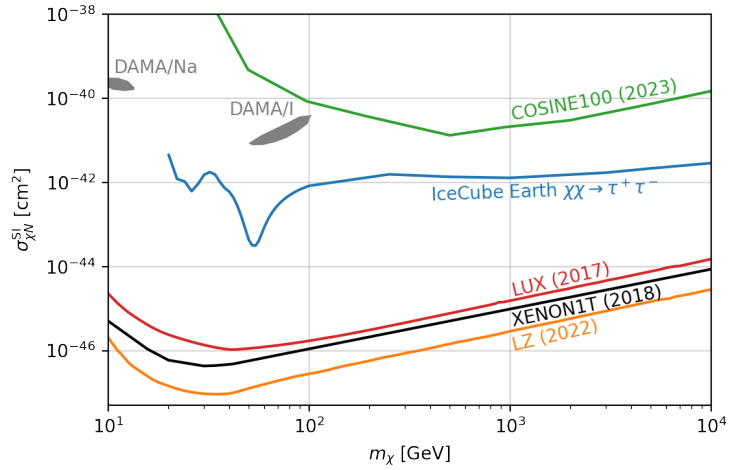

Figure 2.6: Limits on the spin-independent WIMP-nucleon cross section. Ten-years IceCube observations of the Earth put upper bounds (blue) for $\chi + \chi \to \tau^+ + \tau^-$ channel. Other lines show upper limits obtained from direct experiments. Figure taken from [163].

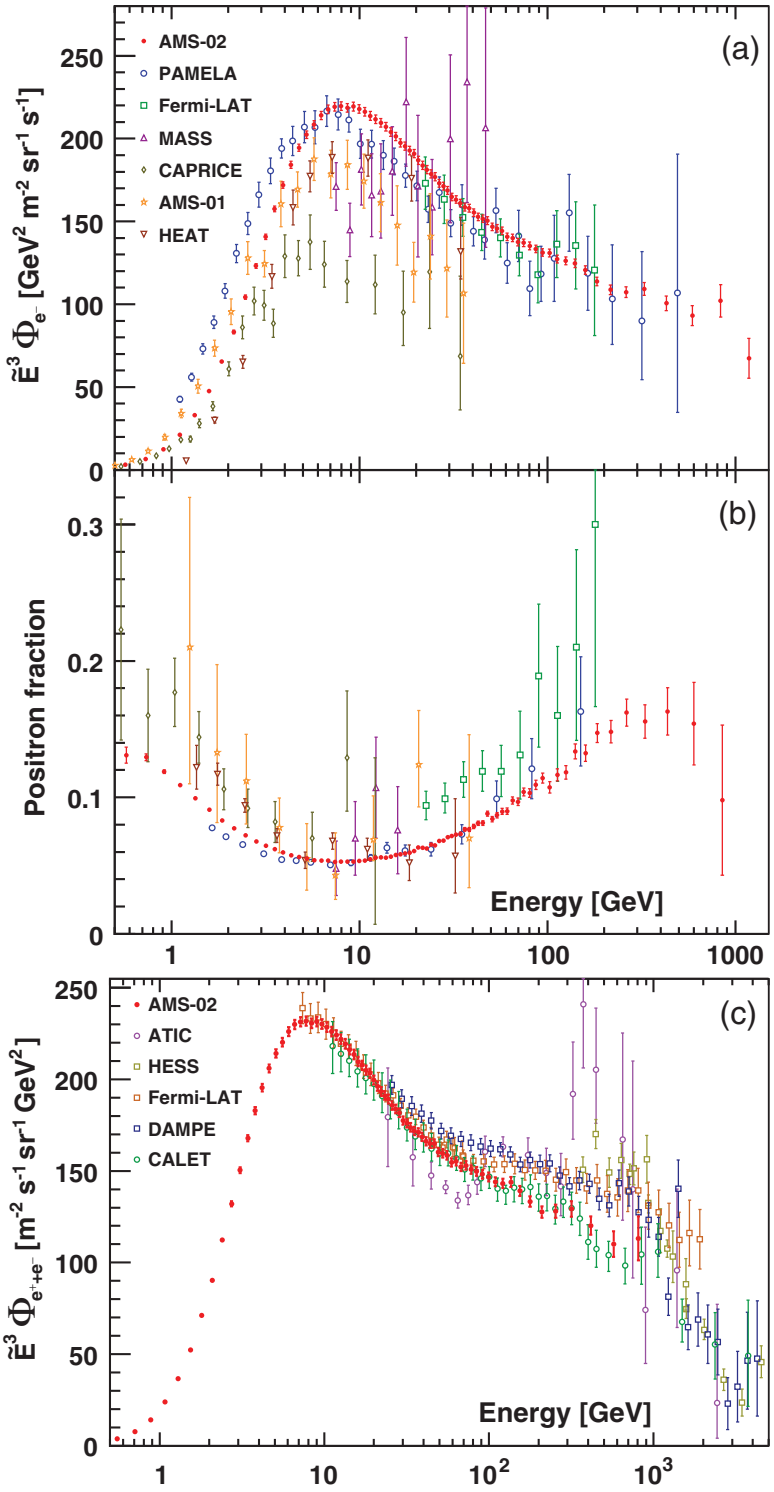

Figure 2.7: The top panel shows the electron spectrum observed by the AMS, the PAMERA, the Fermi-LAT, and so on ([165] and references therein). The middle panel represents positron fraction and the bottom one is the sum of electron and positron spectra. The Figure taken from [165].

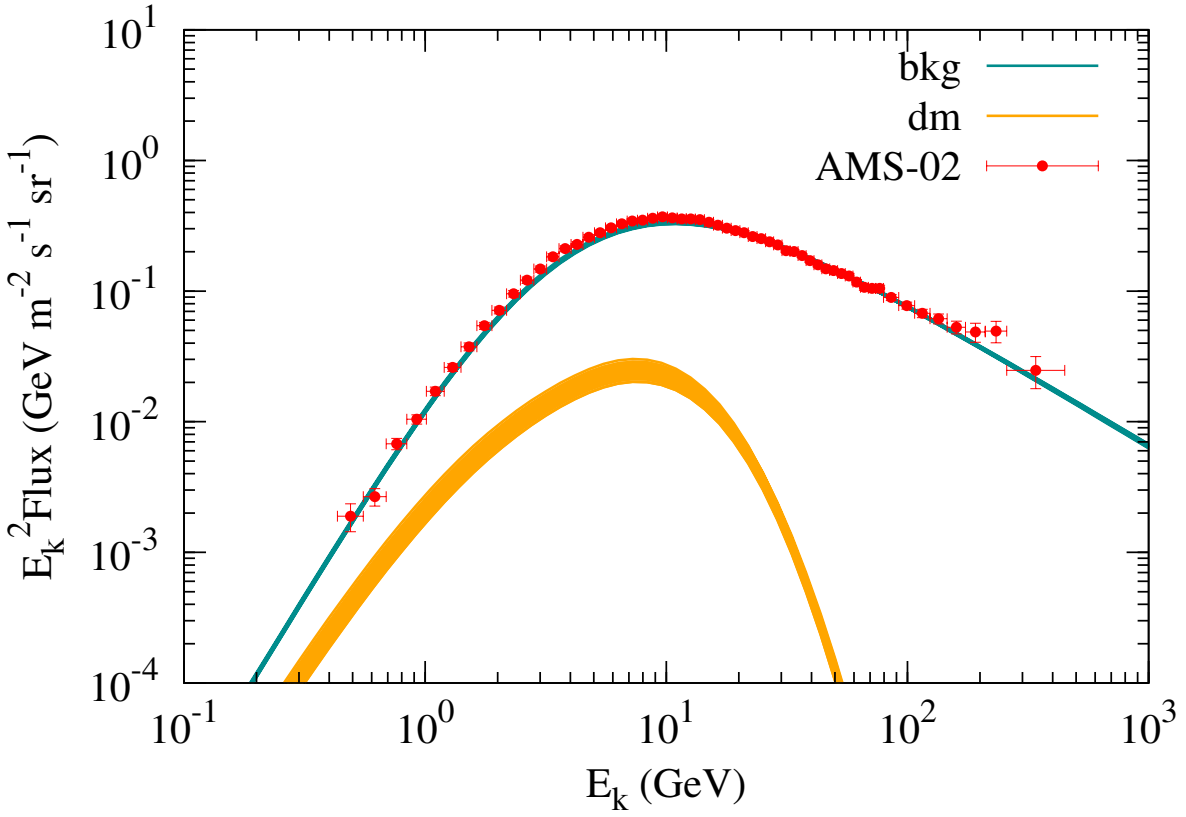

Figure 2.8: Anti-proton fluxes produced dark matter annihilation and its background with 2σ ranges of various background parameters derived in the background fitting. For illustration, the mass of the dark matter is set to be 47 GeV and the cross section is $10^{-26}\,\mathrm{cm^3 s^{-1}}$ for $b\bar{b}$ annihilation channel. Figure taken from [167].

2.2.2 Primordial black holes

PBHs have been discussed from various aspects and can be account for all portion of dark matter in some PBH mass range. PBHs can form in some ways and then evaporate as Hawking pointed out. One can constrain PBHs by observations such as gamma-ray observations, big bang nucleosynthesis (BBN), lensing and so on.

PBHs formation and evaporation

If large density fluctuations exist in the early Universe, they can collapse into PBHs. PBHs are different from black holes astrophysically produced in the end of stellar evolutions. The PBH mass M is determined by when it is produced. When wavelength of the fluctuations enter in the cosmological horizon, the density fluctuations $\delta(=\rho(\boldsymbol{x})/\bar{\rho}-1)$ exceeding a threshold value δ_c and then matters and radiations in the horizon gravitationally collapse into black holes. Here, $\rho(\boldsymbol{x})$ is the density fluctuations in co-moving coordinates $\boldsymbol{x}$ and $\bar{\rho}$ is spatially averaged density fluctuations. Considering Fourier-transformed density fluctuations $\delta(\boldsymbol{k})$ with the wavenumber $\boldsymbol{k}$, the Fourier mode enters the horizon when its wavelength $2\pi(a/a_0)k^{-1}$ becomes comparable with the horizon scale. At the horizon entering, the wavenumber ($k = |\boldsymbol{k}|$) is given by

$$\begin{aligned} k &= \frac{a}{a_0}H = \frac{g^1_{s*0}/3T_0^3}{g^1_{s*}/3T^3}H = \frac{g^1_{s*0}/3T_0^3}{g^1_{s*}/3T^3}\left(\frac{1}{3M_{\rm pl}\frac{\pi^2}{30}g_*T^4}\right)^{\frac{1}{2}} \\ &= g_{s*0}^{1/3}g_{s*}^{1/6}\left(\frac{\pi^2}{90}\right)^{\frac{1}{2}}\frac{TT_0}{M_{\rm pl}} \end{aligned} \tag{2.23}$$

where we have used $g_{s*}T^3a^3 = g_{s*0}T_0^3a_0^3$.

The PBH mass M correspond to a mass of radiations in the horizon called a horizon mass M_H. The horizon mass M_H is given by

$$M_H = \frac{4\pi}{3}\rho_R H^{-3} = \frac{4\pi}{3}\rho_R\left(\frac{8\pi G}{3}\rho_R\right)^{-3} = \frac{4\pi^3 g_*T^4}{90}\left(\frac{\pi^2 g_*T^4}{90M_{\rm pl}^2}\right)^{-\frac{3}{2}} \tag{2.24}$$

where H is the Hubble parameter, ρ_R is the density of radiations and g_* is the degrees of freedom of relativistic particles. With a parameter γ describing the difference between

the PBH mass and horizon mass, the PBH mass is expressed as

$$M = \gamma M_H \simeq 6 \times 10^{35}\,\mathrm{g} \left(\frac{\gamma}{0.2}\right) \left(\frac{g_*}{10.75}\right)^{-\frac{1}{2}} \left(\frac{T}{10\,\mathrm{MeV}}\right)^{-2} \tag{2.25}$$

$$\simeq 8 \times 10^{35}\,\mathrm{g} \left(\frac{\gamma}{0.2}\right) \left(\frac{g_*}{10.75}\right)^{-\frac{1}{6}} \left(\frac{k}{10^5\,\mathrm{Mpc}^{-1}}\right)^{-2} \tag{2.26}$$

where we used Eq. (2.23) in the last line.

As Hawking pointed out, black holes radiate particles and evaporate. Hawking temperature T_{BH} is important for discussing the evaporation of black holes and given by

$$T_{\mathrm{BH}} = \frac{1}{8\pi G M} \simeq 100\,\mathrm{eV} \left(\frac{M}{10^{20}\,\mathrm{g}}\right)^{-1}. \tag{2.27}$$

Approximating that black holes radiate particles as black bodies at T_{BH}, radiated energy follow Stefan-Boltzmann law

$$\frac{\mathrm{d}E}{\mathrm{d}t} = \frac{\pi^2}{120} g(M) T^4 (4\pi r_s^2) = \frac{\pi}{480} g(M) \frac{1}{(8\pi G M)^2} \tag{2.28}$$

where g is degrees of freedom of the radiated particles whose contributions are coming from particles lighter than the Hawking temperature. This reduces a mass of a black hole as $\mathrm{d}M/\mathrm{d}t = -\,\mathrm{d}E/\mathrm{d}t$. We can get the life time of the black hole

$$\tau \simeq 10240\pi g^{-1}(M) G^2 M^3 = 1.7 \times 10^{20} g^{-1}(M) \left(\frac{M}{10^{15}\,\mathrm{g}}\right)^3. \tag{2.29}$$

Constraints on evaporating PBHs

We review some of constraints on evaporating PBHs (Fig. 2.10). For the constraints on evaporating PBHs, one usually used $\beta(M)$ which is constraints on the fraction of the Universe collapsing into PBHs at their formation epoch. In the mass range $10^9\,\mathrm{g} \lesssim M \lesssim 10^{17}\,\mathrm{g}$, BBN, CMB and extragalactic gamma-ray background (EGB) gave the most stringent limits. Other constraints are discussed in [168].

The first example is BBN. Evaporating PBHs emit high-energy particles such as photons, mesons, hadrons, antinucleons and so on. This can modify the standard BBN scenario. For example, ^{4}He are dissociated by the high-energy photons produced in cascade, increasing the abundance of lighter elements. The high-energy hadrons also dissociate light elements nucleated in BBN, which reduces ^{4}He and increases D, T, ^{3}He, ^{6}Li and ^{7}Li. Extra interconversion between protons and neutrons can be induced by emitted mesons

and antinucleons, increasing the n/p freeze-out ratio and the final ^{4}He abundance. BBN constraints are shown as the pink line in Fig. 2.10.

Observations of extragalactic gamma-ray backgrounds have also given constraints on evaporating PBHs. After primary particles are emitted with the Hawking evaporation, secondary particles are produced from the primary particles. The photon spectrum is expressed by the sum of the primary and secondary ones

$$\frac{\mathrm{d}\dot{N}_\gamma}{\mathrm{d}E_\gamma}(E_\gamma, M) = \frac{\mathrm{d}\dot{N}_\gamma^{\mathrm{pri}}}{\mathrm{d}E_\gamma}(E_\gamma, M) + \frac{\mathrm{d}\dot{N}_\gamma^{\mathrm{sec}}}{\mathrm{d}E_\gamma}(E_\gamma, M) \tag{2.30}$$

where dots denote a time derivative. These can contribute to extragalactic gamma-ray backgrounds. Considering redshift effects in energy of particles produced at earlier cosmological epochs, the current background spectrum of gamma rays can be calculated. The result is shown in Fig. 2.9 taken from [168]. The calculated fluxes for different PBH masses should not exceed existing X-ray and gamma-ray observations such as HEAO 1, balloon observations, COMPTEL, EGRET and Fermi-LAT. This has given the upper bound as denoted by the red line in Fig. 2.10.

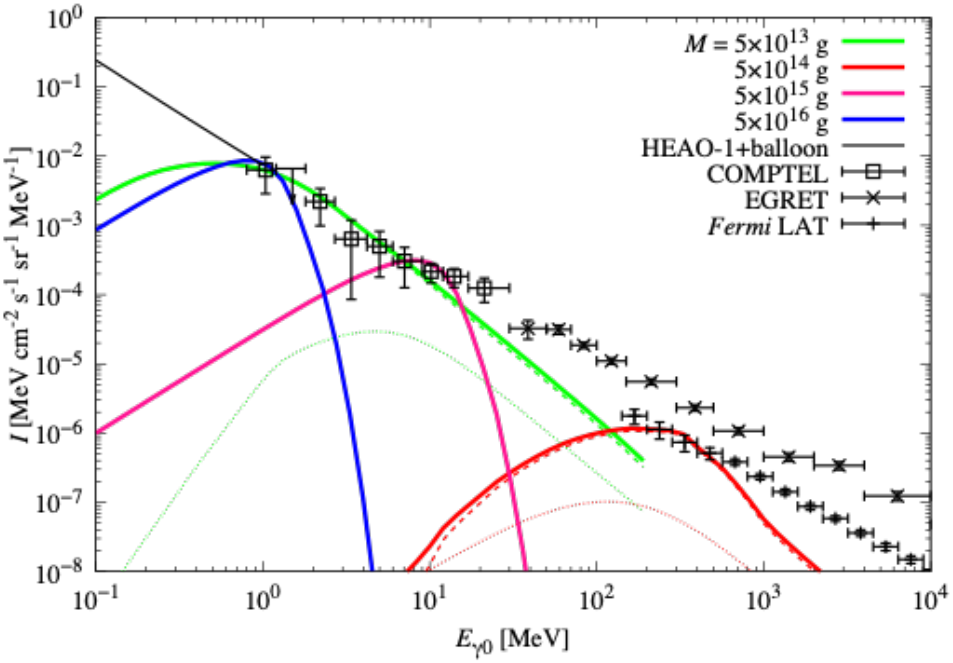

Figure 2.9: Fluxes corresponding to the upper limit on the PBH abundance for various values of M, coming from the observations from HEAO 1 and balloon observations, COMPTEL, EGRET and Fermi-LAT. The dotted lines denote fluxes of secondary photons. Figure taken from [168].

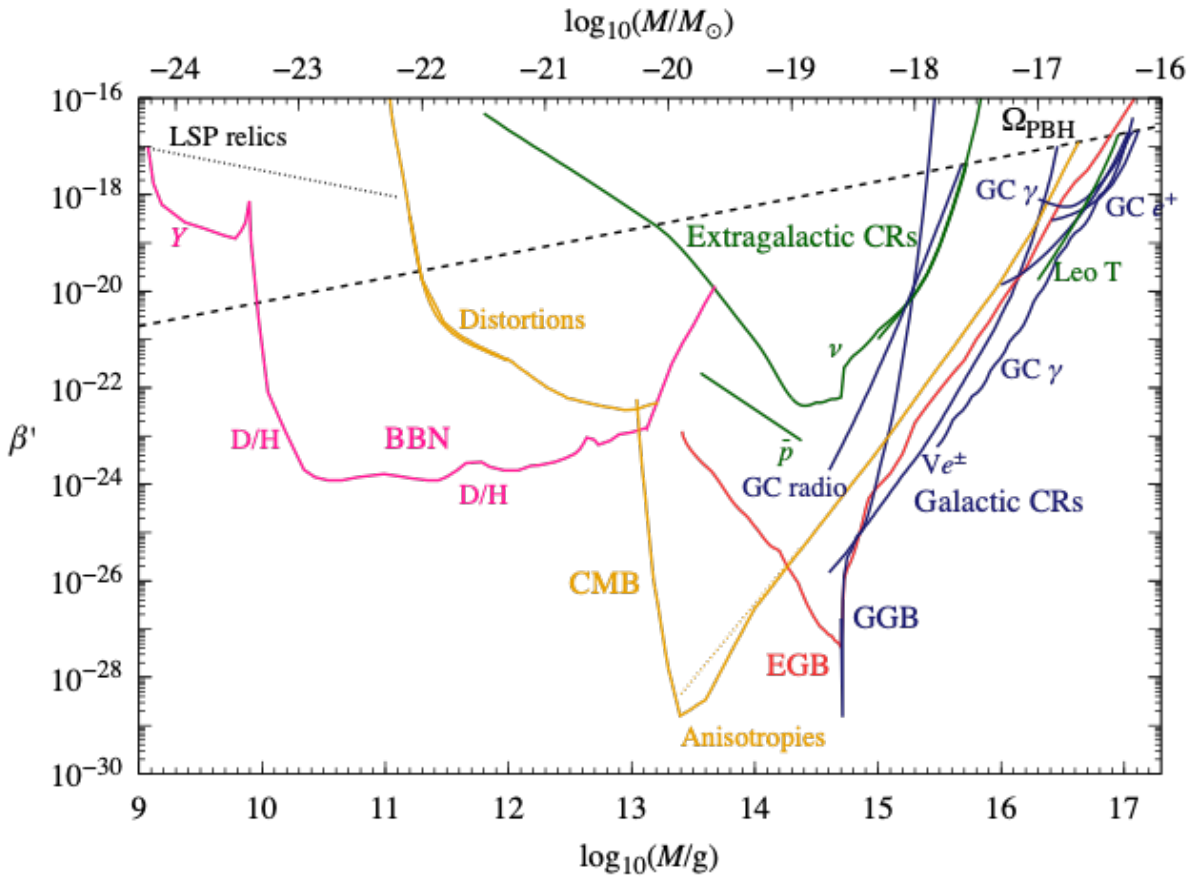

Figure 2.10: Constraints on evaporating PBHs (taken from Fig. 4 of [168]). Combined BBN (pink) and EGB (red) limits, compared to other constraints on evaporating PBHs from LSP relics (dotted grey since dependent on LSP mass), the CMB spectral distortions and anisotropies (yellow), extragalactic antiprotons and neutrinos (green), the GGB and the electrons and positrons observed by Voyager 1 (blue). Less secure limits come from observations of primary photons, electron-positron annihilation and radio emission from the GC (blue since Galactic) and Leo T (green since extragalactic). The dashed line is the only constraint for no Hawking radiation.

Constraints on non-evaporated PBHs

Constraints on non-evaporating PBHs are coming from lensing, accretion effects, gravitational wave observations and so on. For these constraints, fraction of the DM in PBHs $f(M)$ is used unlike the evaporating ones [168]. Fig. 2.11 shows such constraints on $f(M)$. The mass window $10^{17}\,\mathrm{g} \lesssim M \lesssim 10^{23}\,\mathrm{g}$ is open under an assumption that PBH mass spectrum is quasi-monochromatic. Its extension still remains a possibility.

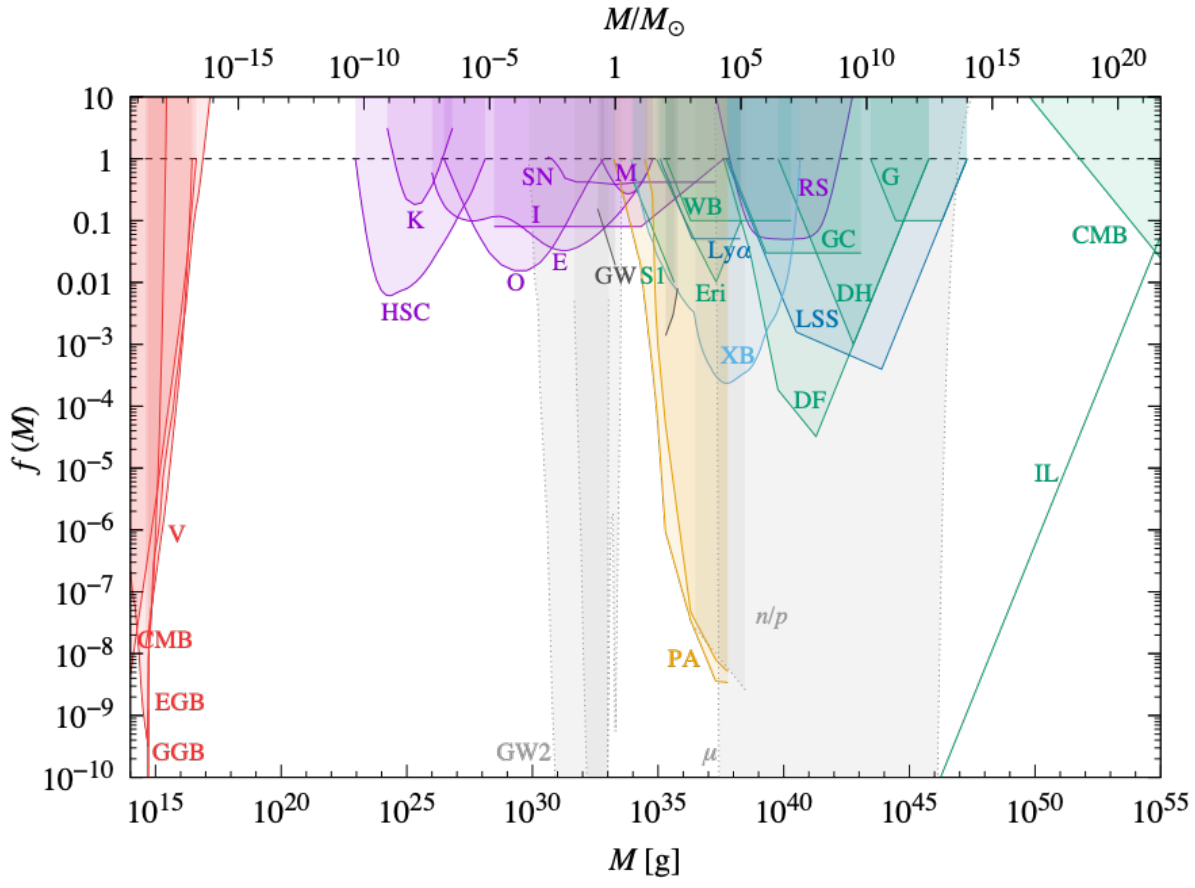

Figure 2.11: Constraints on $f(M)$ for non-evaporating PBHs (taken from Fig. 10 of [168]) given by evaporation (red), lensing (magenta), dynamical effects (green), gravitational waves (black), accretion (light blue), CMB distortions (orange) and so on. Other constraints are explained in [168].

2.3 Axions

In addition to the WIMPs and PBHs, axions are also a dark matter candidate also motivated as a solution to so-called strong CP problem. In Section 2.3 we first review the strong CP problem in the SM and Peccei-Quinn (PQ) mechanism as its solution. After an overview of axion models such as KSVZ and DFSZ models [7–10], we show axion interactions with SM particles and then axion-like particles (ALPs). Several axion searches are discussed in Section 2.4.

2.3.1 Strong CP problem

Quantum Chromodynamics (QCD) allows the following theta term to appear

$$\mathcal{L}_\theta = \theta \frac{g^2}{32\pi^2} G^a_{\mu\nu} \tilde{G}^{a,\mu\nu} \tag{2.31}$$

which violates CP symmetry. Here, g is the gauge coupling, $G^a_{\mu\nu}(a = 1, \ldots, 8)$ is the SU(3) gauge field strength, and $\tilde{G}^{a,\mu\nu}$ is its dual. Let us consider the following Lagrangian

$$\mathcal{L} = -\frac{1}{4} G^a_{\mu\nu} G^{a,\mu\nu} + \mathcal{L}_\theta + \bar{\Psi}_i (i\gamma^\mu D_\mu) \Psi_i - \bar{\Psi}_i M_{ij} \Psi_j + \text{h.c.} \tag{2.32}$$

where $\Psi_i (i = 1, \ldots, N)$ are the N-flavor fermions, $\bar{\Psi}_i$ is their Dirac conjugate, and h.c. denotes the Hermitian conjugate. $M_{ij}(i, j = 1, \ldots, N)$ is the mass matrix and generally complex. We can diagonalize this mass matrix with unitary matrices. After diagonalizing the mass matrix, its diagonal components have complex phases and they can be removed with $U(1)$ axial transformation for the fermions

$$\Psi_i = \exp\left(-i \frac{\arg(M_{ii})\gamma_5}{2}\right) \Psi_i \tag{2.33}$$

$$\bar{\Psi}_i = \bar{\Psi}_i \exp\left(-i \frac{\arg(M_{ii})\gamma_5}{2}\right) \tag{2.34}$$

where $\gamma^5 \equiv i\gamma^0\gamma^1\gamma^2\gamma^3$ can be expressed as

$$\gamma^5 = \begin{pmatrix} -1 & 0 \\ 0 & 1 \end{pmatrix}$$

under the following representation for γ^μ

$$\gamma^0 = \begin{pmatrix} 0 & 1 \\ 1 & 0 \end{pmatrix} \qquad \gamma^i = \begin{pmatrix} 0 & \sigma^i \\ -\sigma^i & 0 \end{pmatrix}.$$

Under $U(1)$ axial transformations, a measure of a path integral transform

$$\mathcal{D}\Psi_i \mathcal{D}\bar{\Psi}_i \to \mathcal{D}\Psi_i \mathcal{D}\bar{\Psi}_i \exp\left[-i \int d^4x \, \arg(M_{ii}) \frac{g^2}{32\pi^2} G^a_{\mu\nu} \tilde{G}^{a,\mu\nu}\right] \tag{2.35}$$

and the Lagrangian becomes

$$\mathcal{L} = -\frac{1}{4} G^a_{\mu\nu} G^{a,\mu\nu} + \left(\theta + \sum_i \arg(M_{ii})\right) \frac{g^2}{32\pi^2} G^a_{\mu\nu} \tilde{G}^{a,\mu\nu} + \sum_i \bar{\Psi}_i (i\gamma^\mu D_\mu - \tilde{M}_{ii}) \Psi_i \tag{2.36}$$

where $\tilde{M}_{ii}$ is the real diagonal matrix. We now find that not θ but $\bar{\theta}$

$$\bar{\theta} = \theta + \sum_i \arg(M_{ii}) = \theta + \arg(\det M) \tag{2.37}$$

is a physical parameter. The discussion implies that the theta term violating CP symmetry appears in the Lagrangian and the physical parameter $\bar{\theta}$ is responsible for how much the theta term is violating CP symmetry. The CP violation can induce a neutron electronic dipole moment (EDM) d_n which is calculated as

$$d_n = 4.5 \times 10^{-15} \bar{\theta} \, \mathrm{e\,cm}, \tag{2.38}$$

and experiments have given an upper bound

$$|d_n| < 1.8 \times 10^{-26} \, \mathrm{e\,cm}. \tag{2.39}$$

This bound can be translated into

$$|\bar{\theta}| < 0.4 \times 10^{-11} \tag{2.40}$$

although its value can be $\mathcal{O}(1)$ without a specific reason. QCD allows the CP violating term to appear in its Lagrangian but its effects are tiny in fact. This is so-called strong CP problem.

2.3.2 Peccei-Quinn mechanism

Peccei and Quinn proposed a dynamical solution to the strong CP problem [3, 4] where the CP violating $\bar{\theta}$ is regarded as a dynamical field and $\bar{\theta} = 0$ is realized in the minimum of its potential $V(\bar{\theta})$ as follows. Let us consider 1-flavor case

$$\mathcal{L} = -\frac{1}{4} G^a_{\mu\nu} G^{a,\mu\nu} + \bar{\theta} \frac{g^2}{32\pi^2} G^a_{\mu\nu} \tilde{G}^{a,\mu\nu} + \bar{\Psi}(i\gamma^\mu D_\mu - m)\Psi. \tag{2.41}$$

Euclidean action is

$$S_E = \int d^4x_E \left[\frac{1}{4} G^{Ea}_{\mu\nu} G^{Ea}_{\mu\nu} + i\bar{\theta} \frac{g^2}{32\pi^2} G^{Ea}_{\mu\nu} \tilde{G}^{Ea}_{\mu\nu} + \bar{\Psi}_E(\gamma^E_\mu D^E_\mu + m)\Psi_E \right] \tag{2.42}$$

where $D^E_\mu = \partial_\mu - igA^E_\mu$. Euclidean gamma matrices are given by $\gamma^4_E = \gamma^0$, $\gamma^i_E = -i\gamma^i$ which satisfies $\gamma^\mu_E, \gamma^\nu_E = 2\delta^{\mu\nu}$, $(\gamma^\mu_E)^\dagger = \gamma^\mu_E$. The effective potential $V(\bar{\theta})$ is given by

$$\begin{aligned} \exp\left[-\int d^4x_E V(\bar{\theta}) \right] &= \int \mathcal{D}A^{Ea}_\mu \mathcal{D}\Psi_E \mathcal{D}\bar{\Psi}_E \exp[-S_E] \\ &= \int \mathcal{D}A^{Ea}_\mu \det\left(\gamma^E_\mu D^E_\mu + m\right) \\ &\quad \times \exp\left[-\int d^4x_E \left(\frac{1}{4} G^{Ea}_{\mu\nu} G^{Ea}_{\mu\nu} + i\bar{\theta} \frac{g^2}{32\pi^2} G^{Ea}_{\mu\nu} \tilde{G}^{Ea}_{\mu\nu} \right) \right]. \end{aligned} \tag{2.43}$$

Using the fact that $\det\left(\gamma^E_\mu D^E_\mu + m\right) = \prod_n (\lambda_n^2 + m^2) > 0$ with the eigen values λ_n for $\gamma^E_\mu D^E_\mu$, it is shown that

$$\begin{aligned} \exp\left[-\int d^4x_E V(\bar{\theta}) \right] &\leqq \int \mathcal{D}A^{Ea}_\mu \det\left(\gamma^E_\mu D^E_\mu + m\right) \exp\left[\int d^4x_E \left(-\frac{1}{4} G^{Ea}_{\mu\nu} G^{Ea}_{\mu\nu} \right) \right] \\ &= \exp\left[-\int d^4x_E V(0) \right] \end{aligned} \tag{2.44}$$

and that the potential takes its minimum at $\bar{\theta} = 0$.

In order to make $\bar{\theta}$ a dynamical variable and solve the strong CP problem, $U(1)_{\rm PQ}$ symmetry and a PQ scalar ϕ with $U(1)_{\rm PQ}$ charge are introduced. Lagrangian additionally with the PQ scalar is given by

$$\mathcal{L} = -\frac{1}{4} G^a_{\mu\nu} G^{a,\mu\nu} + \bar{\theta} \frac{g^2}{32\pi^2} G^a_{\mu\nu} \tilde{G}^{a,\mu\nu} + \bar{\Psi} i\gamma^\mu D_\mu \Psi + \mathcal{L}_{\rm Yukawa} + \mathcal{L}_{\rm PQ} \tag{2.45}$$

where the kinetic and potential terms for the PQ scalar $\mathcal{L}_{\rm PQ}$ is given by

$$\mathcal{L}_{\rm PQ} = |\,\partial_\mu\phi|^2 - \frac{1}{4}\left(|\phi|^2 - \frac{v^2}{2}\right)^2, \tag{2.46}$$

and $\mathcal{L}_{\rm Yukawa}$ represents the Yukawa terms

$$\mathcal{L}_{\rm Yukawa} = y\bar{\Psi}(\phi P_R + \phi^* P_L)\Psi = y(\phi^*\chi\xi + \phi\xi^\dagger\chi^\dagger) \tag{2.47}$$

Here, $P_L = (1-\gamma^5)/2$ and $P_R = (1+\gamma^5)/2$ are the chiral projection operators, and $\Psi = (\chi, \xi^\dagger)^T$. The potential term for ϕ and $\mathcal{L}_{\rm Yukawa}$ are invariant under the following $U(1)_{\rm PQ}$ transformations

$$\chi \to e^{i\alpha}\chi, \xi \qquad\qquad \to e^{i\alpha}\xi, \phi \to e^{2i\alpha}\phi. \tag{2.48}$$

The PQ scalar potential takes minimum at $|\phi| = v/\sqrt{2}$ and $U(1)_{\rm PQ}$ is spontaneously broken. The PQ scalar is written as $\phi = ve^{i\frac{a}{v}}/\sqrt{2}$ where a is the dynamical variable corresponding to phase direction of ϕ. It is the Nambu-Goldstone boson associated with $U(1)_{\rm PQ}$ breaking and called QCD axion. Now the Yukawa term becomes

$$\mathcal{L}_{\rm Yukawa} = y\frac{v}{\sqrt{2}}(e^{-i\frac{a}{v}}\chi\xi + e^{i\frac{a}{v}}\xi^\dagger\chi^\dagger). \tag{2.49}$$

The phase factors can be removed by transformations of fermions

$$\chi \to e^{i\frac{a}{2v}}\chi, \tag{2.50}$$

$$\xi \to e^{i\frac{a}{2v}}\xi, \tag{2.51}$$

and then $\bar{\theta}$ becomes

$$\bar{\theta} \to \bar{\theta} - \frac{a}{v}. \tag{2.52}$$

When the QCD axion takes vacuum expectation value $\langle a\rangle = \bar{\theta}v$, the QCD axion settles at CP invariant vacuum .

2.3.3 Axion models

We have seen that the strong CP problem was solved by the PQ mechanism where QCD axion appeared after spontaneous symmetry breaking of the $U(1)_{\rm PQ}$. This subsection introduces examples to realize the PQ mechanism, such as KSVZ model [7, 8] and DFSZ

model [9, 10].

KSVZ axion

In the KSVZ model, a PQ scalar Φ and heavy quarks $Q_i\,(i = 1, \ldots, N_Q)$ are additionally introduced in addition to the particles in the SM. The PQ scalar is a singlet under $SU(3)_C \times SU(2)_L \times U(1)_Y$. Its potential $V(\Phi)$ is given by

$$V(\Phi) = -\mu_\Phi^2 |\Phi|^2 + \frac{1}{4}\lambda_\Phi |\Phi|^4. \tag{2.53}$$

The heavy quarks have Yukawa interaction with the PQ scalar as

$$\mathcal{L}_{\text{Yukawa}} = -y_{ij}\bar{Q}_{Li}\Phi Q_{Ri} - y_{ij}^*\bar{Q}_{Rj}\Phi^* Q_{Lj} \tag{2.54}$$

where $Q_L = P_L Q$ and $Q_R = P_R Q$ are defined with projection operators P_L and P_R, respectively. These interactions are invariant the following transformations under $U(1)_{\text{PQ}}$

$$\Phi \to e^{2iq\alpha}\Phi \tag{2.55}$$

$$Q_{Li} \to e^{iq\alpha}Q_{Li} \tag{2.56}$$

$$Q_{Ri} \to e^{-iq\alpha}Q_{Ri}. \tag{2.57}$$

$V(\Phi)$ has its minimum at $|\Phi| = \sqrt{2}\mu_\Phi/\sqrt{\lambda_\Phi}$. Φ can be written as

$$\Phi = \frac{\eta}{\sqrt{2}} \exp\left(i\frac{a}{\eta}\right) \tag{2.58}$$

The QCD axion a interact with $SU(3)_C$ gauge fields

$$\mathcal{L}_{agg} = -\frac{g^2}{32\pi^2}\frac{a}{f_a}G_{\mu\nu}^a \tilde{G}^{a\,\mu\nu} \tag{2.59}$$

where $f_a = \eta/N_Q$ is the decay constant of the QCD axion.

DFSZ axion

The DFSZ model does not include the heavy quarks as opposed to the KSVZ model. Instead, two Higgs fields $H_u = (H_u^0, H_u^-)$, $H_d = (H_d^+, H_d^0)$ are introduced in addition to a PQ scalar Φ. They are $SU(2)_L$ doublets. Their Yukawa interactions are given by

$$\mathcal{L}_{\text{Yukawa}} = -y_{ij}^u \bar{q}_{Li} H_u u_{Rj} - y_{ij}^d \bar{q}_{Li} H_d d_{Rj} + \text{h.c.} \tag{2.60}$$

where $q_L = (u_L, d_L)$ is the left-handed quark, and u_R, d_R are the right-handed up-type and down-type quarks, respectively. y_{ij} is the Yukawa coupling and i, j denotes the indices describing generations. Potential terms for scalar fields are

$$\begin{aligned} V(H_u, H_d, \Phi) =& \lambda_u \left(H_u^\dagger H_u - \frac{v_u^2}{2} \right)^2 + \lambda_d \left(H_d^\dagger H_d - \frac{v_d^2}{2} \right)^2 + \lambda_\Phi \left(|\Phi|^2 - \frac{v_\Phi^2}{2} \right)^2 \\ &+ (a H_u^\dagger H_u + b H_d^\dagger H_d)|\Phi|^2 - c(H_u \cdot H_d |\Phi|^2 + \text{h.c.}) + d|H_u \cdot H_d|^2 + e|H_u^* \cdot H_d|^2 \end{aligned} \tag{2.61}$$

where the couplings are denoted by $\lambda_u, \lambda_d, \lambda_\Phi, a, b, c, d, e$. The Yukawa interaction is invariant under the following $U(1)_{\text{PQ}}$ transformations

$$H_u \to \exp(iX_u\alpha) H_u \tag{2.62}$$

$$H_d \to \exp(iX_d\alpha) H_d \tag{2.63}$$

$$\Phi \to \exp(iX_\Phi\alpha)\Phi \tag{2.64}$$

$$q_L \to q_L \tag{2.65}$$

$$u_R \to \exp(-iX_u\alpha) u_R \tag{2.66}$$

$$d_R \to \exp(-X_d\alpha) d_R \tag{2.67}$$

with $U(1)_{\text{PQ}}$ charges X_u, X_d, X_Φ. The scalar potential terms are also $U(1)_{\text{PQ}}$ if $X_u + X_d = -2X_\Phi$.

Scalar fields take their vacuum expectation values

$$\langle H_u \rangle = \frac{v_u}{\sqrt{2}} \exp\left(i\frac{\phi_u}{v_u} \right) \begin{pmatrix} 1 \\ 0 \end{pmatrix} \tag{2.68}$$

$$\langle H_d \rangle = \frac{v_d}{\sqrt{2}} \exp\left(i\frac{\phi_d}{v_d} \right) \begin{pmatrix} 0 \\ 1 \end{pmatrix} \tag{2.69}$$

$$\langle \Phi \rangle = \frac{v_\Phi}{\sqrt{2}} \exp\left(i\frac{\phi_\Phi}{v_\Phi} \right) \tag{2.70}$$

with the three phases

$$\phi_u = -\frac{v_u}{v} h + \frac{v_d v_\Phi}{v\eta} H - \frac{v_d}{\eta} \frac{2x}{1+x^2} a \tag{2.71}$$

$$\phi_d = \frac{v_d}{v} h + \frac{v_u v_\Phi}{v\eta} H - \frac{v_u}{\eta} \frac{2x}{1+x^2} a \tag{2.72}$$

$$\phi_\Phi = \frac{v}{\eta} \frac{2x}{1+x^2} H + \frac{v_\Phi}{\eta} a \tag{2.73}$$

where $v = \sqrt{v_u^2 + v_d^2}$, $x = v_d/v_u$, and η is given by

$$\eta^2 = v_\Phi^2 + \frac{4v_u^2 v_d^2}{v^2} = v_\Phi^2 + 4\left(x + \frac{1}{x}\right)^{-2} v^2. \tag{2.74}$$

When $\eta \gg v \sim v_d \sim v_u$, we get $\phi_\Phi \simeq a$. Considering the QCD axion a, the Yukawa interaction is

$$\begin{aligned}\mathcal{L}_{\text{Yukawa}} =& \frac{y_{ij}^u}{\sqrt{2}} v_u \bar{u}_{Li} \exp\left(-i\frac{2x^2}{1+x^2}\frac{a}{\eta}\right) u_{Rj} \\ &- \frac{y_{ij}^d}{\sqrt{2}} v_d \bar{d}_{Li} \exp\left(-i\frac{2}{1+x^2}\frac{a}{\eta}\right) d_{Rj}.\end{aligned} \tag{2.75}$$

With transformation of quarks, axion-gluon coupling becomes

$$\mathcal{L}_{agg} = \frac{g^2}{32\pi^2}\frac{a}{f_a} G_{\mu\nu}^a \tilde{G}^{a\,\mu\nu} \tag{2.76}$$

where $f_a = \eta/(2N_g)$ is the axion decay constant, and N_g is the number of generations.

Axion interaction with SM particles

We expect interaction between the QCD axions and the SM particles. For example, the SM quarks and charged leptons have PQ charges and interact with the QCD axions since they have PQ charges in the DFSZ model. In KSVZ model, the QCD axion has the interaction with the SM quarks through loop effects of heavy quarks with their PQ charges. Thus, interactions between the QCD axion, nuclei N with its mass m_N and electrons e with its mass m_e are given by

$$\mathcal{L}_{aNN} = \frac{g_{aNN}}{2m_N}\,\partial_\mu a(\bar{N}\gamma^\mu\gamma_5 N) \tag{2.77}$$

$$\mathcal{L}_{aee} = \frac{g_{aee}}{2m_e}\,\partial_\mu a(\bar{e}\gamma^\mu\gamma_5 e) \tag{2.78}$$

where g_{aNN} is the axion-nucleon coupling, g_{aee} is the axion-electron coupling, and they are proportional to $1/f_a$. Their numerical factors depend on models. Especially, g_{aee} is small in the KSVZ model where the QCD axion does not directly interact with the electron.

In general, the QCD axion also couple to photon through

$$\mathcal{L}_{a\gamma\gamma} = -\frac{1}{4} g_{a\gamma\gamma} a F_{\mu\nu}\tilde{F}^{\mu\nu} \tag{2.79}$$

where $g_{a\gamma\gamma} = \alpha C/(2\pi f_a)$ is the axion-photon coupling, α is the fine structure constant,

and C is given by

$$C = \frac{\mathcal{E}}{\mathcal{N}} - \frac{2(4 + m_u/m_d)}{3(1 + m_u/m_d)} \tag{2.80}$$

with anomaly coefficients $\mathcal{E}$ and $\mathcal{N}$. With $m_u/m_d = 0.46$, C becomes -2.04 in the KSVZ model while 0.63 in the DFSZ model.

Axion-like particles

The QCD axion appear as a solution to the strong CP problem in the PQ mechanism. Theories beyond the SM often predict axion-like particles (ALPs) which are a kind of the generalization of the QCD axion. For instance, superstring theory may include the ALPs associated with compactification of extra spaces. Although the ALPs do not solve the strong CP problem, they can be a dark matter candidate. The axion parameter space is very broad including ALPs (Fig. 2.12). Both the QCD axion and ALPs have been explored. In the next section, specific examples of axion searches are introduced.

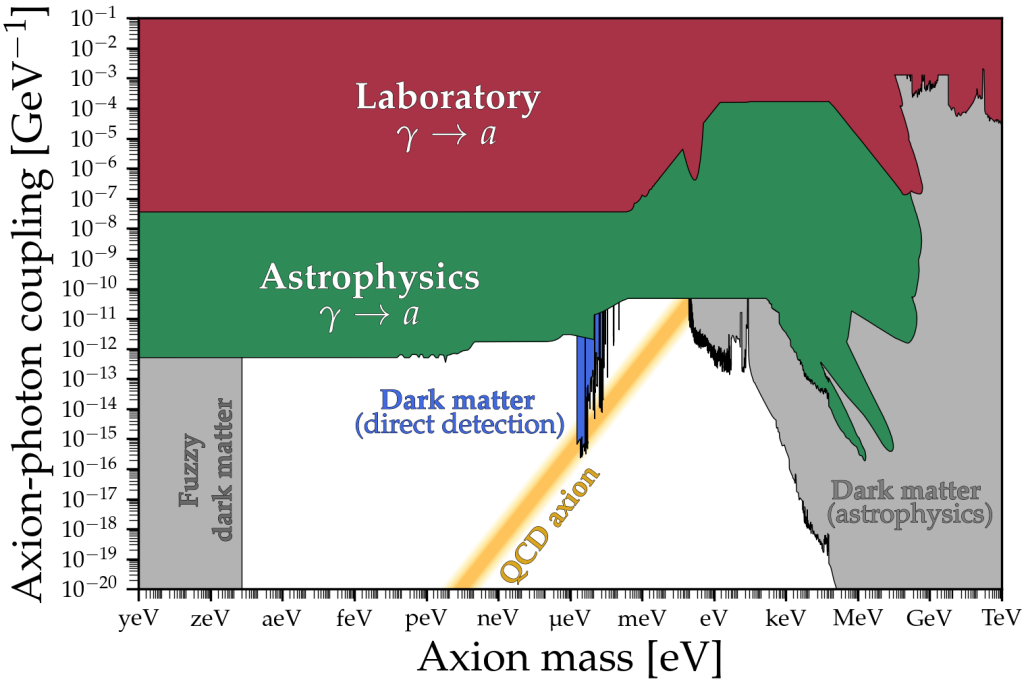

Figure 2.12: Simplified summary of existing constraints with the haloscopes corresponding to the blue region, the helioscopes included in the green space, and the laboratory experiments such as LSW within the red region. QCD axion models are expressed by the yellow band. Gray region shows parameter space where ultra-light axions work as so-called fuzzy dark matter and heavier axion decay are constrained with observations of produced photons although we do not discuss them in this thesis. Figure taken from [169].

2.4 Axion searches

We have seen that axions are motivated as a solution to the strong CP problem and/or a dark matter candidate in Section 2.3. Next question is how we can look for them. Axion searches are on-going. For example, axion haloscopes, axion helioscopes and LSW experiments are exploring axions and have constrained them as we will see below.

2.4.1 Axion haloscopes

Axion haloscopes try to detect axion dark matter in the galactic halo [43–50]. They have strong magnetic fields imposed in their cavity which allows for axions in the galactic halo to convert into photons as a signal. When the axion mass m_a matches the frequency corresponding to the system, resonance effects enhance the sensitivity to axion parameters. The efficiency is characterized by a cavity quality factor Q. In a set of typical parameter values for an axion haloscope, the signal power deposited to the cavity is given by

$$P = 5.0 \times 10^{-23}\,\mathrm{W} \left(\frac{V}{30\,\mathrm{L}}\right) \left(\frac{B}{10\,\mathrm{T}}\right)^2 \left(\frac{C}{0.5}\right) \times \left(\frac{c_\gamma}{0.97}\right)^2 \left(\frac{\rho_a}{0.45\,\mathrm{GeV/cm^3}}\right) \left(\frac{\nu}{1\,\mathrm{GHz}}\right) \left(\frac{Q}{10000}\right) \tag{2.81}$$

where V is the volume of the cavity, B is the magnitude of the external magnetic field, c_γ is the model dependent coefficient of the axion-photon coupling, whose value is -1.92 (0.75) for the KSVZ (DFSZ) model, ρ_a is the local dark matter density, ν is the frequency of the photon, Q is the loaded quality factor of the cavity, and C is the form factor of the cavity.

Improving the signal-to-noise ratio (SNR) SNR $= P/\delta P_s$ is important to get better sensitivity by experiments. Here, δP_s is fluctuations in the system noise power $P_s = k_B T_s \delta\nu$ (the Johnson-Nyquist formula) with the Boltzmann constant k_B and the system noise temperature. When we survey axion parameter space in a mass range, its scan rate is important and given by

$$\frac{\mathrm{d}\nu}{\mathrm{d}t} = 1.2\,\mathrm{GHz/year} \left(\frac{5}{\mathrm{SNR}}\right)^2 \left(\frac{0.15\,\mathrm{K}}{T_S}\right)^2 \left(\frac{P}{5.0 \times 10^{-23}\,\mathrm{W}}\right)^2 \left(\frac{10000}{Q}\right) \tag{2.82}$$

This determines how we can scan a mass region with a sensitivity. Given a logarithmic

scan rate, we could explore the smallest coupling

$$g_{a\gamma\gamma}^2 \propto \frac{T_S}{B^2 V} \tag{2.83}$$

This motivates us to reduce T_S for scanning lower axion-photon coupling $g_{a\gamma\gamma}$ with a faster scan rate.

Axion Dark Matter eXperiment (ADMX) is a haloscope with a large ($V = 136\,\mathrm{L}$) and cylindrical cavity equipped with a superconducting magnet ($B \simeq 7.0\,\mathrm{T}$). The ADMX and other haloscopes are trying to touch axion models denoted by the yellow band in Fig. 2.13. Their constraints are shown by red vertical bands. The ADMX has already started to explore the KSVZ and DFSZ models introduced in Section 2.3.

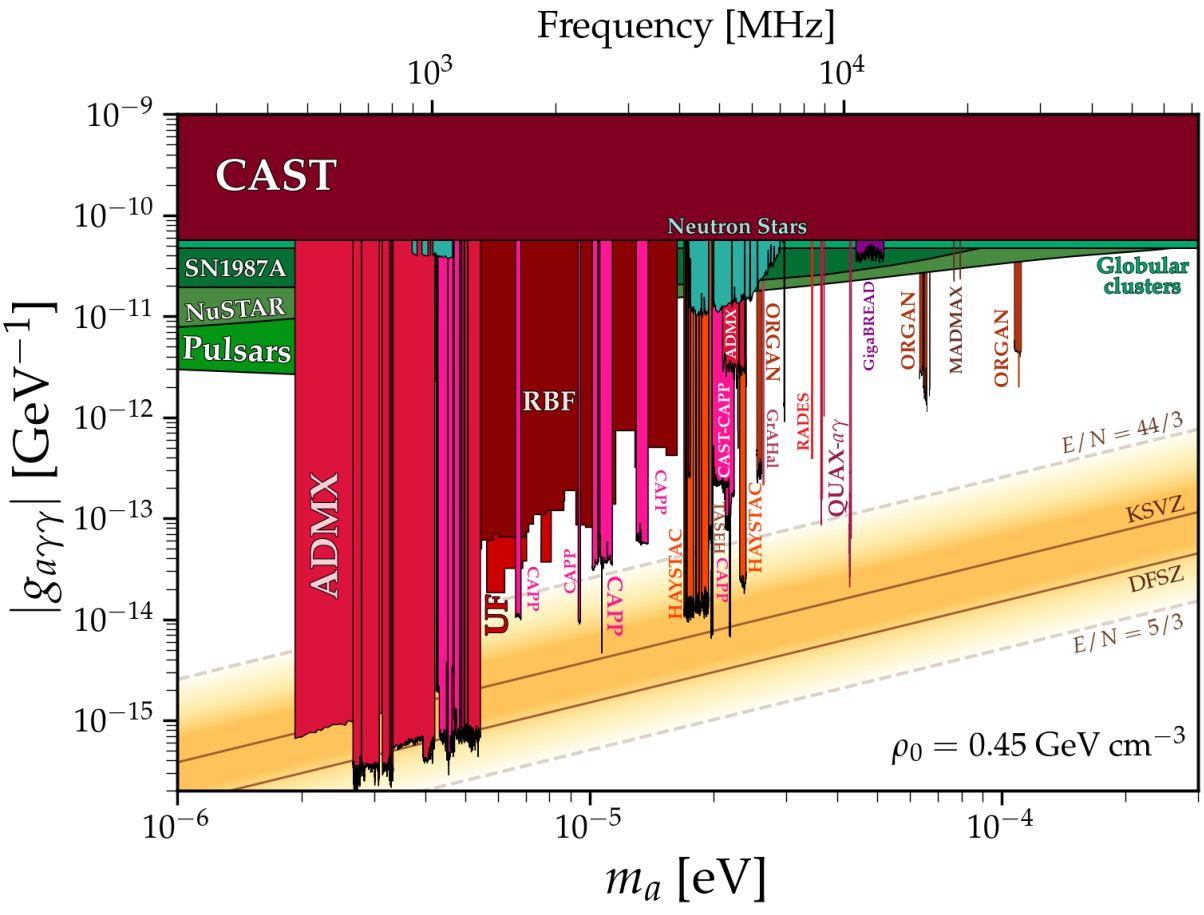

Figure 2.13: Summary of constraints with haloscopes. Figure taken from [169].

2.4.2 Axion helioscopes

Axion helioscopes are looking for axions produced within the Sun [32–42]. Axions a can be produced in the Sun through several processes such as Primakoff process $\gamma + Q \to a + Q$ where thermal photons γ inside the core of the Sun can be converted into axions a by electric fields induced by charged particles Q. Primakoff process is characterized by the axion-photon coupling $g_{a\gamma\gamma}$. The transition rate for a photon to an axion in a stellar plasma with temperature T is given by [33]

$$\Gamma_{\gamma\to a} = \frac{g_{a\gamma\gamma}^2 T \kappa_s^2}{32\pi}\left[\left(1+\frac{\kappa_s^2}{4E^2}\right)\ln\left(1+\frac{4E^2}{\kappa_s^2}\right)-1\right] \tag{2.84}$$

where E is the photon energy and κ_s represents the screening scale

$$\kappa_s^2 = \frac{4\pi\alpha}{T}\left(n_e + \sum_j Z_j^2 n_j\right) \tag{2.85}$$

with the electron number density n_e, the number density of the j-th ion n_j with charge Z_j, and the fine structure constant α. One can get total axion number flux at the Earth

$$\Phi_a = \frac{R_\odot^3}{4\pi D_\odot^2}\int_0^1 dr 4\pi r^2 \int_{\omega_{\rm pl}}^\infty dE \frac{4\pi k^2}{(2\pi)^3}\frac{\mathrm{d}k}{\mathrm{d}E} 2 f_b \Gamma_{\gamma\to a} \tag{2.86}$$

where $D_\odot$ is the average solar distance, $R_\odot$ is the solar radius, r is a solar radial variable normalized by $R_\odot$, $f_b = (e^{E/T}-1)^{-1}$ is the Bose-Einstein distribution of the thermal photon bath in the Sun, and $\omega_{\rm pl}^2 = 4\pi\alpha n_e/m_e$ is the plasma frequency of photons in the Sun. After integration over a solar model, we can get solar axion flux. It is characterized as

$$\frac{\mathrm{d}\Phi_a}{\mathrm{d}E} = 6.02\times10^{10}\,\mathrm{cm^{-2}s^{-1}keV^{-1}}\left(\frac{g_{a\gamma\gamma}}{10^{-10}\,\mathrm{GeV^{-1}}}\right)^2 E^{2.481} e^{-E/1.205} \tag{2.87}$$

where the energy E in keV. Fig. 2.14 shows the expected solar axion flux with respect to the energy in keV.

The solar axions produced through the Primakoff process can escape from the solar interior and arrive at Earth. Helioscopes convert the solar axions to photons by imposing a strong magnetic field with a dipole magnet towards the Sun. Fig. 2.15 represents a typical experimental setup of helioscopes. The energy of solar axions is typically $\mathcal{O}$(keV) Fig. 2.14 meaning that expected photon signals would be observed as X-rays by the detector in a

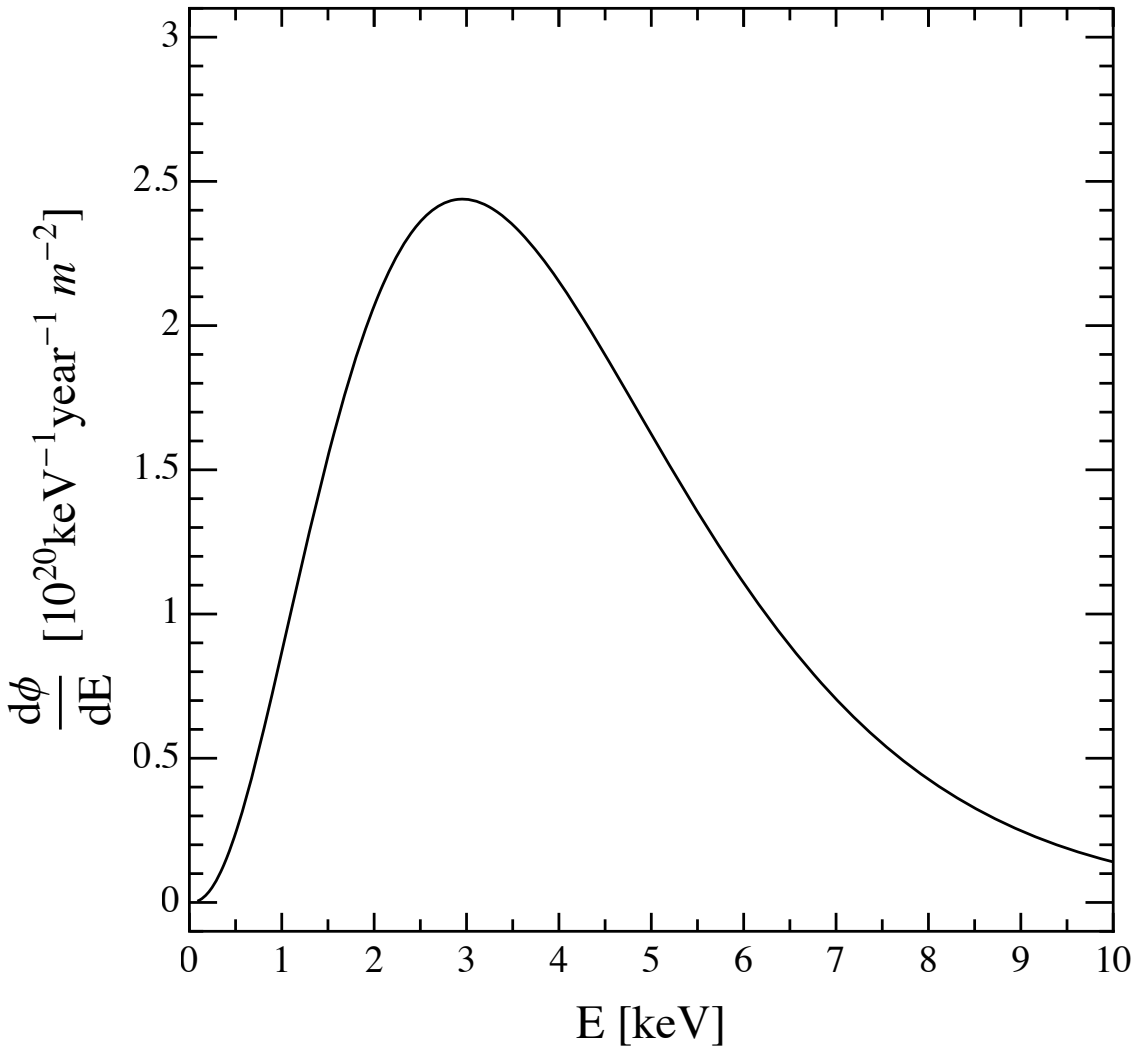

Figure 2.14: Solar axion flux spectra at the Earth. The axion-photon coupling $g_{a\gamma\gamma} = 10^{-12}\,\mathrm{GeV}^{-1}$ for illustration. Figure taken from [30].

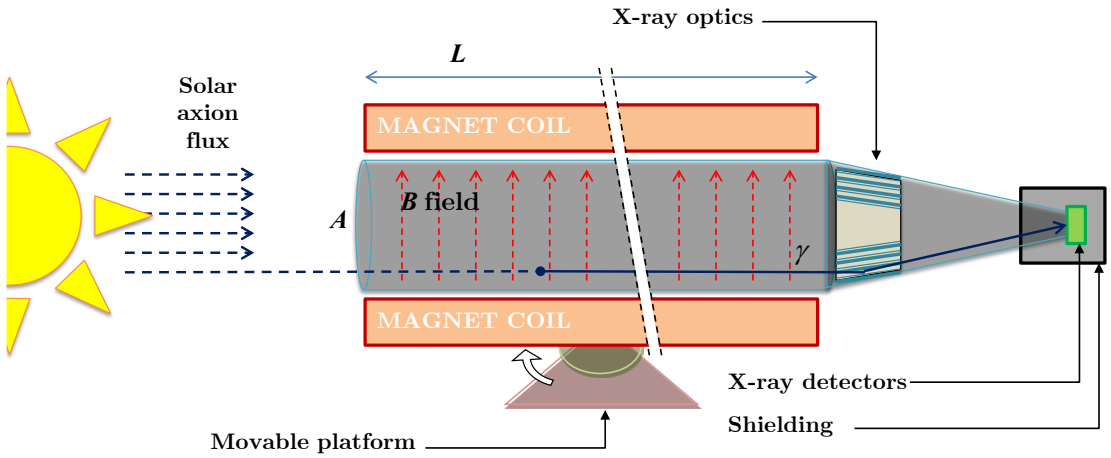

Figure 2.15: A typical helioscope design. Solar axions can be converted into X-rays by magnetic fields imposed with powerful magnets. The X-rays are concentrated onto detectors with X-ray optics. Figure taken from [30].

helioscope. The axion-photon conversion probability is given by

$$P_{a\to\gamma} = \left(\frac{g_{a\gamma\gamma}B}{q}\right)^2 \sin^2\left(\frac{qL}{2}\right) \tag{2.88}$$

with $q = m_a^2/(2E_a)$, magnetic field B, and the size of the system L (see appendix for its derivation). By multiplying the conversion probability with the solar axion flux, we can obtain the expected photon flux

$$\begin{aligned}\frac{\mathrm{d}\Phi_\gamma}{\mathrm{d}E} &= \frac{\mathrm{d}\Phi_a}{\mathrm{d}E}P_{a\to\gamma} \\ &= 0.088\,\mathrm{cm}^{-2}\mathrm{day}^{-1}\mathrm{keV}^{-1}E^{2.481}e^{-E/1.205}\left(\frac{g_{a\gamma\gamma}}{10^{-10}\,\mathrm{GeV}^{-1}}\right)^4\left(\frac{L}{9.26\,\mathrm{m}}\right)^2\left(\frac{B}{9.0\,\mathrm{T}}\right)^2.\end{aligned} \tag{2.89}$$

Following the discussion, helioscopes have already excluded some portion in axion parameter space and are under upgrade to get more sensitivity on the axion-photon coupling $g_{a\gamma\gamma}$. Let us see examples below.

CERN Axion Solar Telescope

The CERN Axion Solar Telescope (CAST) is one of the helioscopes trying to see axion signature and was under operation from 2003 [32], and has been upgraded through several phases until 2021 [33–39]. It is equipped with a test magnet in the Large Hadron Collider whose strength tends to be 9 T. The CAST has given upper bounds on the axion-photon

coupling $g_{a\gamma\gamma} < 6.6 \times 10^{-11}\,\mathrm{GeV}^{-1}$ for axions with the mass $m_a \lesssim 0.01\,\mathrm{eV}$, as shown in Fig. 2.16.

International Axion Observatory

International Axion Observatory (IAXO) is a forthcoming helioscope and expected to have more sensitivity on the axion-photon coupling $g_{a\gamma\gamma}$ shown by purple shaded area in Fig. 2.16.

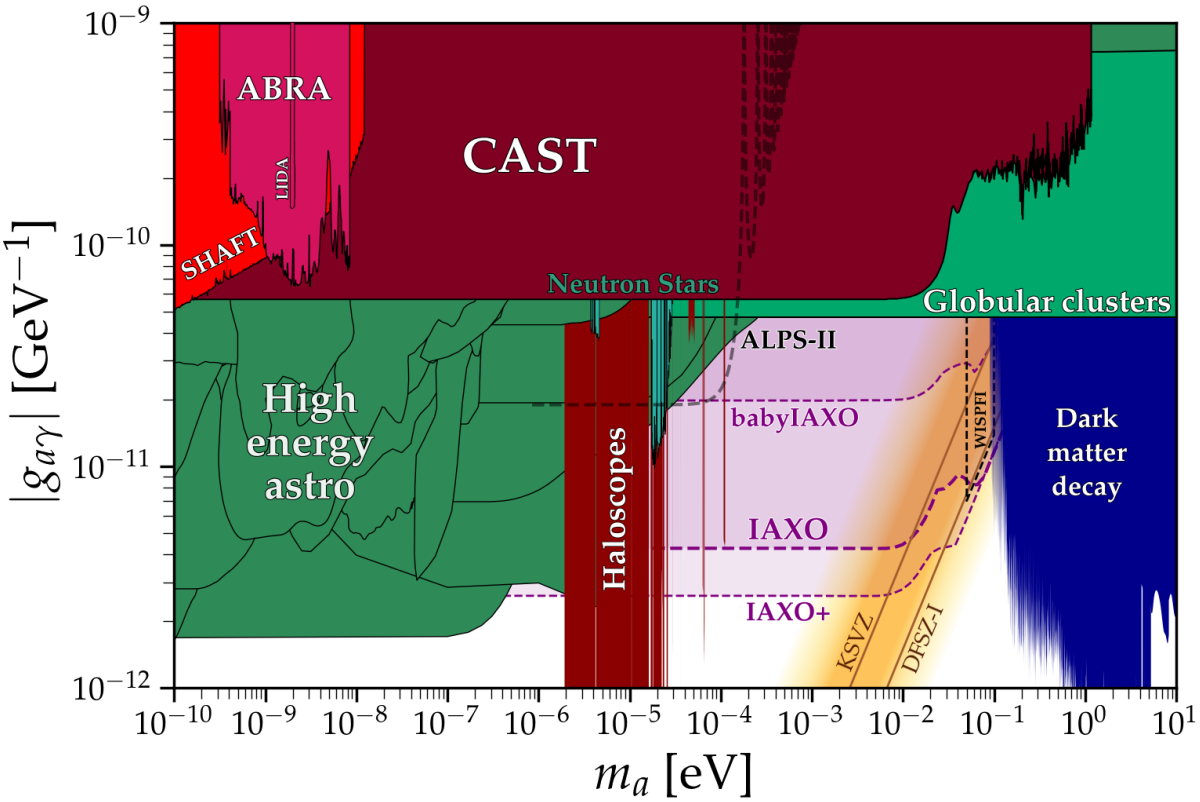

Figure 2.16: Summary of existing and expected constraints with helioscopes, light-shining-through-a-wall experiments and so on. Dark red area with "CAST" has been excluded. Purple shaded regions represent expected sensitivities of future helioscopes such as babyIAXO, IAXO, and its further upgraded version IAXO+. The yellow band correspond to axion models including the KSVZ model and the DFSZ model, which would be explored with these helioscopes in future. Green region shows existing upper limits obtained from high-energy astrophysics. Some of them will be introduced in Chapter 3. ALPS and ALPS II are light-shining-through-a-wall experiments. The ALPS II have recently reported their upper bound $g_{a\gamma\gamma} < 1.8 \times 10^{-9}\,\mathrm{GeV}^{-1}$ which located outside the figure. The ALPS II prospects are represented by black dashed line in this figure. Figure taken from [169].

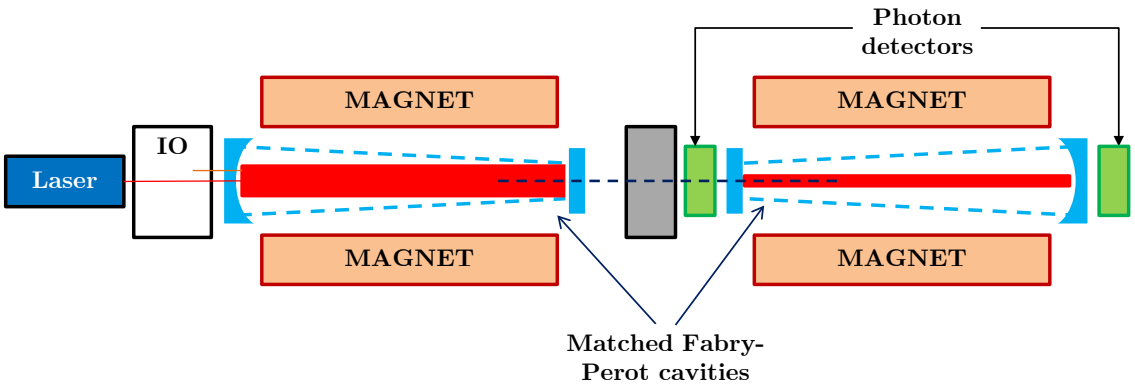

Figure 2.17: Figure taken from [30].

2.4.3 Light shining through a wall

There exist other attempts to detect axions in the laboratory. An example is so-called light shining through a wall (LSW) experiments [52–55] where induced laser beam goes toward a strong static magnetic field. A barrier is set behind the magnetic field and optical thick to the photons coming from their source. If there exist axions, the strong magnetic field can convert the photons into axions which can pass through the opaque barrier. Imposing a strong magnetic field again behind the barrier allow some of the axions to be converted back into photons which could be detected and become axion signatures. Fig. 2.17 shows a sketch of a light shining through a wall experiment. Since the axion-photon conversion occur twice in order for axions to be produced and then reconverted to photons, the probability of the double conversion $\gamma \to a \to \gamma$ is proportional to the fourth power of the axion-photon coupling $g_{a\gamma\gamma}$ as

$$P_{\gamma\to a\to\gamma} = 6 \times 10^{-34} \left(\frac{g_{a\gamma\gamma}}{10^{-10}\,\mathrm{GeV}^{-1}}\right)^4 \left(\frac{B_0}{10\,\mathrm{T}}\right)^4 \left(\frac{L}{10\,\mathrm{m}}\right)^4 \mathcal{F}_P \mathcal{F}_R \tag{2.90}$$

where $\mathcal{F}_P$ and $\mathcal{F}_R$ are the enhancement factor corresponding to power built-up by the optics systems in the production and reconversion areas, respectively. The Any Light Particle Search (ALPS) is a LSW experiment, and ALPS II is an upgraded version of the ALPS and have recently reported the first science results for the axions[1] [54]. The ALPS II is expected to finally achieve sensitivity denoted by black dashed line in Fig. 2.16.

[1]The ALPS II is also exploring other hypothetical particles such as hidden photons [54].

2.5 Summary

Chapter 2 gave us the overview of the properties and candidates of dark matter. Although it composes 26% energy of the Universe, we have not succeeded in understanding what it really is. The WIMPs are one of the most motivated dark matter candidates and have been searched experimentally in direct and indirect ways or with colliders. Experiments have started constraining broad parameter space of WIMPs although there still remain room to discuss them as a dark matter candidate. One have also payed an attention to other dark matter candidates these days. For example, the PBHs can be produced in the early universe and be account for all portion of dark matter in some mass range. The axions are also a dark matter candidate. The Peccei-Quinn mechanism motivates the QCD axions as a solution to the strong CP problem. The ALPs are kind of generalization of the QCD axions and can appear in theories beyond the SM. The ALPs also work as a dark matter candidate and have been experimentally explored in several ways.

The haloscopes try to detect the galactic halo axions with their cavity fulled with strong magnetic fields. KSVZ and DFSZ models are kinds of benchmarks of QCD axions and have been explored in some mass range $20\,\mu\text{eV} \lesssim m_a \lesssim 60\,\mu\text{eV}$ with the ADMX experiment, for instance (Fig. 2.13). The helioscopes cannot search μeV mass axions better than the haloscopes but, in sub eV mass scale, axions were explored using buffer gas techniques (Fig. 2.16). Future-planed helioscopes are expected to access QCD axion models more sensitive than existing ones. The LSW experiments have also constrained axions but their current sensitivity is weaker than other axion searches for now. With upgraded LSW experiments, one may explore competitively lighter axions as well as the helioscopes. Fig. 2.12 shows very simplified summary of existing constraints with experiments and observations including the haloscopes, the helioscopes, and the LSW experiments. Different experimental setups are responsible for axion searches in different axion mass scale and complementary with each other.

Axion searches are not limited within these experimental frameworks. We can actually have possibilities to get some information of axions with astrophysics. The green region in Fig. 2.12 have been excluded with astrophysics which gives constraints complementary to the helioscopes and the experiments in laboratories for the ALPs. For example, gamma-ray observations of high-energy astrophysical objects in the Universe are helpful for us to explore the ALPs typically in the mass $10^{-10}\,\text{eV} \lesssim m_a \lesssim 10^{-6}\,\text{eV}$. We will see how we can constrain the axion mass m_a and the axion-photon coupling $g_{a\gamma\gamma}$ with gamma-ray observations in the next chapter. Hereafter, we do not distinguish two words, axion and ALP.

Chapter 3

Axion search with gamma-ray observations

In Chapter 3, we try to grasp an idea using gamma-ray observations as a search for axions. Starting with an overview of gamma-ray propagation without and with axions, we show a workflow commonly used to constrain axions with gamma-ray observations in Section 3.1. In Section 3.2, some specific examples of such axion searches are discussed first focusing on ones with gamma rays coming from extragalactic sources, based on the workflow with some additional discussions dependent to sources we consider. Then, we find that observations of galactic sources have also constrained axions but there is still room to be improved in Section 3.3. This chapter is summarized in Section 3.4.

3.1 Light shining through the Universe

3.1.1 Overview

Before starting to discuss axion search with gamma rays, we first have to see how gamma rays propagate thorough the Universe without axions. An emission mechanism of gamma rays will be discussed in Chapter 4. After gamma rays start to propagate thorough the Universe, they interact with low-energy background photons such as star emissions, dust re-emissions and the cosmic microwave background (CMB) in the Universe, and annihilate into electrons and positrons if the gamma-ray energy is exceeding the threshold value of the process. This absorption effect makes it difficult for gamma rays to reach at the Earth from distant sources. The details of the gamma-ray absorption will be given in Chapter 4.

If there exist axions in the Universe, this story changes significantly as follows. The

Lagrangian for axions and photons are described by

$$\mathcal{L} = -\frac{1}{4}F_{\mu\nu}F^{\mu\nu} + \frac{1}{2}\,\partial_\mu a\,\partial^\mu a - \frac{1}{2}m_a^2 a^2 - \frac{1}{4}g_{a\gamma\gamma}aF_{\mu\nu}\tilde{F}^{\mu\nu} \tag{3.1}$$

where $F_{\mu\nu}$ is the field strength tensor for photons, $\tilde{F}^{\mu\nu}$ is its dual, a is the axion field with its mass m_a and coupling to photons $g_{a\gamma\gamma}$. The last term can be rewritten as $g_{a\gamma\gamma}a\mathbf{E}\cdot\mathbf{B}$ in terms of the electric field $\mathbf{E}$ and the magnetic field $\mathbf{B}$. This allows gamma rays to be converted into axions and vise versa under an external magnetic field. Since axions do not experience the same absorption process as photons, the conversion (or often called oscillation) between axions and photons can change the observed flux of the gamma rays.

After a celestial object emit an initially polarized photon beam with an energy E, its propagation can be expressed by the equations of motion derived from Eq. (3.1). In a homogeneous magnetic field, the solution for these equations provide us with a simple analytical expression for the conversion probability

$$P_{\gamma\to a}(E,L) = \left(\frac{g_{a\gamma\gamma}B_0 L}{2}\right)^2 \frac{\sin^2(\Delta_{\rm osc}L/2)}{(\Delta_{\rm osc}L/2)^2} \tag{3.2}$$

where L is the propagation distance of the axion-photon beam, and $\Delta_{\rm osc} = \sqrt{\Delta_a^2 + (2\Delta_{a\gamma})^2} = 2\Delta_{a\gamma}\sqrt{1+(E_{\rm cr}/E)^2}$. Here, $\Delta_a = -m_a^2/(2E)$, $\Delta_{a\gamma\gamma} = g_{a\gamma\gamma}B_0/2$, and $E_{\rm cr}$ is a critical energy

$$E_{\rm cr} = \frac{|m_a^2 - \omega_{\rm pl}^2|}{2g_{a\gamma\gamma}B_0} \tag{3.3}$$

$$\simeq 2.5\times10^7\,{\rm eV}\frac{|m_a^2-\omega_{\rm pl}^2|}{(10^{-10}\,{\rm eV})^2}\left(\frac{\mu{\rm G}}{B_0}\right)\left(\frac{10^{-11}\,{\rm GeV}^{-1}}{g_{a\gamma\gamma}}\right). \tag{3.4}$$

with $\Delta_{\rm pl} = -\omega_{\rm pl}^2/(2E)$ and the plasma frequency $\omega_{\rm pl}^2 = 4\pi\alpha n_e/m_e$ in an astrophysical environment with $\alpha = e^2/(4\pi)$, the electron density n_e, the electron mass m_e and the electric charge e. The derivation is shown in Section C.1.

The axion-photon conversion becomes more efficient when the gamma-ray energy E and the propagation length L respectively satisfy

$$E \gtrsim E_{\rm cr}, \quad L \gtrsim L_{\rm cr} \tag{3.5}$$

with $L_{\rm cr} = 2/(g_{a\gamma\gamma}B_0)$. In some suitable units, these conditions can be expressed as [108]

$$E_{\rm cr} \sim \frac{10\,{\rm GeV}m_{a,\,{\rm neV}}^2}{g_{11}B_{10\,\mu{\rm G}}} \sim \frac{100\,{\rm TeV}m_{a,\,{\rm neV}}^2}{g_{11}B_{\rm nG}} \sim \frac{10\,{\rm keV}m_{a,\,{\rm neV}}^2}{g_{11}B_{10\,{\rm G}}}, \tag{3.6}$$

$$L_{\rm cr} \sim \frac{10\,{\rm kpc}}{g_{11}B_{10\,\mu{\rm G}}} \sim \frac{10^3\,{\rm Mpc}}{g_{11}B_{\rm nG}} \sim \frac{0.1\,{\rm pc}}{g_{11}B_{10\,{\rm G}}}. \tag{3.7}$$

Here, these expressions based on the following notation

$$m_{a,\,{\rm neV}} \equiv \frac{m_a}{1\,{\rm neV}} \tag{3.8}$$

for the axion mass m_a,

$$g_{11} \equiv \frac{g_{a\gamma\gamma}}{10^{-11}\,{\rm GeV}^{-1}} \tag{3.9}$$

for the axion-photon coupling $g_{a\gamma\gamma}$, and

$$B_{10\,\mu{\rm G}} \equiv \frac{B_0}{10\,\mu{\rm G}}, \quad B_{\rm nG} \equiv \frac{B_0}{1\,{\rm nG}}, \quad B_{10\,{\rm G}} \equiv \frac{B_0}{10\,{\rm G}} \tag{3.10}$$

for the strength of a magnetic field B_0. Three sets of values in Eqs. (3.6) and (3.7) correspond to typical scale for the size L and the magnetic field strength B_0 associated with blazar jets, inter galactic medium, and the MW, respectively.

Fig. 3.1 shows the propagation of gamma rays passing thorough these astrophysical environments. As an example, an extragalactic blazar is considered as a source. From left to right in Fig. 3.1, we have a blazar as a gamma-ray source, its host galaxy (dark pink), its galaxy cluster (light pink), intergalactic space (white), the MW (blue), and the Earth. Gamma-rays (black wavy lines) are first produced in the blazar jet and then start its journey to the Earth. The upper black wavy line corresponds to gamma rays surviving the gamma-ray absorption and finally arriving at the Earth. The middle one shows that most of gamma rays are attenuated with the interaction with low-energy background photons such as extragalactic background lights (EBL) which is denoted by the orange wavy line. If axions in the Universe, this story can change. Since gamma-rays pass through the host galaxy and potentially through a galaxy cluster, the magnetic fields in these astrophysical environments can induce the axion-photon conversion. The lower gamma ray is converted into axions (black dashed line) with the magnetic field in the galaxy cluster, for instance. The axions can continue to propagate thorough the galaxy cluster and then the intergalactic space without the absorption process. The magnetic field in the MW can convert the axions back to gamma rays observed at the Earth. Based on this framework, gamma-ray observations have been used for axion searches as follows.

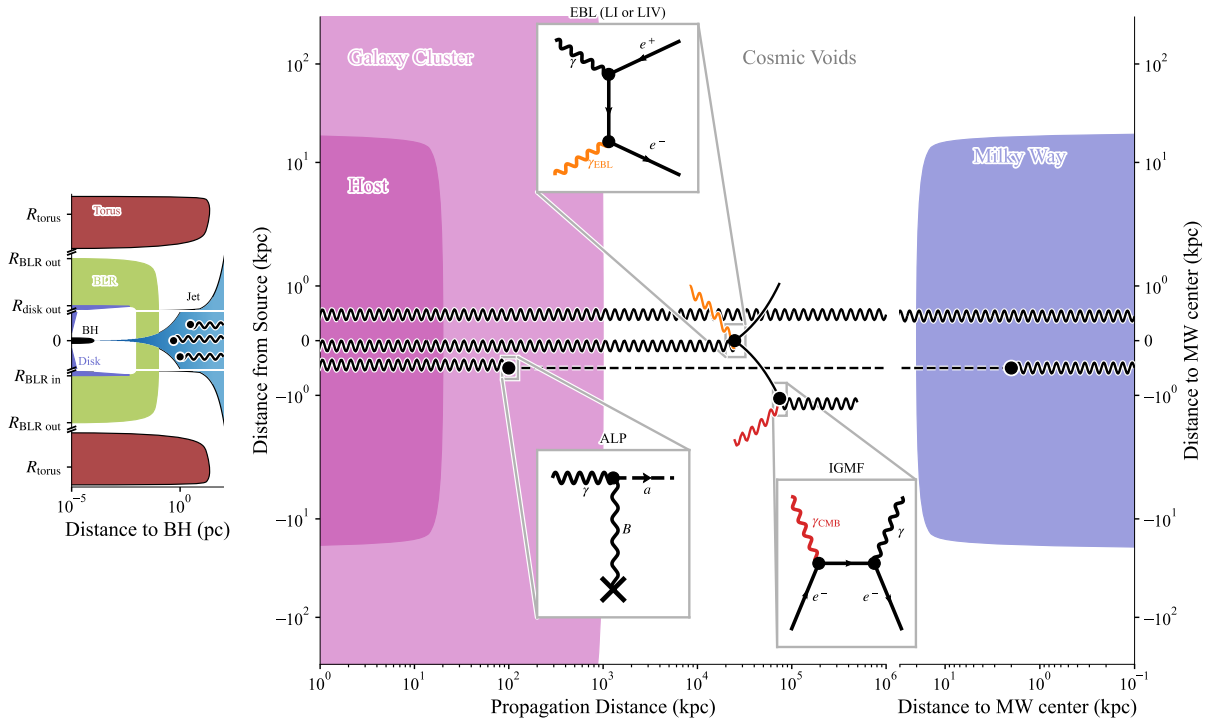

Figure 3.1: Gamma-ray propagation from a blazar to the Earth. Figure taken from [145].

3.1.2 Workflow

Now that we have briefly seen how gamma-ray spectra can be distorted by the gamma-ray absorption and the axion-photon conversion, let us next summarize common parts in a workflow for axion searches using data sets of gamma-ray observations. The workflow is applicable for the observations of both extragalactic sources (Section 3.2) and galactic ones (Section 3.3) although some differences, of course, should be taken into account.

Modeling relevant magnetic fields

It is important to consider the axion-photon conversion effect induced by magnetic fields in several astrophysical environments since it highly change the corresponding conversion probability Eq. (3.2) and then results constraining the axion mass m_a and the axion-photon coupling $g_{a\gamma\gamma}$. This urges us to take into account the profile of the magnetic field relevant to high-energy objects as precisely as possible in axion searches. Here, we show information of magnetic fields in intergalactic space and the MW. Magnetic fields associated with gamma-ray emission place in a source should be cared one by one depending what kind of sources we consider. In Sections 3.2 and 3.3, we will see some examples.

A magnetic field of the MW is commonly efficient for those examples in Sections 3.2 and 3.3. It is known that the magnetic field in the MW is described by the model developed by Jansson and Farrar [170] which are used in axion searches not only with galactic sources but also extragalactic ones. It consists of a large-scale regular component and a small-scale random one. The coherence length of the latter is about $10^{-2}\,\mathrm{pc}$ much smaller than the former, and the latter is neglected in the axion-conversion. The magnetic field strength of regular component varies between $1.4 - 4.4\,\mu\mathrm{G}$.

For extragalactic sources, the axion-photon beam passes thorough the intergalactic space where the magnetic field strength is currently bounded above $\lesssim 10^{-9}\,\mathrm{G}$. The lower limits locate at $10^{-8}\,\mathrm{nG}$ scale. When a source redshift is relatively small, one did not expect strong irregularities in gamma-ray spectra induced by the axion-photon conversion by the intergalactic magnetic field, as discussed in e.g. [132–134] where the authors have neglected the effect of the axion-photon conversion in the intergalactic space.

Calculation of survival probability

The conversion probability Eq. (3.2) determines how many gamma rays from a source convert into axions which are not attenuated with the low-energy background photons as

we have discussed. The expression Eq. (3.2) was obtained under the homogeneous magnetic field but axion-photon beams actually travel in inhomogeneous magnetic fields in a realistic astrophysical environment. In order to consider such environments as precisely as possible, we can solve the equations of motion using a transfer-matrix formalism which will be explained in Section 4.1. The numerical calculations give us the probability corresponding how much gamma-ray flux will survive after the gamma-ray absorption and axion-photon conversion. We denote the survival probability by $P_{\gamma\gamma}$. It will be multiplied with an intrinsic spectrum $\Phi_{\rm int}$ to compute an expected spectrum.

Calculation of expected spectra

Intrinsic gamma-ray spectra depend on sources and the corresponding datasets. For axion searches, one have usually used an expression to model the intrinsic spectrum $\Phi_{\rm int}(E)$ which fit well with observed gamma-ray data. Here, E is the gamma-ray energy. The following expressions are some examples and listed for references later. We will see cases where those are used in axion searches with gamma-ray observations in Sections 3.2 and 3.3.

- **Power law spectrum**

$$\Phi_{\rm int}(E) = N_0 \left(\frac{E}{E_0}\right)^{-\Gamma} \tag{3.11}$$

- **Exponential cutoff power law**

$$\Phi_{\rm int}(E) = N_0 \left(\frac{E}{E_0}\right)^{-\Gamma_1} \exp\left[-\left(\frac{E}{E_{\rm cut}}\right)^{\Gamma_2}\right] \tag{3.12}$$

- **Log parabola spectrum**

$$\Phi_{\rm int}(E) = N_0 \left(\frac{E}{E_0}\right)^{-\alpha-\beta\log(E/E_0)} \tag{3.13}$$

Here, N_0 is the normalization of the spectrum, and the indices are denoted by Γ, Γ_1, Γ_2, α, and β. E_0 is the reference scale. Other expressions are occasionally used for some sources but we do not list all of them here. We can then calculate the expected spectrum as $\Phi_{\rm model} = P_{\gamma\gamma}\Phi_{\rm int}$.

Statistical analysis

We then address a statistical analysis where we optimize the expected spectrum to some datasets and calculate a test statistic for each parameter set (m_a, $g_{a\gamma\gamma}$) in scanned parameter space. This finally allows us to constrain the axion mass m_a and the axion-photon coupling $g_{a\gamma\gamma}$ after getting the threshold corresponding to a confidence level. In Section 4.3, we will introduce a method for the statistical analysis used in this thesis.

The workflow introduced in this subsection is summarized in Fig. 3.2. It is applied to specific examples of axion searches with gamma rays from extragalactic sources in Section 3.2 and galactic sources in Section 3.3 unless otherwise stated.

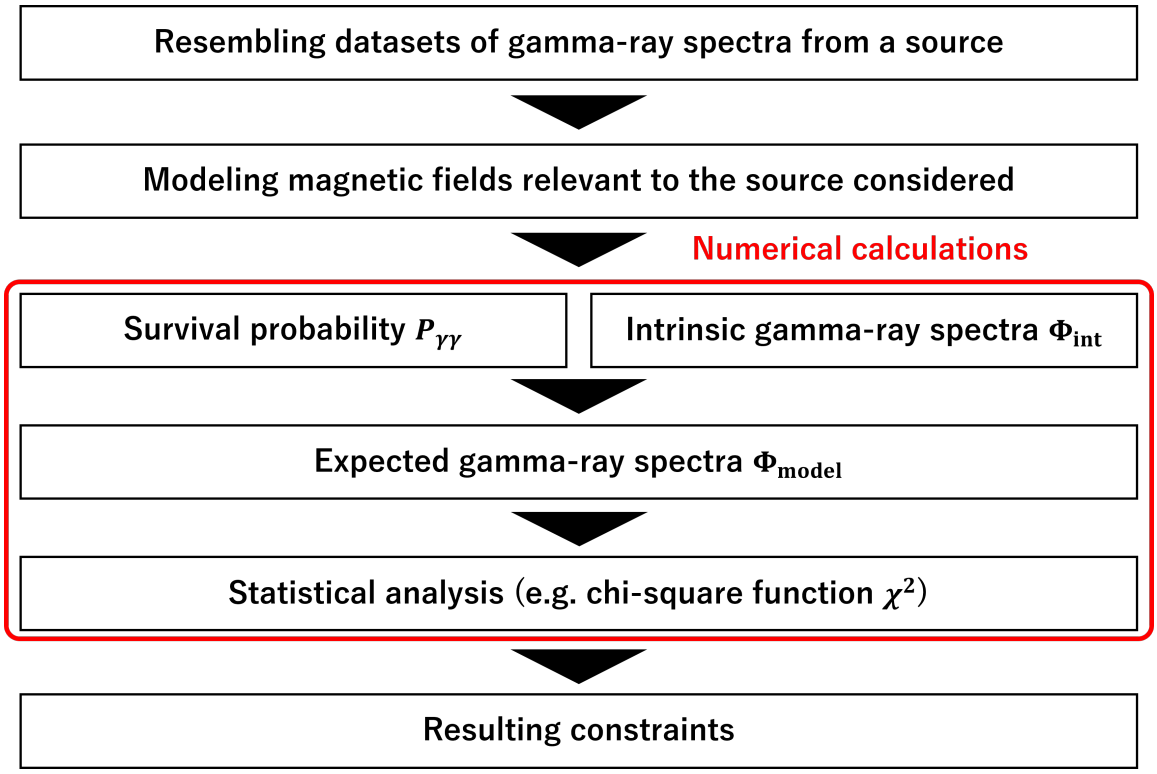

Figure 3.2: Workflow used in axion searches with gamma-ray observations.

3.2 Examples: extragalactic sources

In this section, we see some specific examples of existing constraints on axions obtained from gamma-ray observations of extragalactic sources such as active galactic nuclei (AGN). Since we have already showed the workflow common in these examples in Section 3.1, let us next focus on differences between them. Models of magnetic fields are the most important difference depending on what kind of celestial objects we consider.

3.2.1 Active galactic nuclei

Super massive black holes power AGN with matter accreted around their surroundings. The accretion disc formed surrounding the black hole is one of main contributions to the total luminosity of an AGN for its non-thermal emissions. Highly collimated relativistic jets extend from sub-parsec to kilo-parsec scales and also play a key role of the non-thermal emission. Magnetic fields within AGN jets tend to be $B_0 \sim 10\,\mathrm{G}$ and are essential for the axion-photon conversion. For example, NGC 1275 [132–134] and Markarian 421 (Mrk 421) [135–138] have been used to impose limits on the axion parameters.

NGC 1275 in the Perseus Galaxy Cluster

The NGC 1275 is the radio galaxy located in the center of the Perseus Galaxy Cluster at a distance of $\sim 75\,\mathrm{Mpc}$ ($z = 0.01756$). As mentioned in Section 2.1, galaxy clusters are the largest gravitationally bound structures in the Universe. Their intra-cluster medium is composed of hot, highly ionized gas with temperatures $T \sim 10^7$ to $10^8\,\mathrm{K}$. Faraday rotation measurements and magneto-hydrodynamical simulations imply that galaxy clusters have a turbulent magnetic field whose strength is ranging from $0.1\,\mu\mathrm{G}$ to a few μG. The magnetic field can induce the axion-photon conversions for gamma rays propagating for cosmological distance from the NGC 1275.

For example, Fermi-LAT [132], Major Atmospheric Gamma Imaging Cherenkov telescopes (MAGIC) [133] and Very Energetic Radiation Imaging Telescope Array System (VERITAS) [134] collaborations have used their datasets of the observed gamma rays to constrain axions, for which modeling of the magnetic field is important. They modeled the turbulent component as a divergence-free homogeneous and isotropic field with Gaussian turbulence with zero mean and a variance σ_B. The profile of the magnetic field is given by

$$B(r) = B_0 \left(\frac{n_e(r)}{n_e(r=0)} \right)^{\eta} \tag{3.14}$$

where $n_e(r)$ is the electron density of the intra-cluster medium (ICM). The energy density $M(k)$ is considered to follow

$$M(k) \propto k^q \Theta(k - k_L)\Theta(k_H - k) \tag{3.15}$$

where $k_L = 2\pi/\Lambda_{\rm max}$ and $k_H = 2\pi/\Lambda_{\rm min}$ are the minimum and maximum turbulence scales, respectively.

The authors [132] used $n_e(r)$ derived from X-ray observations within the inner $r_{\rm max} = 500\,{\rm kpc}$ for the Perseus galaxy cluster. They assume a zero magnetic field beyond $r_{\rm max}$. There are rotation measurements to explore only within tens of pc around the NGC 1275. These measurements estimated that the magnetic field strength was $25\,\mu{\rm G}$ ([132] and references therein). There is an independent lower limit of $B_0 \gtrsim 2{-}13\,\mu{\rm G}$ for $0.3 \lesssim \eta \lesssim 0.7$ derived by MAGIC observations of the Perseus galaxy cluster. The authors [132] applied values of parameters obtained from rotation measurements of other galaxy cluster (A 2199). They finally assume model parameters take the values in Table 3.1 and set their constraints denoted by "NGC 1275 (Fermi)" in Fig. 3.3.

parameter	value
σ_B	$10\,\mu$G
$r_{\rm max}$	500 kpc
η	0.5
q	-2.8
$\Lambda_{\rm min}$	0.7 kpc
$\Lambda_{\rm max}$	35 kpc

Table 3.1: Model parameters for the magnetic field in Perseus galaxy cluster used in [132].

Markarian 421

Several works used gamma-ray observations of the Mrk 421 for axion searches [135–138]. The Mrk 421 is one of the brightest blazars ($z = 0.031$) in TeV gamma rays and widely studied.

Magnetic field in the blazar jet can induce the axion-photon conversion and its effect have been investigated. The astrophysical environment of the Mrk 421 is modeled by the

magnetic field $B^{\rm jet}(r)$ and the electron density $n_e^{\rm jet}(r)$ whose profiles are

$$B^{\rm jet}(r) = B_0 \left(\frac{r}{r_{\rm VHE}}\right)^{-1}, \tag{3.16}$$

$$n_e^{\rm jet}(r) = n_0 \left(\frac{r}{r_{\rm VHE}}\right)^{-2} \tag{3.17}$$

where $r_{\rm VHE}$ is the distance of the emission site to the black hole at the center. B_0 and n_0 are the magnetic field strength and the electron density at $r_{\rm VHE}$, respectively. Best-fit values of some parameters including B_0 and n_0 are obtained from fitting of the electromagnetic wave spectrum to the data. However, the precise value of $r_{\rm VHE}$ is difficult to be derived from the observations and it has large uncertainty with an order of magnitude. Optimistic values for $r_{\rm VHE}$ were sometimes chosen within this uncertainty. This can give a less conservative limits on the axion parameters. More details of the blazar jet magnetic field are discussed in [135–138] and references therein.

The axion-photon beam starts to feel magnetic field in the host galaxy cluster of the Mrk 421 after it passes thorough the blazar jet region, as sketched in Fig. 3.1. In the case of the NGC 1275, [133] considered the axion-photon conversion induced by $\mathcal{O}(1\,\mu{\rm G})$ magnetic field in the Perseus Galaxy Cluster. However, the authors of [135] did not consider the axion-photon conversion in the inter-cluster region because it has not to be confirmed that the Mrk 421 is located on such a galaxy cluster with magnetic fields strong enough to cause the axion-photon conversion. Magnetic fields in the intergalactic space and the MW are treated in the same way discussed in Section 3.1.

Based on the modeling of these magnetic field environments, the survival probability was calculated in the case of the Mrk 421 [135–138]. In [135, 136], the authors used the observational data of the Mrk 421[1] associated with each observation phase a day and finally combined them to get stronger constraints on the axion parameters. For example, 15 phases of the gamma-ray observation were used and then combined in [136]. For each observation phase, a function was chosen among Eqs. (3.11) to (3.13) etc. as an intrinsic gamma-ray spectrum. Datasets in some phases could not individually set limits exceeding the upper bounds by the CAST [38]. In [137], the authors utilized different datasets of the Mrk 421 observed for three years by the Fermi-LAT and High Altitude Water Cherenkov (HAWC) Gamma-Ray Observatory. The datasets were fitted by the exponential cutoff power law Eq. (3.12) which was used as the intrinsic gamma-ray spectrum. Resulting constraints on axions are summarized in Fig. 3.3. Colored region with "Mrk 421" has been excluded by its gamma-ray observations.

[1] In [136], some datasets of a blazar (PG 1553+113) were also used in addition to ones of the Mrk 421.

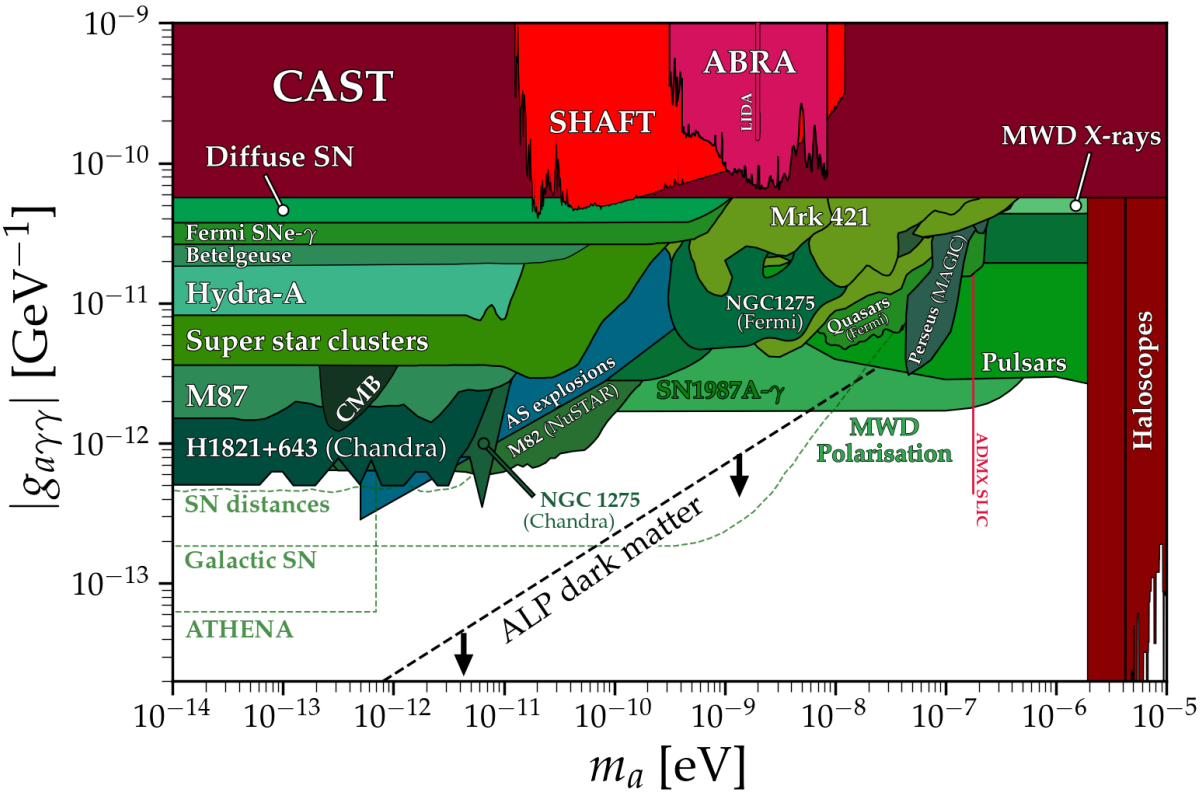

Figure 3.3: Constraints on axions with astrophysics denoted by green area including gamma-ray search. The observations of extragalactic sources introduce above have constrained green region, e.g. the NGC 1275 within the Perseus galaxy cluster [132, 133], the Mrk 421 [135–138] and quasars [131]. The red space shows the existing constraints with the CAST [39] and haloscopes including the ADMX [50]. Other constraints are listed in [169] from which the figure are taken.

3.3 Examples: galactic sources

In addition to extragalactic sources, galactic gamma-ray sources have also been used for axion searches [139–144]. In this section, we will see that gamma-ray observations of supernova remnants (SNRs) and pulsar wind nebulae (PWNe) in the MW have given constraints on axions [139–141]. Especially, the Crab Nebula [142–144] is the most relevant to the contents in Chapter 4.

3.3.1 Supernova remnants and pulsar wind nebulae

Zi-Qing Xia et al. (2018/2019)

Three SNRs (IC443, W44 and W51C) were used to see oscillation effects induced by axions [139] with gamma-ray spectra observed by the Fermi-LAT. Intrinsic spectra of these SNRs were modeled by the log-parabola type functions Eq. (3.13) where E_0 is fixed to the default value in the Third Fermi-LAT catalog (3FGL). The expected spectra were fitted to the gamma-ray spectra, and the fitting result was improved by the axion-photon conversion with a statistical significance of 4.2σ for IC443. However, the best-fit parameter ($m_a = 6.6\,\mathrm{neV}$ and $g_{a\gamma\gamma} = 13.4 \times 10^{-11}\,\mathrm{GeV}^{-1}$) contradicted with the upper bound given by the CAST [38].

The same group has then considered three SNRs [141] to constrain axions. The two of them (IC443 and W51C) were the same as [139] while W49B was newly chosen in their analysis. In addition, they have also used gamma-ray data observed by several Imaging Atmospheric Cherenkov Telescopes (IACTs) such as the MAGIC, VERITAS and High Energy Stereoscopic System (H.E.S.S.). The intrinsic spectra were modeled by a log-parabola function Eq. (3.13) following the Fourth Fermi-LAT catalog (4FGL). As opposed to their previous analysis [139], the spectral parameter E_0 was unfixed for their optimizations. The authors have set constraints on axion parameters with the combined analysis of all the three SNRs they have chosen. However, their constraint was not able to exceed one by the CAST [38].

Yun-Feng Liang et al. (2019)

They have also tried to constrain axions with other 10 gamma-ray sources [140] including three SNRs, five PWNe, one high-mass X-ray binary, and another is unidentified. They all have been observed by the H.E.S.S. experiment. We do not list them here but available in Table 1 of [140]. Intrinsic spectra for these gamma-ray sources were characterized by two types of functions, a power-law Eq. (3.11) or an exponential cutoff power law

Eq. (3.12). The specific function type was chosen for each source as that in the literature. Their constraint combined with the 10 sources is shown in Fig. 3.4. The yellow region was excluded by the combined analysis at 95% confidence level. At the axion mass $m_a \sim 10^{-7}\,\mathrm{eV}$, the resulting constraint is exceeding the CAST one [38].

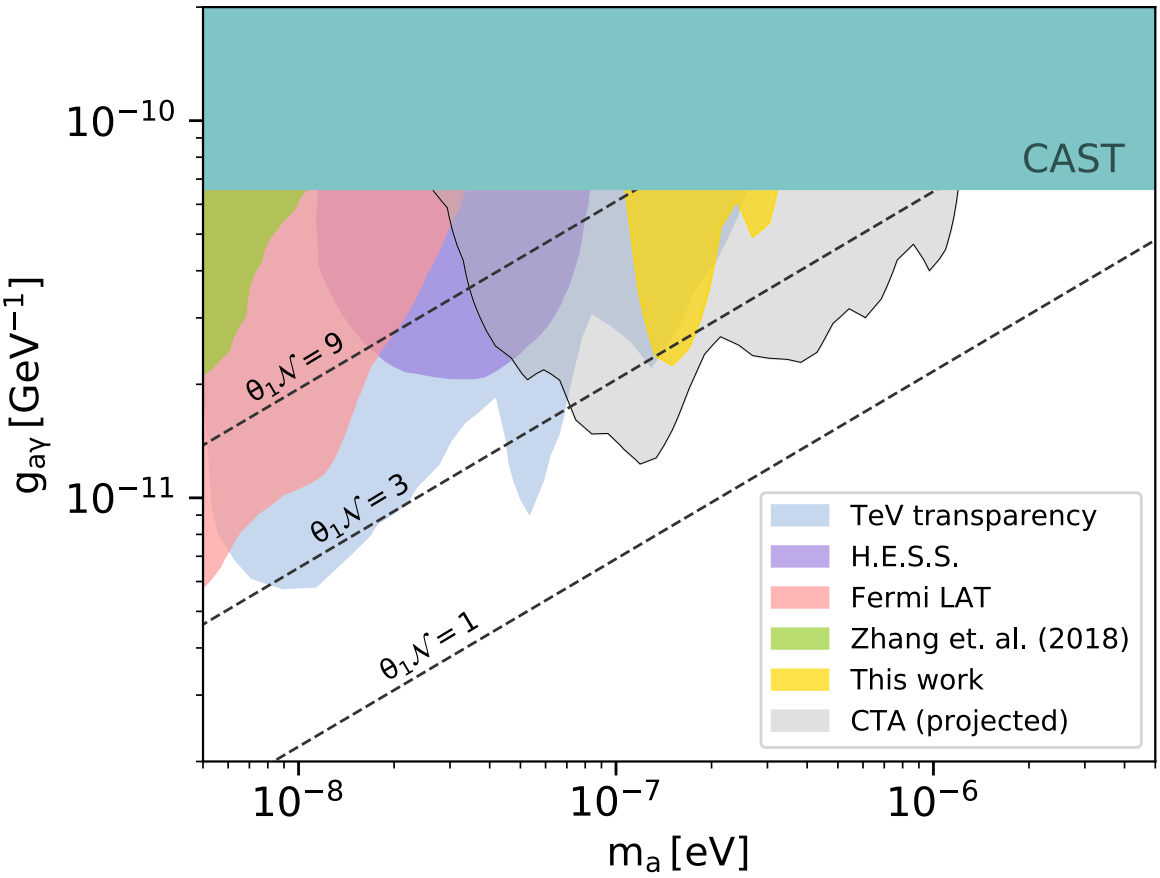

Figure 3.4: The yellow area corresponds to constraint by [140]. The red region is excluded by the observation of the NGC 1275 by the Fermi-LAT [132]. Figure taken from [140].

3.3.2 Crab Nebula

The Crab Nebula is one of the famous PWNe in our galaxy. Astrophysicists have studied well the Crab Nebula for long time based on observations from radio to gamma rays. The maximum energy of the observed gamma rays tend to PeV scale which have been detected by the LHAASO [156]. Such observed data sets allowed us to develop more precise emission models of the Crab Nebula [158, 159] which will be discussed in Chapter 4. In this subsection, we show the existing results to impose constraints on axions with gamma rays from the Crab Nebula [142, 143] and then point out a missing piece in these analyses.

Xiao-Jun Bi et al. (2021)

In [142], the authors have taken the Crab Nebula as the main target for their axion search with gamma rays[2]. They considered the gamma-ray absorption and the axion-photon conversion in the magnetic field of the MW since the Crab Nebula is a galactic source. After numerically calculating the survival probability and then expected gamma-ray spectrum, the authors compare it with the observed data sets given by several gamma-ray observation groups. Their analysis revealed that their resulting constraint on axions could not exceed one with CAST as a benchmark result. In Fig. 3.5, the red region shows their constraint [142] and the black-dashed line is the upper bound by the CAST [38].

Jun Li et al. (2024)

The LHAASO released their reports of detections of the Crab Nebula [156] and twelve ultra-high-energy gamma-ray sources [171]. In order to set constraints on axions, the authors of [143] have used datasets of gamma rays from four of them (the Crab Nebula, LHAASO J2226+6057, LHAASO J1908+0621, and LHAASO J1825-1326). For these energetic sources, they have modeled intrinsic gamma-ray spectra with a log-parabola function Eq. (3.13) where E_0 is set to be 10 TeV. As a result, their combined analysis of the four sources set a limit on the axion-photon coupling $g_{a\gamma\gamma} \lesssim 7.2 \times 10^{-11}\,\mathrm{GeV}^{-1}$ at the axion mass $m_a \sim 4 \times 10^{-7}\,\mathrm{eV}$, as shown by blue region in Fig. 3.5. However, their constraint was weaker than the CAST result (black-dashed line) [38] even if they tried to get stronger constraints by combining datasets from other six gamma-ray facilities in addition to the LHAASO.

[2] [142] has also tried to set dark photon limits with gamma rays from the Crab Nebula.

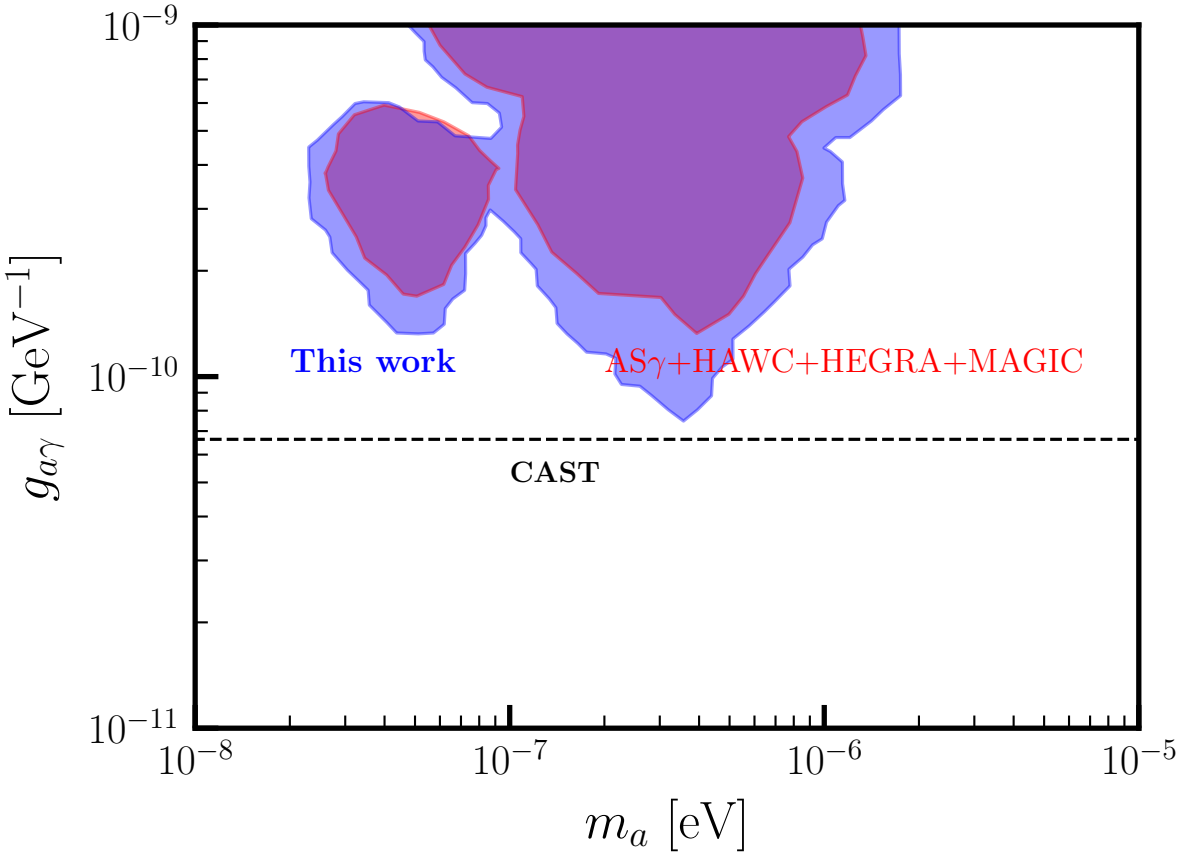

Figure 3.5: Constraints on axions with gamma-ray observations of the Crab Nebula without [142] and with the LHAASO observation [143], corresponding to red and blue region, respectively. The black-dashed line is the CAST upper bound [38]. Figure taken from [143].

Kazunori Kohri and Haruki Takahashi (2025)

There actually exists a missing piece in these kind of analyses: magnetic field in the Crab Nebula. It is known that the magnetic field in the Crab Nebula is important to explain broad emissions of electromagnetic waves from the Crab Nebula through the so-called synchrotron self-Compton (SSC) mechanism as explained in Chapter 4. Considering the magnetic field in the Crab Nebula can affect the axion-photon conversion and then alter constraints on axions. In fact, it actually does [144]. This point has been missed so far but should be taken into account, as pointed out in [144]. In Chapter 4, we will discuss importance of the magnetic field in the Crab Nebula not only for broad-band spectrum of photons but also for axion search with gamma-ray observations of the Crab Nebula.

3.4 Summary

The gamma-ray observations are an alternative way to get information for axions in addition to other axion searches such as the axion helioscopes, the axion haloscopes, the LSW experiments and so on. From celestial objects, gamma rays propagate through several magnetic field environments in the Universe and can experience the axion-photon conversion. This can alter the gamma-ray spectra and can be used to constrain the axion mass m_a and the axion-photon coupling $g_{a\gamma\gamma}$. When we take this kind of approach for axion search, it is important to take into account magnetic fields for analyses as precisely as possible.

On the one hand, for extragalactic sources such as blazars, we saw that one could consider magnetic fields in their jet and in the galaxy cluster to put constraints on axions in Section 3.2. Since extragalactic sources are located far from the Earth, constraints obtained with extragalactic sources are naively expected to be generally stronger than ones with galactic sources. Fig. 3.3 includes the constraints with gamma rays from some extragalactic sources such as the NGC 1275 [132, 133], the Mrk 421 [135–138], quasars [131] and so on. However, such analyses have still uncertainties coming from modeling of emission mechanisms and magnetic fields.

On the other hand, galactic sources (e.g. SNRs and PWNe) have also been used for axion searches with gamma-ray observations and some of them are well-studied using broadband emissions from radio to gamma rays. The Crab Nebula is a good example and its emission mechanism is understood well as explained in Chapter 4. Nevertheless, the magnetic field in the Crab Nebula have not been taken into account in the context of axion searches so far. In the next chapter, we discuss effects of the magnetic fields of the Crab Nebula and in fact reveal that this consideration gives us new constraints on axions with gamma rays from the Crab Nebula.

Chapter 4

New constraints on axions with gamma rays from the Crab Nebula

In Chapter 4, we discuss effects of the magnetic field around the Crab Nebula on axion search with gamma rays based on [144]. In Section 4.1, we first show how we can characterize the effects of the gamma-ray absorption and the axion-photon conversion. Section 4.2 introduces emission models of electromagnetic waves from the Crab Nebula including the model for the magnetic field around the source, which is important not only for the intrinsic gamma-ray emission but also for the axion-photon conversion. In Section 4.3, we perform statistical analyses based on the developed model and constrain the axion mass m_a and the axion-photon coupling $g_{a\gamma\gamma}$, and show that the magnetic field in the Crab Nebula also contribute to the axion-photon conversion and give new constraints on the axion parameters. Section 4.4 is devoted to summarize this chapter.

4.1 Axion-photon conversion

The system of axions a and photons A_μ is described by the following Lagrangian

$$\mathcal{L} = -\frac{1}{4}F_{\mu\nu}F^{\mu\nu} + \frac{1}{2}\,\partial_\mu a\;\partial^\mu a - \frac{1}{2}m_a^2 a^2 - \frac{1}{4}g_{a\gamma}aF_{\mu\nu}\tilde{F}^{\mu\nu}, \tag{4.1}$$

where a is the axion field, m_a denotes the axion mass, and $g_{a\gamma}$ is the axion-photon coupling. Here, $F_{\mu\nu}$ and $\tilde{F}_{\mu\nu}$ are the electromagnetic field strength tensor and its dual, respectively. Axions and photons are mixing with each other through the axion-photon coupling, which can be written as $g_{a\gamma}a\boldsymbol{E}\cdot\boldsymbol{B}$ in terms of the electric field $\boldsymbol{E}$ and magnetic field $\boldsymbol{B}$. Axion-photon beams with a monochromatic energy E are propagating along x_3-direction under

magnetic fields. The propagation can be described by the equation [172]

$$\left(i\frac{\mathrm{d}}{\mathrm{d}x_3} + E + \mathcal{M}\right)\Psi(x_3) = 0 \tag{4.2}$$

where $\mathcal{M}$ is the mixing matrix and $\Psi(x_3) = (A_1(x_3), A_2(x_3), a(x_3))^T$. Neglecting Faraday rotation effects, the mixing matrix $\mathcal{M}$

$$\mathcal{M} = \begin{pmatrix} \Delta_\perp & 0 & 0 \\ 0 & \Delta_\parallel & \Delta_{a\gamma} \\ 0 & \Delta_{a\gamma} & \Delta_a \end{pmatrix}. \tag{4.3}$$

has several components such as $\Delta_\perp = \Delta_{\rm pl} + 2\Delta_{\rm QED} - i\Gamma/2$, $\Delta_\parallel = \Delta_{\rm pl} + 7\Delta_{\rm QED}/2 - i\Gamma/2$, $\Delta_a = -m_a^2/(2E)$ corresponding to the kinetic term of axions, and $\Delta_{a\gamma} = g_{a\gamma}B/2$ resulting in the axion-photon conversion. The plasma term $\Delta_{\rm pl} = -\omega_{\rm pl}^2/(2E)$ is arising from the effective photon mass in plasma of astrophysical environments where $\omega_{\rm pl} = \sqrt{4\pi n_e e^2/m_e}$ with the electron density n_e, the electric charge e, and the electron mass m_e. QED vacuum polarization effects appear in $\Delta_{\rm QED} = \alpha E/(45\pi)(B/B_{\rm cr})^2$ where α is the fine structure constant and $B_{\rm cr} = m_e^2/|e| \sim 4.4 \times 10^{13}\,\mathrm{G}$. Γ characterizes the absorption effect of high-energy gamma rays as explained below.

As briefly mentioned in Section 3.1, high-energy gamma rays are absorbed through the pair production process where they interact with low-energy background photons and annihilate into electrons and positrons. CMB and interstellar radiational fields including star light emission and its dust re-emission [173–175] act as the low-energy background photons. This process occurs when gamma-ray energy is exceeding its threshold value

$$E_{\rm th} \sim \frac{4m_e^2}{\epsilon} \sim 0.5\,\mathrm{TeV}\left(\frac{\epsilon}{1\,\mathrm{eV}}\right)^{-1} \tag{4.4}$$

with the energy of background photons ϵ. The absorption effect is characterized by

$$\Gamma = \int d\epsilon \frac{\mathrm{d}n_{\rm bg}}{\mathrm{d}\epsilon}\int_0^2 d\cos\theta \frac{1-\cos\theta}{2}\sigma_{\gamma\gamma} \tag{4.5}$$

where $\mathrm{d}n_{\rm bg}/\mathrm{d}\epsilon$ is the spectrum of the background photons, θ is the collision angle between the high-energy gamma rays and the background photons. The cross section $\sigma_{\gamma\gamma}$ is written as

$$\sigma_{\gamma\gamma} = \frac{3}{16}\sigma_T(1-\beta^2)\left[2\beta(\beta^2-2) + (3-\beta^4)\ln\left(\frac{1+\beta}{1-\beta}\right)\right] \tag{4.6}$$

where σ_T is the Thomson cross section and $\beta = 1 - 4m_e^2/s$ with the Mandelstam variable

$s = 2E\epsilon(1 - \cos\theta)$.

The axion-photon conversion and the gamma-ray absorption affect on the gamma-ray spectrum. We can numerically calculate these effects with a public code `gammaALPs` [176] based on an equation of transfer matrices as follows. We first rewrite Eq. (4.2) as

$$i\frac{\mathrm{d}\rho}{\mathrm{d}x_3} = [\rho, \mathcal{M}] \tag{4.7}$$

in terms of the density matrix $\rho(x_3) = \Psi(x_3)\Psi(x_3)^\dagger$. Its solution

$$\rho(z) = \mathcal{T}(x_3, 0; E)\rho(0)\mathcal{T}^\dagger(x_3, 0; E) \tag{4.8}$$

can be obtained with the transfer matrix $\mathcal{T}$ which is the solution of Eq. (4.2) under initial condition $\mathcal{T}(0, 0; E) = 1$. Transfer matrices can be calculated for each environment corresponding to the Crab Nebula $\mathcal{T}_1$ and the MW $\mathcal{T}_2$. For the environment in MW, we use Jansson & Farrar model [170] which have been used in axion searches with gamma-ray observations. Models for the Crab Nebula are taken from [159] and explained in Section 4.2. In each environment, we assume that the propagation path can be divided into $N_i\,(i = 1, 2)$ domains where astrophysical quantities such as the magnetic field and electron density are constant [176]. The transfer matrix in total path of axion-photon beams is given by

$$\mathcal{T}_{\mathrm{total}} = \prod_{i=1}^{2}\prod_{n=1}^{N_i}\mathcal{T}_i(x_{3,[N_i-n+1]}, x_{3,[N_i-n]}; E) \tag{4.9}$$

where $x_{3,0}$ is the x_3 coordinate closest to the Crab Nebula. We then obtain an expression for the photon survival probability

$$P_{\gamma\gamma} = \mathrm{Tr}\left((\rho_{11} + \rho_{22})\mathcal{T}_{\mathrm{total}}\rho(0)\mathcal{T}^\dagger_{\mathrm{total}}\right) \tag{4.10}$$

where $\rho_{11} = \mathrm{diag}(1, 0, 0), \rho_{22} = \mathrm{diag}(0, 1, 0)$, and $\rho(0) = \mathrm{diag}(1/2, 1/2, 0)$ for unpolarized gamma rays.

4.2 Modeling the Crab Nebula

4.2.1 Electrons and magnetic fields in the Crab Nebula

We explain the model for the broadband emission of the Crab Nebula [159]. Electrons and positrons are distributed around the Crab Nebula. These spectra are characterized with a power-law by the first-order Fermi acceleration. We refer to both electrons and

positrons as electrons below. The accelerated electron distribution in the Crab Nebula is radially symmetric and steady in this model, and assumed to have two components: radio electrons and wind electrons. Radio electrons are contributing as synchrotron emission from radio to optical regime. At higher energy, synchrotron emission from the wind electrons is dominant. The total electron spectrum $n_e(\gamma, r)$ is characterized as

$$n_e(\gamma, r) = n_{\rm radio}(\gamma, r) + n_{\rm wind}(\gamma, r). \tag{4.11}$$

with the electron's Lorentz factor γ and distance from the center of the Crab Nebula r.

For the radio electrons, [159] assumed that their spectrum $n_{\rm radio}(\gamma, r)$ follows a power law from $\gamma_{r,\rm min}$ and has a super-exponential cutoff around $\gamma_{r,\rm max}$,

$$n_{\rm radio}(\gamma, r) = \frac{n_{r,0}}{\rho_r^3}\gamma^{-s_r} \exp\left[-\left(\frac{\gamma}{\gamma_{r,\rm max}}\right)^{\beta_{\rm min}}\right] \Theta(\gamma - \gamma_{r,\rm min}) F_{\rm radio}(r), \tag{4.12}$$

$$F_{\rm radio}(r) = \exp\left(-\frac{r^2}{2\rho_r^2}\right) \Theta(r - r_s), \tag{4.13}$$

where $n_{r,0}$ is the normalization, s_r is the index, $\beta_{\rm min}$ is responsible for the super-exponential cutoff, and $\Theta(x)$ is the Heaviside step function. $F_{\rm radio}(r)$ shows the radial dependence of the electron spectrum and follows a Gaussian function with constant width ρ_r.

Wind electron spectrum $n_{\rm wind}(\gamma, r)$ is modeled as

$$n_{\rm wind}(\gamma, r) = \frac{n_{w,0}}{\rho_w(\gamma)^3} G(\gamma) \exp\left[-\left(\frac{\gamma_{w,\rm min}}{\gamma}\right)^{\beta_{\rm min}}\right] \exp\left[-\left(\frac{\gamma}{\gamma_{w,\rm max}}\right)^{\beta_{\rm max}}\right] F_{\rm wind}(\gamma, r), \tag{4.14}$$

$$G(\gamma) = \left(\frac{\gamma}{\gamma_{w,1}}\right)^{-s_{w,1}} \left(\frac{\gamma_{w,1}}{\gamma_{w,2}}\right)^{-s_{w,2}} (1 - \Theta(\gamma - \gamma_{w,1})) \tag{4.15}$$

$$+ \left(\frac{\gamma}{\gamma_{w,2}}\right)^{-s_{w,2}} (\Theta(\gamma - \gamma_{w,1}) - \Theta(\gamma - \gamma_{w,2})) \tag{4.16}$$

$$+ \left(\frac{\gamma}{\gamma_{w,2}}\right)^{-s_{w,3}} \Theta(\gamma - \gamma_{w,2}), \tag{4.17}$$

$$F_{\rm wind}(\gamma, r) = \exp\left(-\frac{r^2}{2\rho_w(\gamma)^2}\right) \Theta(r - r_s). \tag{4.18}$$

The spectrum has super-exponential cutoffs at $\gamma_{w,\rm min}$ and $\gamma_{w,\rm max}$. $G(\gamma)$ denotes a double broken power law of the spectrum with the indexes $s_{w,1}, s_{w,2}$ and $s_{w,3}$. The spatial distribution $F_{\rm wind}(\gamma, r)$ is assumed to follow a Gaussian and also depend on the energy of the

wind electrons. Its dependence is given by

$$\rho_w(\gamma) = \rho_{w,0}\left[\left(\frac{\gamma}{9\times 10^5}\right)^2\right]^{-\alpha_w}. \tag{4.19}$$

The radio and wind electrons radiate low-energy photons through synchrotron process under magnetic fields around the Crab Nebula. For a model of magnetic fields near the Crab Nebula, we consider a variable B-field model developed in [158, 159]. In the variable B-field model, the magnetic field has a power-law profile with respect to r

$$B(r) = B_0\left(\frac{r}{r_s}\right)^{-\alpha} \tag{4.20}$$

where $\alpha\,(\geq 0)$ is the index, r_s is a shock radius, and B_0 is the magnetic field strength at r_s.

4.2.2 Emission mechanism of the Crab Nebula

Using the expressions for the distribution of electrons $n_e(\gamma, r)$ [Eq. (4.11)] and magnetic fields $B(r)$ [Eq. (4.20)], we can write down the spectral volume emissivity $j_\nu(\nu, r) \equiv dE/dt\,dV\,d\nu\,d\Omega$. For the synchrotron process, its spectral volume emissivity is expressed as

$$j_\nu^{\rm sync}(\nu, r) = \frac{1}{4\pi}\frac{\sqrt{3}e^3 B(r)}{m_e c^2}\int_1^\infty d\gamma\, n_e(\gamma, r) f_{\rm sync}\left(\frac{\nu}{\nu_c}\right) \tag{4.21}$$

where c is the speed of light and $\nu_c = 3eB\gamma^2/(4\pi m_e c)$ is the critical frequency. Note that we do not use the natural unit in this Section 4.2. The function $f_{\rm sync}(x)$ is given by

$$f_{\rm sync}(x) = \frac{x}{20}\left[(8+3x^2)\left(K_{1/3}(x/2)\right)^2 + xK_{2/3}(x/2)\left(2K_{1/3}(x/2) - 3xK_{2/3}(x/2)\right)\right] \tag{4.22}$$

where K_ξ is the modified Bessel function of kind ξ.

Low-energy photons radiated through the synchrotron process can be kicked up by high-energy electrons and become high-energy gamma rays by inverse-Compton (IC) scattering. This is called a synchrotron self-Compton (SSC) process. The emissivity of the IC scattering

$$j_\nu^{\rm IC}(\nu, r) = \frac{3\sigma_T hc}{4}\frac{h\nu}{4\pi}\int_1^\infty d\gamma\,\frac{n_e(\gamma, r)}{\gamma^2}\int_0^\infty d\epsilon\, f_{\rm IC}(\nu, \epsilon, \gamma)\frac{n_{\rm seed}(\epsilon, r)}{\epsilon} \tag{4.23}$$

can be calculated with the IC kernel function

$$f_{\rm IC}(x) = 2q\ln q + (1+2q)(1-q) + \frac{1}{2}\frac{(\Gamma_\epsilon q)^2}{1+\Gamma_\epsilon q}(1-q) \tag{4.24}$$

where σ_T is the Thomson cross section, h is the Planck constant, $\Gamma_\epsilon = 4\epsilon\gamma/(m_e c^2)$ and $q = h\nu/(\Gamma_\epsilon(\gamma m_e c^2 - h\nu))$. $n_{\rm seed}(\epsilon, r)$ denotes seed photon's density where ϵ is the energy of seed photons.

While synchrotron photons are important as seed photons of the SSC process, CMB and dust emissions are also components of seed photons. CMB photons act as not only one of seed photons but also prevent especially PeV gamma rays from propagating for long distance in the Universe [177] as explained in Section 4.1, and its density is

$$n_{\rm seed}^{\rm CMB} = \frac{4\pi}{hc}\frac{B_\nu(T_{\rm CMB})}{h\nu}. \tag{4.25}$$

where $B_\nu(T)$ is the intensity of the black body at temperature T. Dust emission was introduced to explain the observational data in the radio and optical ranges (e.g. [149]). [159] used a model where the dust emission is originated from a mixture of two populations consisting of amorphous carbon dust grains with different temperatures $T_i\,(i=1,2)$ and their masses $M_i\,(i=1,2)$. The dust populations are within a shell whose inner and outer radii are $r_{\rm in}$ and $r_{\rm out}$, respectively. The emissivity of the dust is given by

$$j_\nu^{\rm dust}(\nu, r) = \frac{3\kappa[\Theta(r-r_{\rm in}) - \Theta(r-r_{\rm out})]}{4\pi(r_{\rm out}^3 - r_{\rm in}^3)} \sum_{i=1,2} M_i B_\nu(T_i) \tag{4.26}$$

where κ is the absorption coefficient dependent on the wavelength λ

$$\kappa = 2.15\times10^{-4}\,{\rm cm^2 g^{-1}}\left(\frac{\lambda}{\mu{\rm m}}\right)^{-1.3}. \tag{4.27}$$

We can calculate the density of synchrotron and dust emissions as seed photons of SSC process

$$n_{\rm seed}^j(\epsilon, r) = \frac{r_0}{2hc}\frac{4\pi}{\epsilon}\int_{r_s/r_0}^1 dy\,\frac{y}{x}\ln\frac{x+y}{|x+y|} j_\nu^t(\nu, r_0 y), \quad (j = {\rm sync, dust}). \tag{4.28}$$

where $r_0 = 2.0\,{\rm pc}$ is the radius of the Crab Nebula. The total density of seed photons is expressed by

$$n_{\rm seed}(\epsilon, r) = \sum_k n_{\rm seed}^k(\epsilon, r), \quad (k = {\rm sync, dust, CMB}) \tag{4.29}$$

and used to calculate the IC emissivity in Eq. (4.23). The total luminosity L_ν can be calculated by integrating the emissivity in the SSC process over volume dV and solid angle $d\Omega$ as

$$L_\nu = \oint d\Omega \int dV\, j_\nu(\nu, r) = (4\pi)^2 \int_{r_s}^{r_0} dr\, r^2 \left[j_\nu^{\rm sync}(\nu, r) + j_\nu^{\rm IC}(\nu, r) \right], \tag{4.30}$$

using Eq. (4.21) and Eq. (4.23).

4.2.3 Axion-photon conversion in the Crab Nebula

This model [159] enables us to numerically calculate high-energy gamma-ray flux. We can obtain parameters for the magnetic field based on this model shown in Table 4.1. In the model of the variable magnetic field, we adopt the best-fit value $\alpha = 0.4691$ to fit the full multi-wavelength spectrum without the axions, which gives the conservative upper bound on the model parameters of the axions. However, the numerical calculations are consuming a lot of time and computer resources to fit the broad emission from radio to gamma rays. Since we would like to see how axions affect the spectrum of high-energy gamma rays only, we focus on the gamma-ray spectrum in GeV $\sim$ PeV energy range. A similar approach was taken in the case of an axion search using gamma rays from a blazar [138]. Fermi-LAT has observed the gamma rays consisted of synchrotron and IC emissions around GeV scale [178, 179], and LHAASO reported TeV and PeV gamma rays in IC part [156]. It is known that the gamma-ray spectrum in the energy scale can be well described by the following function [156, 179]

$$\Phi_{\rm int} = N_{\rm sync}^0 \left(\frac{E}{100\,{\rm MeV}} \right)^{-\Gamma_{\rm sync}} + N_{\rm IC}^0 \left(\frac{E}{1\,{\rm GeV}} \right)^{-\alpha - \beta \ln(E/1\,{\rm GeV})} \tag{4.31}$$

where $E = h\nu$ is the energy of gamma rays. A power-law spectrum with the index $\Gamma_{\rm sync}$ was used for the synchrotron part [179] while IC emission was explained by using a log-parabola spectrum whose shape is characterized by α and β [156, 179]. $N_{\rm sync}^0$ and $N_{\rm IC}^0$ are the normalization constants for synchrotron and IC emissions, respectively.

Parameter	variable B-field model
B [μG]	256.4
α	0.4691
r_s [pc]	0.13

Table 4.1: Parameters of the magnetic field in the variable B-field model taken from [159].

As explained in Section 4.1, the intrinsic spectrum of gamma rays $\Phi_{\rm int}$ emitted from the source undergoes the axion-photon conversion and the gamma-ray absorption during its propagation to the Earth. We can numerically calculate the model flux $\Phi_{\rm model}$ as

$$\Phi_{\rm model} = P_{\gamma\gamma}\, \Phi_{\rm int}. \tag{4.32}$$

The photon survival probability $P_{\gamma\gamma}$ determines how the gamma-ray spectrum can be distorted by the effects of the axion-photon conversion and gamma-ray absorption. Note that we took into account the effects of the magnetic field of the Crab Nebula on the axion-photon conversions. Since we have considered the model for magnetic fields in the Crab Nebula, this can alter constraints on the axion mass m_a and the coupling to photons $g_{a\gamma\gamma}$ as discussed in Section 4.3.

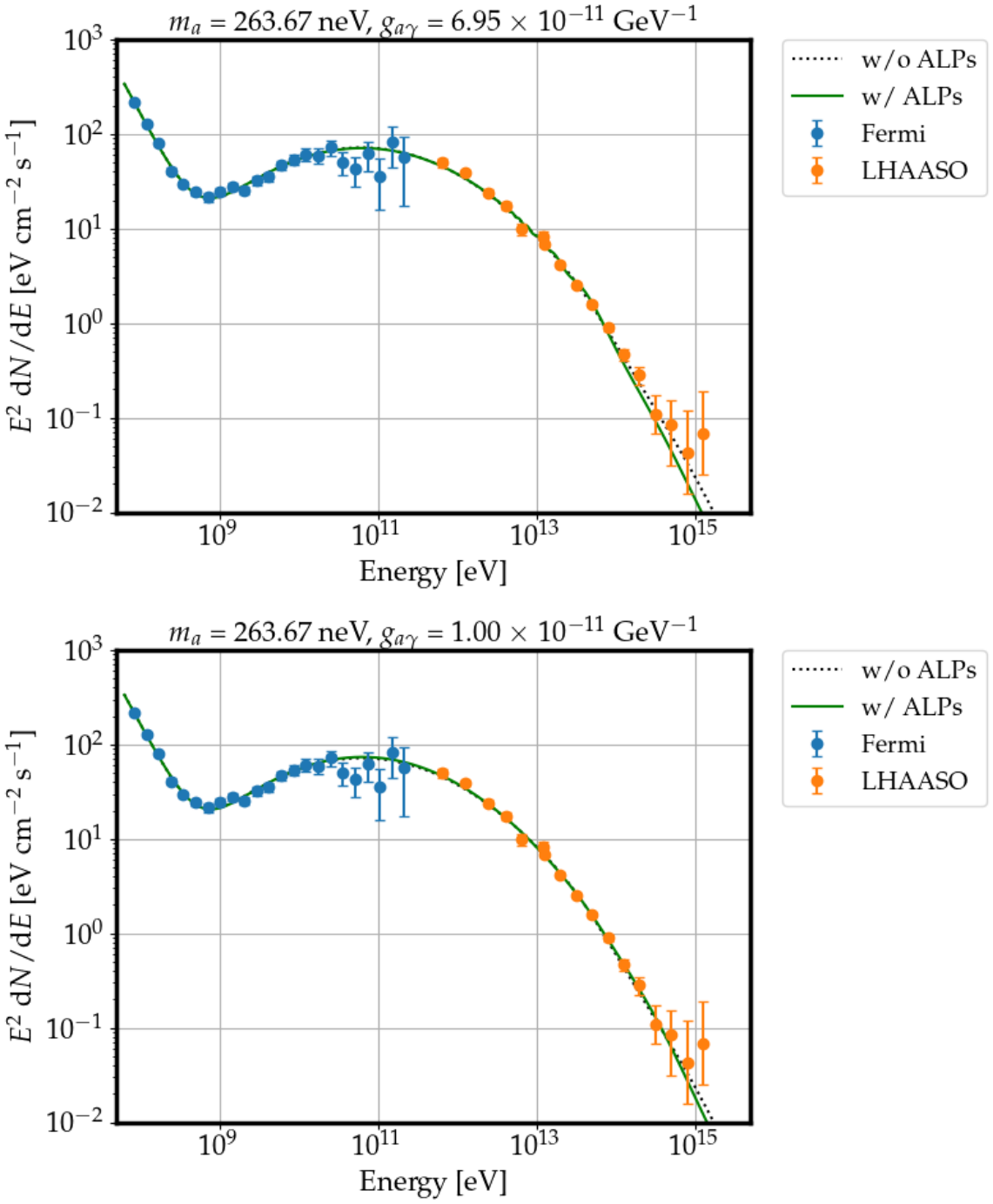

Figure 4.1: Spectral energy distribution without and with axions in some parameter sets. While the parameter set for the top panel is excluded in Fig. 4.3, the bottom one is allowed with decreasing the axion-photon coupling $g_{a\gamma\gamma}$.

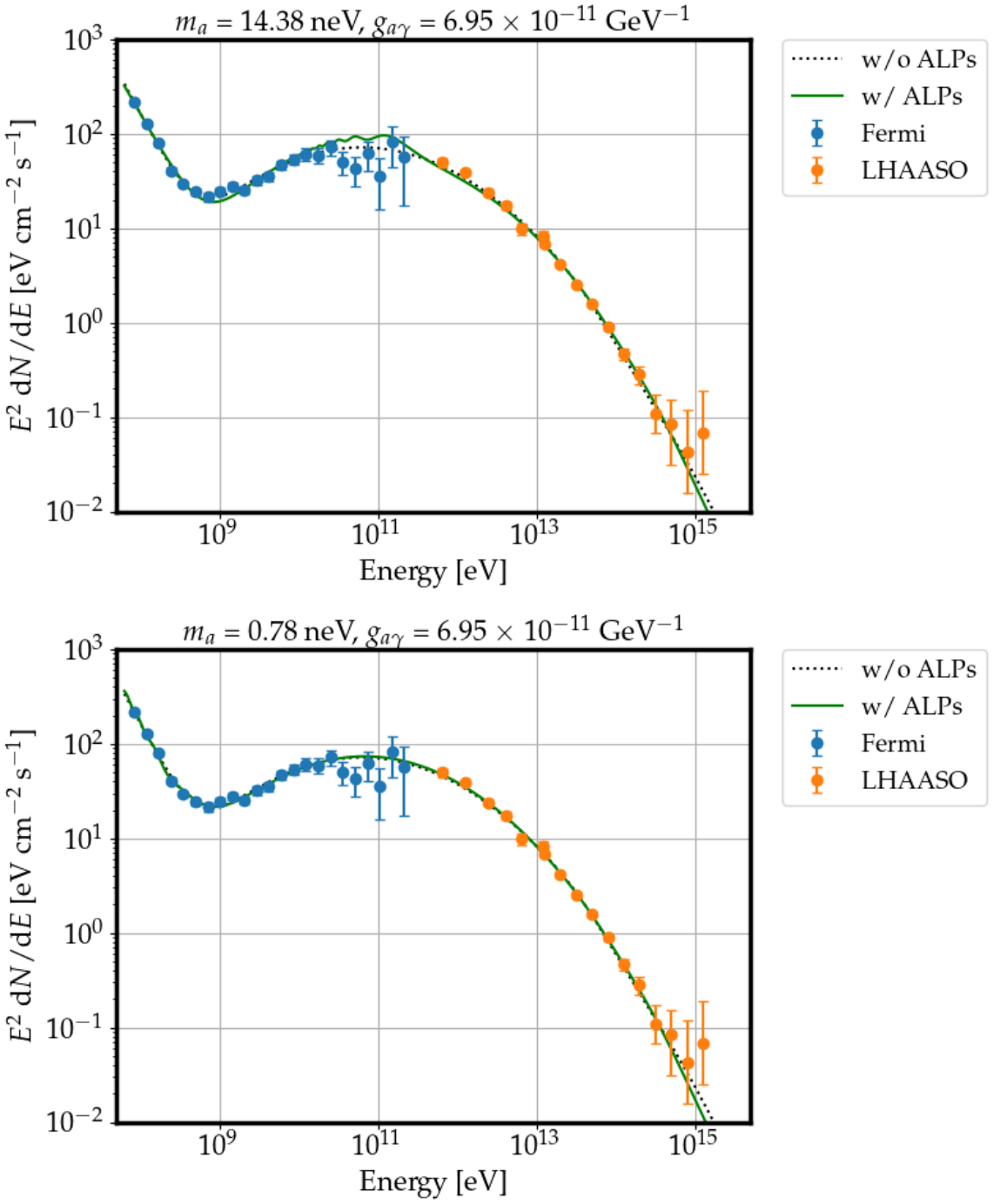

Figure 4.2: Same as Fig. 4.1 but in different parameter sets. The parameter set corresponding to the top panel is excluded in Fig. 4.3. With decreasing the axion mass m_a, the parameter set for the bottom panel is allowed.

4.3 Analysis and Results

We minimize chi-squared function

$$\chi^2 = \sum_i \frac{(\Phi^i_{\rm model} - \Phi^i_{\rm data})^2}{\sigma_i^2} \tag{4.33}$$

to get the best-fit spectrum where $\Phi^i_{\rm model}$, $\Phi^i_{\rm data}$ and σ_i are the predicted flux, the observed one and its error bar, respectively. Each i corresponds to a data point from experiments. The test statistic (TS) are defined as TS $= \chi^2_{\rm w/\,axion} - \chi^2_{\rm w/o\,axion}$. We cannot apply the Wilks' theorem [180] because of non-linear effects on the gamma-ray spectrum in the axion-photon system [132], and should get a TS distribution with Monte Carlo (MC) simulations as performed in [120, 135–137]. 500 mock data sets of the photon flux are randomly produced with Gaussian sampling. Each data point has the mean value and error bar which are set to be the predicted flux based on the best-fit spectrum and the experimental error, respectively. Optimizing the model flux to these mock data sets reproduces the TS distribution under null hypothesis. This distribution is considered to be the approximation of the TS distribution under the axion hypothesis [132] and it turns out to follow a non-central chi-square distribution. Its non-centrality and effective degree of freedom (d.o.f.) are found to be 0.82 and 4.06, respectively. The 95% quantile value is $\Delta{\rm TS}_{95\%} = 11.41$. We can exclude the parameter region where the best-fit chi-square under the axion hypothesis $\hat{\chi}^2_{\rm w/o\,axion}$ exceeds $\hat{\chi}^2_{\rm min} + \Delta{\rm TS}_{95\%}$ at 95% confidence level (C.L.). Here, $\hat{\chi}^2_{\rm min}$ is the global best-fit chi-square for the observational data in the scanned parameter space spanning $m_a \in [10^{-11}, 10^{-5}]\,{\rm eV}$, $g_{a\gamma} \in [10^{-12}, 5\times10^{-10}]\,{\rm GeV}^{-1}$.

Following the statistical analysis described above, we use the observational data of the Crab Nebula with the Fermi-LAT [178] and the LHAASO [156] to get constraints on axion parameters m_a and $g_{a\gamma\gamma}$. In Figs. 4.1 and 4.2, we show these observational datasets and the best-fit spectrum with and without axions in some parameter sets, for instance. Fig. 4.3 represents excluded region (95% C.L.) with high-energy gamma rays from the Crab Nebula as green. CAST has excluded red region [39]. As shown in in Fig. 4.3, the parameter sets for the top panel in Figs. 4.1 and 4.2 are excluded while ones for the bottom panel are allowed with decreasing the axion-photon coupling $g_{a\gamma\gamma}$ in Fig. 4.1 or the axion mass m_a in Fig. 4.2. Taking into account the effects of the magnetic field in the Crab Nebula, the resulting constraint reaches up to $g_{a\gamma\gamma} \lesssim 1\times10^{-11}\,{\rm GeV}^{-1}$ at $m_a \simeq 10^{-8}\,{\rm eV}$, and is exceeding the constraints by CAST in the mass range $10^{-10}\,{\rm eV} \lesssim m_a \lesssim 10^{-6}\,{\rm eV}$. The shown parameter space which is excluded by the Crab Nebula in [144] might be milder than other gamma-ray observations (e.g.

NGC 1275 in the Perseus galaxy cluster [132, 133], Mrk 421 [135–138], quasars [131], and other constraints in [169] and references therein.). However, a reliable constraint on the parameters from observations should be the one derived under the most conservative assumptions. One should avoid obtaining overly stringent constraints under intentionally-strong assumptions. Our constraints arise from the fact that the magnetic-field effect appears twice in the SSC process: once in synchrotron radiation and again in the scattering of that radiation via the inverse Compton process. This aspect was overlooked in the previous works. Consequently, even with the most conservative treatment, we obtained unavoidably more stringent constraints. Then, our limit can be regarded to be newly compliment to those other limits.

We can roughly understand the shape of the excluded region as follows. For sizable conversions from axions to photons, the gamma-ray energy E and propagation distance L should satisfy

$$E \gtrsim E^* = \frac{m_a^2}{2 g_{a\gamma\gamma} B} \tag{4.34}$$

$$L \gtrsim L^* = \frac{2}{g_{a\gamma\gamma} B}. \tag{4.35}$$

E^* and L^* can be written in a suitable unit as [108]

$$E^* \sim \frac{10\,\mathrm{GeV}\, m_{a,\mathrm{neV}}^2}{g_{11} B_{10\,\mu\mathrm{G}}} \tag{4.36}$$

$$L^* \sim \frac{10\,\mathrm{kpc}}{g_{11} B_{10\,\mu\mathrm{G}}} \tag{4.37}$$

with the following notation $m_{a,\mathrm{neV}} \equiv m_a/\mathrm{neV}$, $g_{11} \equiv g_{a\gamma\gamma}/10^{-11}\,\mathrm{GeV}^{-1}$ and $B_{10\,\mu\mathrm{G}} \equiv B/10\,\mu\mathrm{G}$. The region below the green area in Fig. 4.3 is allowed since Eq. (4.35) is not satisfied for galactic sources in the MW, corresponding to the upper bounds $g_{a\gamma\gamma} \lesssim 1 \times 10^{-11}\,\mathrm{GeV}^{-1}$. The right region around $m_{a,\mathrm{neV}} \sim 1000$ is not excluded by the condition Eq. (4.34) meaning that this condition Eq. (4.34) necessitates ultra high-energy gamma rays with energy above PeV scale. We could not conservatively exclude the left region by the following reason. E^* becomes smaller than 1 GeV in the parameter space $m_{a,\mathrm{neV}} \lesssim 0.1$ and $1 \lesssim g_{11} \lesssim 50$ and then the axion-photon conversion is efficient for the energy range observed by Fermi-LAT [178] and LHAASO [156]. However, this effect is compensated by the parameters for the intrinsic spectrum and we cannot distinguish the case with and without axions. These imply that, roughly speaking, the observed gamma-ray energy correspond to the mass range excluded in this analysis ($0.1 \lesssim m_{a,\mathrm{neV}} \lesssim 1000$).

Here, let us put a comment on statistical analyses. We did not use so-called CL_s method, which was used in axion searches with gamma-ray observations (e.g. [120, 134, 138, 143]) as well as high-energy experiments [181–183]. It is known that this method allows us to get less optimistic constraints on considered parameters than the traditional frequentist approach when it is difficult to distinguish the null and alternative hypothesis with experiments. However, CL_s method requires high computational resources because one needs to optimize the model flux with mock data sets for each point in the broad parameter space. [120] compared the CL_s method with the one used in [132, 135–137], and the authors concluded that the latter is also consistent with the former. This is why we took the latter approach to reduce time for numerical calculations.

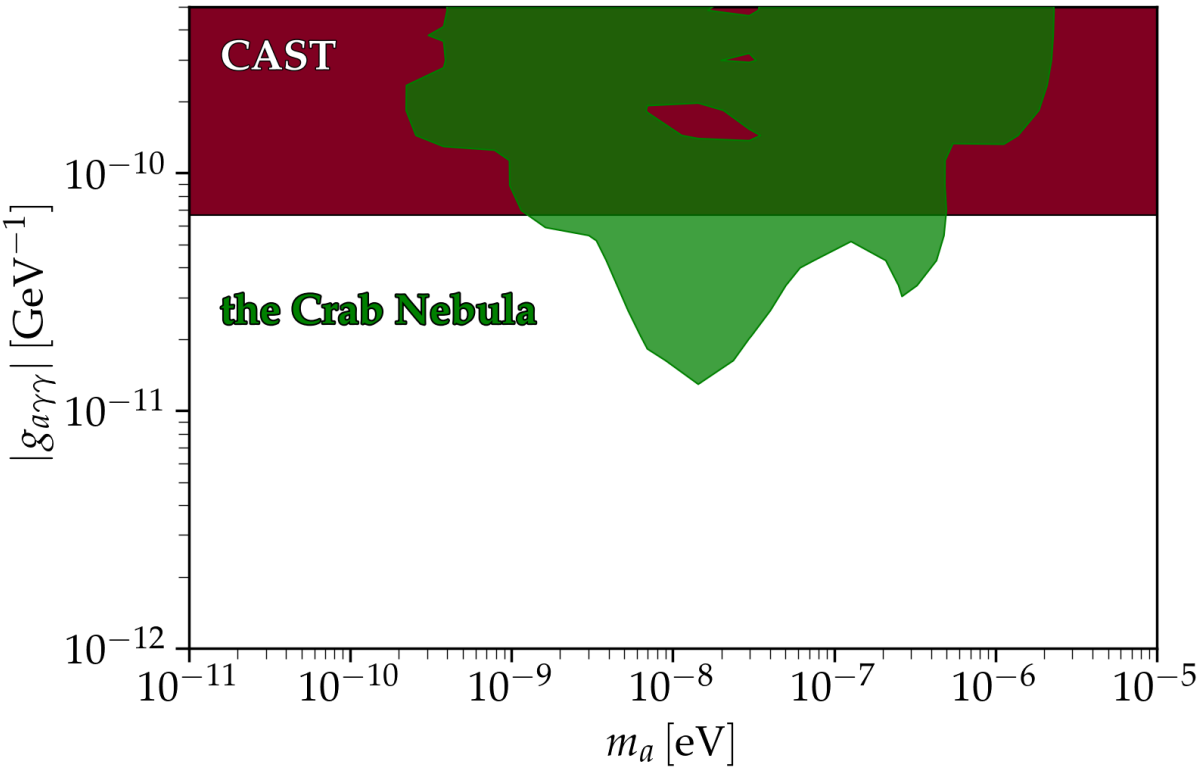

Figure 4.3: Excluded region at 95% C.L. is shown as green based on the observations of gamma rays from the Crab Nebula. Red region is excluded by the CAST experiment [39]. This figure is produced with `AxionLimits` [169].

4.4 Summary

In Chapter 4, we have investigated the importance of the magnetic fields in the Crab Nebula for the axion search with gamma rays. The axion-photon beams experience the gamma-ray absorption and the axion-photon conversion in their journey from the source. For the model of magnetic fields around the Crab Nebula, we considered the variable B-field model [159]. It turned out that the magnetic fields in the Crab Nebula affected on how the gamma-ray spectrum is distorted by the axion-photon conversion (Figs. 4.1 and 4.2). This effect has not been taken into account in axion searches with gamma rays from the Crab Nebula before. By considering the magnetic fields of the Crab Nebula, we obtain new constraints reaching down to $g_{a\gamma\gamma} \lesssim 1 \times 10^{-11}\,\mathrm{GeV}^{-1}$ at $m_a \simeq 10^{-8}\,\mathrm{eV}$ and exceeding the constraints by CAST in the axion mass range $10^{-10}\,\mathrm{eV} \lesssim m_a \lesssim 10^{-6}\,\mathrm{eV}$. This consideration can be applicable to other galactic sources. The analysis in this paper will be a step forward to more precise constraints on the axion parameters as briefly mentioned below.

Let us give a comment on the statistical analysis and other model uncertainties. As explained in Section 4.3, we have not used the $\mathrm{CL_s}$ method for saving times for numerical calculations. Although it was shown in [120] that the statistical analysis used in [132, 135–137] and this paper gave consistent results compared to the $\mathrm{CL_s}$ method. However, we may have a possibility to obtain more conservative results based on the $\mathrm{CL_s}$ method after increasing computer resources. We have also a comment on model uncertainties of the Crab Nebula. Although the Crab Nebula has been observed for long time and in broad energy range allowing for developing SSC emission models, there still is a little room for adding other contributions to the spectrum of the Crab Nebula. For example, [184] considered a hadronic contribution such as neutral pion decay in addition to the leptonic component in order to fit the gamma-ray spectrum with LHAASO data [156] at PeV scale. If we take this possibility into account, we could extend our analysis performed in this paper. These remain as future works.

Chapter 5

Conclusion

In this thesis, we discussed the axion search with the gamma-ray observations of the Crab Nebula. In Chapter 2, we have first reviewed the observational evidences of dark matter at several scales and then summarized the general properties which dark matter candidates should have. Although dark matter is account for 26% energy of the Universe, we have not known what it really is. Several dark matter candidates have been discussed for a long time, including the WIMPs, the PBHs and the axions. They have been investigated in cosmology, astrophysics, and particle physics. Especially, the QCD axion is a dark matter candidate motivated as a solution to the so-called strong CP problem. ALPs are a kind of its generalization. The ALP mass m_a and coupling $g_{a\gamma\gamma}$ have no relation as opposed to the QCD axion. Models beyond the SM often predict the existence of the ALPs. The axions have been explored in several ways. Photons are one of the important probes and have the interaction with axions as $g_{a\gamma\gamma}a\boldsymbol{E}\cdot\boldsymbol{B}$ where a is the axion field, $\boldsymbol{E}$ is the electric field, and $\boldsymbol{B}$ is the magnetic field. This motivated us to search axions with magnetic field in the laboratory and in the Universe.

For example, the helioscopes are trying to detect solar axions produced by the Primakoff process by imposing magnetic fields in laboratories [39]. The haloscopes are searching axion dark matter with cavities [50]. The light shining through a wall experiments are on-going although their constraints are generically weaker than those by the helioscopes and the haloscopes. Observations of celestial objects are also one of ways to search axions, as discussed in Chapter 3. If there exist axions in the Universe, gamma-ray spectra can be distorted through the axion-photon conversion under magnetic fields in the Universe. Astrophysical sources have magnetic fields stronger than ones on the ground and are distant from the Earth, meaning that we naively expect relatively strong signatures from their observations. Actually, astrophysics have given us stronger constraints for lighter axions

than the helioscopes. For example, we have seen that gamma rays from extragalactic sources can indicate axion-induced signals in their spectra which gave us the constraints exceeding ones by the CAST [39] in some axion mass range. However, we should carefully take into account uncertainties arising from modeling of sources in astrophysics. Otherwise, such uncertainties can change significantly resulting constraints and make these results too optimistic or unreliable.

Axions have also been explored with gamma rays emitted by galactic sources such as SNRs and PWNe. For example, the Crab Nebula was used to constrain axions but an important piece was missing in references: the magnetic field in the Crab Nebula. In Chapter 4, we considered the effects of models for magnetic fields in the Crab Nebula on axion search, and investigated possibilities that modeling of the magnetic fields should be cared [144]. In reference (e.g. [159]), models of electromagnetic wave's emission have been developed for the Crab Nebula thanks to observational data sets from radio to gamma rays. The emission can be explained well using SSC emission model where synchrotron photons are radiated under magnetic fields of the Crab Nebula and kicked up by high-energy electrons in the Crab Nebula. We considered the model of the variable magnetic field around the Crab Nebula. The magnetic fields are important not only for the SSC process but also the axion-photon conversion when axion-photon beams propagate through the Universe. This effect has not been taken into account in axion searches with gamma rays from the Crab Nebula so far. By considering the magnetic fields of the Crab Nebula, we obtain new constraints reaching down to $g_{a\gamma\gamma} \lesssim 1 \times 10^{-11}\,\mathrm{GeV}^{-1}$ at $m_a \simeq 10^{-8}\,\mathrm{eV}$ and exceeding the constraints by CAST in the axion mass range $10^{-10}\,\mathrm{eV} \lesssim m_a \lesssim 10^{-6}\,\mathrm{eV}$. This consideration can be applicable to other galactic sources. The analysis in this thesis will be a step forward to more precise constraints on axions with gamma rays.

Acknowledgement

I would like to express my deepest gratitude to my supervisor, Kazunori Kohri, for his continuous guidance, invaluable advice, and support throughout my doctoral studies. His insights and encouragement have shaped my research and helped me grow as a researcher. I would not be here today without his constant guidance and thoughtful support. I am also sincerely grateful to the members of my thesis committee — Kaori Fuyuto, Yuko Urakawa, Motoi Endo, and Takahiko Matsubara — for their constructive feedback and many helpful discussions. Their comments have greatly improved the quality of this thesis.

My sincere appreciation goes to the members of the Cosmophysics and Phenomenology Group, including but not limited to Masashi Aiko, Kazuyuki Akitsu, Yuma Furuta, Yu Hamada, Minxi He, Yingqiu He, Asuka Ito, Ryuichiro Kitano, Mikage Kobayashi, Tadashi Kuramoto, Houheng Leong, Kyohei Mukaida, Yushi Mura, Wakutaka Nakano, Mihoko Nojiri, Shin'ichi Nojiri, Ippei Obata, Shohei Okawa, Pankaj Saha, Yutaka Sakamura, Daisuke Shimozuru, Toya Suzuki, Ryoto Takai, Lukas Treuer, Tenta Tsuji, Fumio Uchida, and Hidenaga Watanabe. Discussions with them broadened and deepened my understanding of physics.

I would also like to thank all the members of the KEK Theory Center, especially Akinobu Dote, Shirabe Endo, Shoji Hashimoto, Yoshimasa Hidaka, Kieko Iioka, Keiya Ishiguro, Satoshi Iso, Takashi Kaneko, Ryan Kellermann, Rinto Kuramochi, Jinyang Li, Takato Mori, Tomoko Numata, Sota Nakajima, Tomoya Nishiki, Jun Nishimura, Maki Ohishi, Yuko Ohno, Takumi Oikawa, Worapat Piensuk, Katsuta Sakai, Cheng-Tsung Wang, Norikazu Yamada, Naoyuki Yamamori, and Ryo Yokokura. Their existences have directly and indirectly motivated, encouraged and supported my Ph.D. life.

Last but not least, I would like to express my heartfelt gratitude to my father, who continues to encourage me despite being bedridden due to a stroke, and to my family, who have stood by me and overcome many difficulties together during my Ph.D. journey.

Appendix A

Symbols, Acronyms and Conventions

A.1 Symbols

Symbols used in this thesis are listed in Table A.1.

speed of light c	$2.99792458 \times 10^{10}\,\mathrm{cm\,s^{-1}}$
Planck's constant $\hbar$	$1.0546 \times 10^{-27}\,\mathrm{cm^2\,g^{-1}\,s^{-1}}$
Newton's constant G	$6.673 \times 10^{-8}\,\mathrm{cm^3\,g^{-1}\,s^{-2}}$
Electron mass m_e	$511\,\mathrm{keV}$
Solar mass $M_\odot$	$1.989 \times 10^{33}\mathrm{g}$
Thomson cross section σ_T	$6.6524 \times 10^{-25}\,\mathrm{cm^2}$

Table A.1: Physical constants.

A.2 Acronyms

The following acronyms are used in this thesis.

AGN	Active galactic nucleus (*source type*)
ALP	Axion-like particle (*dark matter candidate*)
CAST	CERN axion solar telescope (*instrument*)
CMB	Cosmic microwave backgrounds
EBL	Extragalactic background light
Fermi-LAT	Fermi large area telescope (*instrument*)
FSRQ	Flat-spectrum radio quasar (*source type*)
H.E.S.S.	High Energy Stereoscopic System (*instrument*)
LHAASO	Large high altitude air shower observatory (*instrument*)
PBH	Primordial black hole (*dark matter candidate*)
PWN	Pulsar wind nebula (*source type*)
MAGIC	Major atmospheric gamma imaging Cherenkov telescopes (*instrument*)
MW	the Milky Way
QCD	Quantum chromodynamics
SN	Supernova (*source type*)
SNR	Supernova remnant (*source type*)
SSC	Synchrotron self-Compton
VERITAS	Very energetic radiation imaging telescope array system (*instrument*)
WIMP	Weakly interacting massive particle (*dark matter candidate*)

Table A.2: Acronyms used in this thesis.

A.3 Conventions

• Minkowski metric

$$g^{\mu\nu} = \mathrm{diag}(+1, -1, -1, -1) \tag{A.1}$$

• Pauli matrices

$$\sigma^1 = \begin{pmatrix} 0 & 1 \\ 1 & 0 \end{pmatrix}, \quad \sigma^2 = \begin{pmatrix} 0 & -i \\ i & 0 \end{pmatrix}, \quad \sigma^3 = \begin{pmatrix} 1 & 0 \\ 0 & -1 \end{pmatrix}. \tag{A.2}$$

• Gamma matrices

$$\gamma^\mu = \begin{pmatrix} 0 & \sigma^\mu \\ \bar{\sigma}^\mu & 0 \end{pmatrix}, \qquad \gamma^5 = i\gamma^0\gamma^1\gamma^2\gamma^3 = \begin{pmatrix} -I_2 & 0 \\ 0 & I_2 \end{pmatrix} \tag{A.3}$$

with $\sigma^\mu = (1, \sigma^i)$, $\bar{\sigma}^\mu = (1, -\sigma^i)$ $(i = 1, 2, 3)$, and I_2 is 2×2 unit matrix. Also, the gamma matrices satisfy the following relations:

$$\{\gamma^\mu, \gamma^\nu\} = 2g^{\mu\nu}, \quad \{\gamma^\mu, \gamma^5\} = 0, \quad (\gamma^5)^2 = I_4 \tag{A.4}$$

$$\begin{aligned} &(\gamma^0)^T = \gamma^0, \quad (\gamma^1)^T = -\gamma^1, \quad (\gamma^2)^T = \gamma^2, \quad (\gamma^3)^T = -\gamma^3, \\ &(\gamma^0)^* = \gamma^0, \quad (\gamma^1)^* = \gamma^1, \quad (\gamma^2)^* = -\gamma^2, \quad (\gamma^3)^* = \gamma^3, \\ &(\gamma^0)^\dagger = \gamma^0, \quad (\gamma^1)^\dagger = -\gamma^1, \quad (\gamma^2)^\dagger = -\gamma^2, \quad (\gamma^3)^\dagger = -\gamma^3. \end{aligned} \tag{A.5}$$

Here, I_4 is 4×4 unit matrix, and $T, *, \dagger$ represent transfer, complex conjugate and Hermitian conjugate, respectively.

• chiral projection operators

$$P_L = \frac{I_4 - \gamma^5}{2} = \begin{pmatrix} I_2 & \mathbf{0} \\ \mathbf{0} & \mathbf{0} \end{pmatrix}, \quad P_R = \frac{I_4 + \gamma^5}{2} = \begin{pmatrix} \mathbf{0} & \mathbf{0} \\ \mathbf{0} & I_2 \end{pmatrix}. \tag{A.6}$$

The chiral projection operators and the gamma matrices satisfy

$$\gamma^\mu P_L = P_R \gamma^\mu, \quad \gamma^\mu P_R = P_L \gamma^\mu, \tag{A.7}$$

$$\gamma^5 P_L = -P_L, \quad \gamma^5 P_R = P_R. \tag{A.8}$$

Appendix B

The Standard Model

In this chapter, we briefly review the standard model (SM) $SU(3)_C \times SU(2)_L \times U(1)_Y$ describing strong, weak and electromagnetic interactions. In Appendix B.1, we introduce gauge fields, fermions and a Higgs field in the SM.

B.1 Particles in the standard model

$\mathcal{L}_{\text{gauge}}$ is Lagrangian for gauge fields

$$\mathcal{L}_{\text{gauge}} = -\frac{1}{4}G^{a\,\mu\nu}G^{a}_{\mu\nu} - \frac{1}{4}W^{b\,\mu\nu}W^{b}_{\mu\nu} - \frac{1}{4}B^{\mu\nu}B_{\mu\nu} \tag{B.1}$$

where

$$\begin{aligned} G^{a}_{\mu\nu} &= \partial_\mu G^{a}_{\nu} - \partial_\nu G^{a}_{\mu} + g_3 f^{abc} G^{b}_{\mu} G^{c}_{\nu}, \\ W^{a}_{\mu\nu} &= \partial_\mu W^{a}_{\nu} - \partial_\nu W^{a}_{\mu} + g_2 f^{abc} W^{b}_{\mu} W^{c}_{\nu}, \\ B_{\mu\nu} &= \partial_\mu B_{\nu} - \partial_\nu B_{\mu}. \end{aligned} \tag{B.2}$$

Here, G^{a}_{μ}, W^{a}_{μ}, B_μ are the gauge fields associated with $SU(3)_C$, $SU(2)_L$, $U(1)_Y$ gauge symmetries, respectively. g_3 and g_2 are the gauge coupling constants for $SU(3)_C$ and $SU(2)_L$, respectively.

The SM fermions consist of quarks ($SU(3)_C$ fundamental representations) and leptons ($SU(3)_C$ trivial representations). Using chiral projection operators $P_{L,R}$,

$$\begin{cases} \psi_L = P_L \psi \\ \psi_R = P_R \psi \end{cases} \tag{B.3}$$

we can project a fermion ψ into ψ_L and ψ_R which are eigen states of $\gamma^5 = i\gamma^0\gamma^1\gamma^2\gamma^3$.

$\overline{\psi} = \psi^\dagger \gamma^0$ is the Dirac conjugate

$$\begin{cases} \overline{\psi_R} \equiv (\psi_R)^\dagger \gamma^0 = \left(\dfrac{I_4 + \gamma^5}{2} \psi \right)^\dagger \gamma^0 = \psi^\dagger P_R \gamma^0 = \overline{\psi} P_L \\ \overline{\psi_L} \equiv (\psi_L)^\dagger \gamma^0 = \left(\dfrac{I_4 - \gamma^5}{2} \psi \right)^\dagger \gamma^0 = \psi^\dagger P_L \gamma^0 = \overline{\psi} P_R \end{cases} \tag{B.4}$$

where I_4 is 4×4 unit matrix.

The quarks can be decomposed into up-type and down-type quarks. Left-handed up-type quarks u_L and down-type quarks d_L consist of quark doublets q_L

$$q_L = \begin{pmatrix} u_L \\ d_L \end{pmatrix} = P_L \begin{pmatrix} u \\ d \end{pmatrix} \tag{B.5}$$

transforming as **2** representation under $SU(2)_L$. Right-handed up-type quarks u_R and down-type quarks d_R transform as trivial representations. $U(1)_Y$ charges of the quark doublets, right-handed up-type quarks and down-type quarks are $1/6$, $2/3$ and $-1/3$, respectively. A kinetic term for the quarks $\mathcal{L}_{\text{quark}}$ is given by

$$\mathcal{L}_{\text{quark}} = \overline{q_L} \not{D} q_L + \overline{u_R} \not{D} u_R + \overline{d_R} \not{D} d_R \tag{B.6}$$

where $\not{D}$ is the contraction of the gamma matrices γ^μ with covariant derivatives D_μ which is expressed as

$$\begin{aligned} D_\mu q_L &= \left[\partial_\mu + i g_3 G_\mu + i g_2 W_\mu + i g_1 \left(\frac{1}{6} \right) B_\mu \right] q_L, \\ D_\mu u_R &= \left[\partial_\mu + i g_3 G_\mu + i g_1 \left(\frac{2}{3} \right) B_\mu \right] u_R, \\ D_\mu d_R &= \left[\partial_\mu + i g_3 G_\mu + i g_1 \left(-\frac{1}{3} \right) B_\mu \right] d_R \end{aligned} \tag{B.7}$$

with the $U(1)_Y$ gauge coupling constant g_1.

The leptons can be classified into neutrinos and charged leptons. Left-handed neutrinos ν_L and charged leptons e_L are components of lepton doublets l_L

$$l_L = \begin{pmatrix} \nu_L \\ e_L \end{pmatrix} = P_L \begin{pmatrix} \nu \\ e \end{pmatrix} \tag{B.8}$$

which transform as $SU(2)_L$ fundamental representations. Right-handed charged leptons e_R correspond to trivial representations under $SU(2)_L$. $U(1)_Y$ charges of the lepton doublets and right-handed charged leptons are $-\frac{1}{2}$ and -1, respectively. The kinetic term for

quarks	$(r_1, r_2)_a$	leptons	$(r_1, r_2)_a$
$q_L = \begin{pmatrix} u_L \\ d_L \end{pmatrix}$	$(3, 2)_{1/6}$	$l_L = \begin{pmatrix} \nu_L \\ e_L \end{pmatrix}$	$(1, 2)_{1/2}$
u_R	$(3, 1)_{2/3}$	(ν_R)	$(1, 1)_0$
d_R	$(3, 1)_{-1/3}$	e_R	$(1, 1)_{-1}$

Figure B.1: Representations of the SM quarks and leptons under $SU(3)_C \times SU(2)_L \times U(1)_Y$. In $(r_1, r_2)_a$, r_1 and r_2 means the representations for $SU(3)_C$ and $SU(2)_L$, respectively. a is the $U(1)_Y$ charge.

leptons $\mathcal{L}_{\text{lepton}}$ is given by

$$\mathcal{L}_{\text{lepton}} = \overline{l_L} \not{D} l_L + \overline{e_R} \not{D} e_R \tag{B.9}$$

where their covariant derivatives are

$$\begin{aligned} D_\mu l_L &= \left\{ \partial_\mu + i g_2 W_\mu + i g_1 \left(-\frac{1}{2} \right) B_\mu \right\} l_L, \\ D_\mu e_R &= \left\{ \partial_\mu + i g_1 \left(-1 \right) B_\mu \right\} d_R \end{aligned} \tag{B.10}$$

Fig. B.1 shows the representations of the SM quarks and leptons.

There exist three-type quarks and leptons with same representations but different masses, called "generation" in the SM. For example, the SM includes up, charm and top quarks as the up-type quarks.

Higgs field $H = (\phi^+, \phi^0)^T$ is a complex and two-component scalar. It transforms as a trivial representation under $SU(3)_C$ and a fundamental representation **2** under $SU(2)_L$, and has $1/2$ $U(1)_Y$ charge. A kinetic and potential terms for the Higgs field $\mathcal{L}_{\text{Higgs}}$ are given by

$$\mathcal{L}_{\text{Higgs}} = |D_\mu H|^2 - m^2 |H|^2 - \lambda |H|^4 \tag{B.11}$$

where the covariant derivative $D_\mu H$ is

$$D_\mu H = \left\{ \partial_\mu + i g_2 W_\mu + i g_1 \left(\frac{1}{2} \right) B_\mu \right\} H \tag{B.12}$$

with the Higgs potential $V(H) = m^2 |H|^2 + \lambda |H|^4$. Yukawa interaction between the Higgs field and the SM fermions $\mathcal{L}_{\text{Yukawa}}$ is described as

$$\mathcal{L}_{\text{Yukawa}} = - \sum_{i,j=1}^{3} \left[y^u_{ij} \overline{q_{iL}} \tilde{H} u_{jR} + y^d_{ij} \overline{q_{iL}} H d_{jR} + y^e_{ij} \overline{l_{iL}} H e_{jR} + \text{h.c.} \right] \tag{B.13}$$

where $\tilde{H} \equiv i\sigma^2 H^*$ transform as a $SU(2)_L$ doublet as H. y_{ij} are the Yukawa couplings and the indices $i, j = 1, 2, 3$ denote generations. The Yukawa-interactions become mass terms for the quarks and leptons after the Higgs field get a vacuum expectation value (VEV).

Appendix C

Axion-Photon Conversion

In Chapter C, we first derive modified Maxwell's equations with axions which allow for calculating axion-photon conversion probability in a homogeneous magnetic field.

C.1 Conversion in a homogeneous magnetic field

We consider in this thesis axion-photon system described by the following Lagrangian

$$\mathcal{L} = -\frac{1}{4}F_{\mu\nu}F^{\mu\nu} + \frac{1}{2}\,\partial_\mu a\,\partial^\mu a - \frac{1}{2}m_a^2 a^2 - \frac{1}{4}g_{a\gamma\gamma}aF_{\mu\nu}\tilde{F}^{\mu\nu} \tag{C.1}$$

where a is the axion field, m_a is its mass, $g_{a\gamma\gamma}$ is the axion-photon coupling. $F_{\mu\nu} = \partial_\mu A_\nu - \partial_\nu A_\mu$ is the field strength tensor for photons A_μ, and $\tilde{F}^{\mu\nu}$ is its dual. The first term describes the kinetic term for photons, corresponding to ordinary the Maxwell's equations. The second and the third term are the kinetic and mass terms for axions, respectively. The last term is responsible for mixing between axions and photons.

We calculate the conversion probability between axions and photons, starting with solving the Euler-Lagrange equation for the axion field a

$$\frac{\partial\mathcal{L}}{\partial a} = -\frac{1}{4}g_{a\gamma\gamma}F_{\mu\nu}\tilde{F}^{\mu\nu} - m_a^2 a, \tag{C.2}$$

$$\frac{\partial\mathcal{L}}{\partial(\partial_\mu a)} = -\,\partial_\mu a. \tag{C.3}$$

This leads to an inhomogeneuous Klein-Gordon equation for the axion field a

$$(\Box + m_a^2)a = -g_{a\gamma\gamma}\boldsymbol{E}\cdot\boldsymbol{B} \tag{C.4}$$

where $\boldsymbol{E}$ is the electric field, $\boldsymbol{B}$ is the magnetic field, and we used the fact that the last term in Eq. (C.1) can be written in terms of $\boldsymbol{E}$ and $\boldsymbol{B}$. We consider a propagation of axion-photon beams in x_3-direction under a homogeneous and static magnetic field $\boldsymbol{B}_0 = (B_0, 0, 0)^T$. The propagating wave can be seen as a perturbation of the background magnetic fields:

$$\begin{aligned} a(x_3, t) &= \delta a(x_3, t), \\ \boldsymbol{B}(x_3, t) &= \boldsymbol{B}_0 + \delta\boldsymbol{B}(x_3, t), \\ \boldsymbol{E}(x_3, t) &= \delta\boldsymbol{E}(x_3, t). \end{aligned} \tag{C.5}$$

We can describe dynamics of the axion field perturbation as

$$(\Box + m_a^2)\delta a = -g_{a\gamma\gamma}\delta\boldsymbol{E} \cdot (\boldsymbol{B}_0 + \delta\boldsymbol{B}) \tag{C.6}$$

$$= -g_{a\gamma\gamma}\boldsymbol{B}_0 \cdot \delta\boldsymbol{E} \tag{C.7}$$

where we have dropped terms quadratic and higher in the perturbations. By substituting the electric field $\boldsymbol{E} = -\nabla\phi - \partial_t\boldsymbol{A}$ and magnetic field $\boldsymbol{B} = \nabla \times \boldsymbol{A}$ in terms of electric potential ϕ and vector potential $\boldsymbol{A}$, we obtain

$$\begin{aligned} (\Box + m_a^2)\delta a &= g_{a\gamma\gamma}\boldsymbol{B}_0 \cdot \partial_t\delta\boldsymbol{A} \\ &= g_{a\gamma\gamma}B_0\,\partial_t\delta A_\parallel \end{aligned} \tag{C.8}$$

in Weyl gauge ($\delta A^0 = \delta\phi = 0$, $\nabla \cdot \delta\boldsymbol{A} = 0$). The modified Maxwell's equation lead to

$$0 = g_{a\gamma\gamma}(\nabla\delta a) \cdot \boldsymbol{B}_0, \tag{C.9}$$

after dropping terms quadratic in the perturbations, and it is obvious because δa only depends on x_3. We can also obtain

$$\Box\delta\boldsymbol{A} = g_{a\gamma\gamma}(\partial_t\delta a)\boldsymbol{B}_0 \tag{C.10}$$

which can be decomposed as

$$\Box\delta A_\parallel = g_{a\gamma\gamma}(\partial_t\delta a)\boldsymbol{B}_0, \tag{C.11}$$

$$\Box\delta A_\perp = 0. \tag{C.12}$$

Eq. (C.12) implies that $\delta A_\perp$ decouples and does not mix with the axion field.

Under the plane-wave ansatz where $\delta a(x_3, t) = e^{i\omega(x_3 - t)}a(x_3)$, $\delta A_\parallel(x_3, t) = e^{i\omega(x_3 - t)}A_\parallel$,

spatial double derivative with respect to $x_3(= z)$ becomes

$$\begin{aligned}\partial_z^2 \delta a(x_3, t) &= \partial_z^2 e^{i\omega(x_3 - t)} a(x_3) \\ &= \partial_z \left[i\omega e^{i\omega(x_3-t)} + e^{i\omega(x_3-t)}\, \partial_3 a(x_3) \right] \\ &= e^{i\omega(x_3-t)} \left[-\omega^2 + 2i\omega\, \partial_z + \partial_z^2 \right] a(x_3) \\ &\simeq e^{i\omega(x_3-t)} \left[-\omega^2 + 2i\omega\, \partial_z \right] a(x_3) \end{aligned} \tag{C.13}$$

Then, the equation for axions Eq. (C.8) is linearized as

$$i \frac{\mathrm{d}a(x_3)}{\mathrm{d}x_3} = \frac{m_a^2}{2\omega} a(x_3) - \frac{1}{2} B_0 A_\parallel(x_3). \tag{C.14}$$

Eq. (C.11) can be similarly linearized

$$i \frac{\mathrm{d}A_\parallel(x_3)}{\mathrm{d}x_3} = -\frac{1}{2} g_{a\gamma\gamma} B_0 a(x_3). \tag{C.15}$$

Eq. (C.14) and Eq. (C.15) are coupled as a Schrödinger-like equation

$$\left(i \frac{\mathrm{d}}{\mathrm{d}x_3} + \mathcal{M} \right) \Psi(x_3) = 0 \tag{C.16}$$

with $\Psi(x_3) = (A_\parallel(x_3),\, a(x_3))^T$ and the mixing matrix

$$\mathcal{M} = \begin{pmatrix} 0 & \Delta_{a\gamma} \\ \Delta_{a\gamma} & \Delta_a \end{pmatrix} \tag{C.17}$$

whose components are $\Delta_a = -m_a^2/(2\omega)$ and $\Delta_{a\gamma} = g_{a\gamma\gamma} B_0/2$.

The solution of Eq. (C.16) is given by

$$a(x_3) = (\cos^2\theta e^{-i\lambda_+ x_3} + \sin^2\theta e^{-i\lambda_- x_3}) a(0) + \cos\theta \sin\theta (e^{-i\lambda_+ x_3} - e^{-i\lambda_- x_3}) A_\parallel(0), \tag{C.18}$$

$$A(x_3) = \cos\theta \sin\theta (e^{-i\lambda_+ x_3} - e^{-i\lambda_- x_3}) a(0) + (\cos^2\theta e^{-i\lambda_+ x_3} + \sin^2\theta\, e^{-i\lambda_- x_3}) A_\parallel(0) \tag{C.19}$$

where $\lambda_\pm = (\Delta_a \pm \sqrt{\Delta_a^2 + (2\Delta_{a\gamma})^2})/2$ (the signs correspond) are eigenvalues of the mixing matrix $\mathcal{M}$ which is diagonalized by an orthogonal matrix

$$\mathcal{O} = \begin{pmatrix} \cos\theta & -\sin\theta \\ \sin\theta & \cos\theta \end{pmatrix}. \tag{C.20}$$

Considering an initial state $\Psi(0) = (A_\parallel(0), a(0)) = (1, 0)$ propagating for a distance L, for instance, a probability for photons converted into axions $P_{\gamma\to a}$ is given by

$$\begin{aligned} P_{\gamma\to a}(L) &= \cos^2\theta \sin^2\theta |e^{-i\lambda_+ L} - e^{-i\lambda_- L}|^2 \\ &= 2\cos^2\theta\sin^2\theta(1 - \cos[(\lambda_+ - \lambda_-)L]) \\ &= \sin^2 2\theta \sin^2[(\lambda_+ - \lambda_-)L] \\ &= \left(\frac{g_{a\gamma\gamma}B_0 L}{2}\right)^2 \frac{\sin^2(\Delta_{\rm osc}L/2)}{(\Delta_{\rm osc}L/2)^2} \end{aligned} \tag{C.21}$$

with $\Delta_{\rm osc} = \sqrt{\Delta_a^2 + (2\Delta_{a\gamma})^2} = 2\Delta_{a\gamma}\sqrt{1 + (E_{\rm cr}/E)^2}$. Here, $E_{\rm cr}$ is a critical energy

$$E_{\rm cr} = E\frac{|\Delta_a - \Delta_{\rm pl}|}{2\Delta_{a\gamma}} \tag{C.22}$$

$$\simeq 2.5\times 10^7 \frac{|m_a^2 - \omega_{\rm pl}^2|}{(10^{-10}\,{\rm eV})^2}\left(\frac{\mu{\rm G}}{B_0}\right)\left(\frac{10^{-11}\,{\rm GeV}^{-1}}{g_{a\gamma\gamma}}\right){\rm eV} \tag{C.23}$$

In high-energy limit $E \gg E_{\rm cr}$, the oscillation wavenumber becomes $\Delta_{\rm osc} \simeq 2\Delta_{a\gamma}$ and this makes the axion-photon conversion maximally efficient and energy-independent. This energy range is called strong-mixing regime. The conversion probability is further simplified as $P_{\gamma\to a} = \left(\frac{g_{a\gamma\gamma}B_0 L}{2}\right)^2$ when $\Delta_{\rm osc}L \ll 1$. Although actual magnetic field environments are more complicated and the conversion probability is numerically calculated, Eq. (C.21) is still useful to briefly understand behavior of the axion-photon conversion.

References

[1] F. Zwicky. "On the Masses of Nebulae and of Clusters of Nebulae". In: *Astrophys. J.* 86 (1937), pp. 217–246. DOI: 10.1086/143864.

[2] Benjamin R. Safdi. "TASI Lectures on the Particle Physics and Astrophysics of Dark Matter". In: *PoS* TASI2022 (2024), p. 009. DOI: 10.22323/1.439.0009. arXiv: 2303.02169 [hep-ph].

[3] R. D. Peccei and Helen R. Quinn. "CP Conservation in the Presence of Instantons". In: *Phys. Rev. Lett.* 38 (1977), pp. 1440–1443. DOI: 10.1103/PhysRevLett.38.1440.

[4] R. D. Peccei and Helen R. Quinn. "Constraints Imposed by CP Conservation in the Presence of Instantons". In: *Phys. Rev. D* 16 (1977), pp. 1791–1797. DOI: 10.1103/PhysRevD.16.1791.

[5] Steven Weinberg. "A New Light Boson?" In: *Phys. Rev. Lett.* 40 (1978), pp. 223–226. DOI: 10.1103/PhysRevLett.40.223.

[6] Frank Wilczek. "Problem of Strong P and T Invariance in the Presence of Instantons". In: *Phys. Rev. Lett.* 40 (1978), pp. 279–282. DOI: 10.1103/PhysRevLett.40.279.

[7] Jihn E. Kim. "Weak Interaction Singlet and Strong CP Invariance". In: *Phys. Rev. Lett.* 43 (1979), p. 103. DOI: 10.1103/PhysRevLett.43.103.

[8] Mikhail A. Shifman, A. I. Vainshtein, and Valentin I. Zakharov. "Can Confinement Ensure Natural CP Invariance of Strong Interactions?" In: *Nucl. Phys. B* 166 (1980), pp. 493–506. DOI: 10.1016/0550-3213(80)90209-6.

[9] Michael Dine, Willy Fischler, and Mark Srednicki. "A Simple Solution to the Strong CP Problem with a Harmless Axion". In: *Phys. Lett. B* 104 (1981), pp. 199–202. DOI: 10.1016/0370-2693(81)90590-6.

[10] A. R. Zhitnitsky. "On Possible Suppression of the Axion Hadron Interactions. (In Russian)". In: *Sov. J. Nucl. Phys.* 31 (1980), p. 260.

[11] David J. E. Marsh. "Axion Cosmology". In: *Phys. Rept.* 643 (2016), pp. 1–79. DOI: 10.1016/j.physrep.2016.06.005. arXiv: 1510.07633 [astro-ph.CO].

[12] David J. E. Marsh. "Axions for amateurs". In: *Contemp. Phys.* 64.1 (2023), pp. 1–18. DOI: 10.1080/00107514.2023.2256085. arXiv: 2308.16003 [physics.pop-ph].

[13] Masha Baryakhtar, Leslie Rosenberg, and Gray Rybka. "Searching for the QCD Dark Matter Axion". In: (Apr. 2025). arXiv: 2504.10607 [hep-ex].

[14] Peter Svrcek and Edward Witten. "Axions In String Theory". In: *JHEP* 06 (2006), p. 051. DOI: 10.1088/1126-6708/2006/06/051. arXiv: hep-th/0605206.

[15] Asimina Arvanitaki et al. "String Axiverse". In: *Phys. Rev. D* 81 (2010), p. 123530. DOI: 10.1103/PhysRevD.81.123530. arXiv: 0905.4720 [hep-th].

[16] Asimina Arvanitaki and Sergei Dubovsky. "Exploring the String Axiverse with Precision Black Hole Physics". In: *Phys. Rev. D* 83 (2011), p. 044026. DOI: 10.1103/PhysRevD.83.044026. arXiv: 1004.3558 [hep-th].

[17] Hiroyuki Tashiro, Joseph Silk, and David J. E. Marsh. "Constraints on primordial magnetic fields from CMB distortions in the axiverse". In: *Phys. Rev. D* 88.12 (2013), p. 125024. DOI: 10.1103/PhysRevD.88.125024. arXiv: 1308.0314 [astro-ph.CO].

[18] Joshua W. Foster et al. "Dark Grand Unification in the axiverse: decaying axion dark matter and spontaneous baryogenesis". In: *JHEP* 12 (2022), p. 119. DOI: 10.1007/JHEP12(2022)119. arXiv: 2208.10504 [hep-ph].

[19] Naomi Gendler et al. "Glimmers from the axiverse". In: *JCAP* 09 (2024), p. 071. DOI: 10.1088/1475-7516/2024/09/071. arXiv: 2309.13145 [hep-th].

[20] Stephon Alexander, Tucker Manton, and Evan McDonough. "Field theory axiverse". In: *Phys. Rev. D* 109.11 (2024), p. 116019. DOI: 10.1103/PhysRevD.109.116019. arXiv: 2404.11642 [hep-ph].

[21] Joseph P. Conlon. "Out of the Dark: WISPs in String Theory and the Early Universe". In: *PoS* COSMICWISPers (2024), p. 001. DOI: 10.22323/1.454.0001. arXiv: 2402.04725 [hep-th].

[22] Matthew Reece. "Extra-dimensional axion expectations". In: *JHEP* 07 (2025), p. 130. DOI: 10.1007/JHEP07(2025)130. arXiv: 2406.08543 [hep-ph].

[23] Naomi Gendler and David J. E. Marsh. "Possible Implications of QCD Axion Dark Matter Constraints from Helioscopes and Haloscopes for the String Theory Landscape". In: *Phys. Rev. Lett.* 134.8 (2025), p. 081602. DOI: 10.1103/PhysRevLett.134.081602. arXiv: 2407.07143 [hep-th].

[24] Prateek Agrawal, Michael Nee, and Mario Reig. "Axion couplings in heterotic string theory". In: *JHEP* 02 (2025), p. 188. DOI: 10.1007/JHEP02(2025)188. arXiv: 2410.03820 [hep-ph].

[25] Andreas Ringwald. "Searching for axions and ALPs from string theory". In: *J. Phys. Conf. Ser.* 485 (2014). Ed. by Myriam Mondragón et al., p. 012013. DOI: 10.1088/1742-6596/485/1/012013. arXiv: 1209.2299 [hep-ph].

[26] Francesca Chadha-Day, John Ellis, and David J. E. Marsh. "Axion dark matter: What is it and why now?" In: *Sci. Adv.* 8.8 (2022), abj3618. DOI: 10.1126/sciadv.abj3618. arXiv: 2105.01406 [hep-ph].

[27] Matthew Reece. "TASI Lectures: (No) Global Symmetries to Axion Physics". In: *PoS* TASI2022 (2024), p. 008. DOI: 10.22323/1.439.0008. arXiv: 2304.08512 [hep-ph].

[28] Kiwoon Choi and Nicole Righi. "Axion theory and model building". In: *PoS* COSMICWISPers (2024), p. 039. DOI: 10.22323/1.454.0039. arXiv: 2401.17354 [hep-th].

[29] Peter W. Graham et al. "Experimental Searches for the Axion and Axion-Like Particles". In: *Ann. Rev. Nucl. Part. Sci.* 65 (2015), pp. 485–514. DOI: 10.1146/annurev-nucl-102014-022120. arXiv: 1602.00039 [hep-ex].

[30] Igor G. Irastorza and Javier Redondo. "New experimental approaches in the search for axion-like particles". In: *Prog. Part. Nucl. Phys.* 102 (2018), pp. 89–159. DOI: 10.1016/j.ppnp.2018.05.003. arXiv: 1801.08127 [hep-ph].

[31] P. Sikivie. "Experimental Tests of the Invisible Axion". In: *Phys. Rev. Lett.* 51 (1983). Ed. by M. A. Srednicki. [Erratum: Phys.Rev.Lett. 52, 695 (1984)], pp. 1415–1417. DOI: 10.1103/PhysRevLett.51.1415.

[32] K. Zioutas et al. "First results from the CERN Axion Solar Telescope (CAST)". In: *Phys. Rev. Lett.* 94 (2005), p. 121301. DOI: 10.1103/PhysRevLett.94.121301. arXiv: hep-ex/0411033.

[33] S. Andriamonje et al. “An Improved limit on the axion-photon coupling from the CAST experiment”. In: *JCAP* 04 (2007), p. 010. DOI: 10.1088/1475-7516/2007/04/010. arXiv: hep-ex/0702006.

[34] E. Arik et al. “Probing eV-scale axions with CAST”. In: *JCAP* 02 (2009), p. 008. DOI: 10.1088/1475-7516/2009/02/008. arXiv: 0810.4482 [hep-ex].

[35] S. Aune et al. “CAST search for sub-eV mass solar axions with 3He buffer gas”. In: *Phys. Rev. Lett.* 107 (2011), p. 261302. DOI: 10.1103/PhysRevLett.107.261302. arXiv: 1106.3919 [hep-ex].

[36] M. Arik et al. “Search for Solar Axions by the CERN Axion Solar Telescope with ^{3}He Buffer Gas: Closing the Hot Dark Matter Gap”. In: *Phys. Rev. Lett.* 112.9 (2014), p. 091302. DOI: 10.1103/PhysRevLett.112.091302. arXiv: 1307.1985 [hep-ex].

[37] M. Arik et al. “New solar axion search using the CERN Axion Solar Telescope with ^{4}He filling”. In: *Phys. Rev. D* 92.2 (2015), p. 021101. DOI: 10.1103/PhysRevD.92.021101. arXiv: 1503.00610 [hep-ex].

[38] V. Anastassopoulos et al. “New CAST Limit on the Axion-Photon Interaction”. In: *Nature Phys.* 13 (2017), pp. 584–590. DOI: 10.1038/nphys4109. arXiv: 1705.02290 [hep-ex].

[39] K. Altenmüller et al. “New Upper Limit on the Axion-Photon Coupling with an Extended CAST Run with a Xe-Based Micromegas Detector”. In: *Phys. Rev. Lett.* 133.22 (2024), p. 221005. DOI: 10.1103/PhysRevLett.133.221005. arXiv: 2406.16840 [hep-ex].

[40] E. Armengaud et al. “Physics potential of the International Axion Observatory (IAXO)”. In: *JCAP* 06 (2019), p. 047. DOI: 10.1088/1475-7516/2019/06/047. arXiv: 1904.09155 [hep-ph].

[41] A. Abeln et al. “Conceptual design of BabyIAXO, the intermediate stage towards the International Axion Observatory”. In: *JHEP* 05 (2021), p. 137. DOI: 10.1007/JHEP05(2021)137. arXiv: 2010.12076 [physics.ins-det].

[42] D. Basilico et al. “Search for high energy 5.5 MeV solar axions with the complete Borexino dataset”. In: *Eur. Phys. J. C* 85.10 (2025), p. 1182. DOI: 10.1140/epjc/s10052-025-14811-9. arXiv: 2504.19135 [hep-ex].

[43] Stephen J. Asztalos et al. “Large scale microwave cavity search for dark matter axions”. In: *Phys. Rev. D* 64 (2001), p. 092003. DOI: 10.1103/PhysRevD.64.092003.

[44] S. J. Asztalos et al. “An Improved RF cavity search for halo axions”. In: *Phys. Rev. D* 69 (2004), p. 011101. DOI: 10.1103/PhysRevD.69.011101. arXiv: astro-ph/0310042.

[45] Leanne D. Duffy et al. “A high resolution search for dark-matter axions”. In: *Phys. Rev. D* 74 (2006), p. 012006. DOI: 10.1103/PhysRevD.74.012006. arXiv: astro-ph/0603108.

[46] S. J. Asztalos et al. “A SQUID-based microwave cavity search for dark-matter axions”. In: *Phys. Rev. Lett.* 104 (2010), p. 041301. DOI: 10.1103/PhysRevLett.104.041301. arXiv: 0910.5914 [astro-ph.CO].

[47] J. Hoskins et al. “Modulation sensitive search for nonvirialized dark-matter axions”. In: *Phys. Rev. D* 94.8 (2016), p. 082001. DOI: 10.1103/PhysRevD.94.082001. arXiv: 1804.08770 [astro-ph.CO].

[48] N. Du et al. “A Search for Invisible Axion Dark Matter with the Axion Dark Matter Experiment”. In: *Phys. Rev. Lett.* 120.15 (2018), p. 151301. DOI: 10.1103/PhysRevLett.120.151301. arXiv: 1804.05750 [hep-ex].

[49] T. Braine et al. “Extended Search for the Invisible Axion with the Axion Dark Matter Experiment”. In: *Phys. Rev. Lett.* 124.10 (2020), p. 101303. DOI: 10.1103/PhysRevLett.124.101303. arXiv: 1910.08638 [hep-ex].

[50] R. Khatiwada et al. “Axion Dark Matter Experiment: Detailed design and operations”. In: *Rev. Sci. Instrum.* 92.12 (2021), p. 124502. DOI: 10.1063/5.0037857. arXiv: 2010.00169 [astro-ph.IM].

[51] C. M. Adair et al. “Search for Dark Matter Axions with CAST-CAPP”. In: *Nature Commun.* 13.1 (2022), p. 6180. DOI: 10.1038/s41467-022-33913-6. arXiv: 2211.02902 [hep-ex].

[52] Klaus Ehret et al. “New ALPS Results on Hidden-Sector Lightweights”. In: *Phys. Lett. B* 689 (2010), pp. 149–155. DOI: 10.1016/j.physletb.2010.04.066. arXiv: 1004.1313 [hep-ex].

[53] Katharina-Sophie Isleif. “The Any Light Particle Search Experiment at DESY”. In: *Moscow Univ. Phys. Bull.* 77.2 (2022), pp. 120–125. DOI: 10.3103/S002713492202045X. arXiv: 2202.07306 [hep-ex].

[54] Daniel C. Brotherton et al. “Any Light Particle Searches with ALPS II: first science results”. In: (Dec. 2025). arXiv: 2512.14110 [hep-ex].

[55] R. Ballou et al. “New exclusion limits on scalar and pseudoscalar axionlike particles from light shining through a wall”. In: *Phys. Rev. D* 92.9 (2015), p. 092002. DOI: 10.1103/PhysRevD.92.092002. arXiv: 1506.08082 [hep-ex].

[56] Alessandro Mirizzi, Javier Redondo, and Gunter Sigl. “Constraining resonant photon-axion conversions in the Early Universe”. In: *JCAP* 08 (2009), p. 001. DOI: 10.1088/1475-7516/2009/08/001. arXiv: 0905.4865 [hep-ph].

[57] Nicola Bassan, Alessandro Mirizzi, and Marco Roncadelli. “Axion-like particle effects on the polarization of cosmic high-energy gamma sources”. In: *JCAP* 05 (2010), p. 010. DOI: 10.1088/1475-7516/2010/05/010. arXiv: 1001.5267 [astro-ph.HE].

[58] Denis Wouters and Pierre Brun. “Constraints on Axion-like Particles from X-Ray Observations of the Hydra Galaxy Cluster”. In: *Astrophys. J.* 772 (2013), p. 44. DOI: 10.1088/0004-637X/772/1/44. arXiv: 1304.0989 [astro-ph.HE].

[59] Alexandre Payez et al. “Revisiting the SN1987A gamma-ray limit on ultralight axion-like particles”. In: *JCAP* 02 (2015), p. 006. DOI: 10.1088/1475-7516/2015/02/006. arXiv: 1410.3747 [astro-ph.HE].

[60] M. Meyer et al. “Fermi Large Area Telescope as a Galactic Supernovae Axionscope”. In: *Phys. Rev. Lett.* 118.1 (2017), p. 011103. DOI: 10.1103/PhysRevLett.118.011103. arXiv: 1609.02350 [astro-ph.HE].

[61] Maurizio Giannotti et al. “Stellar Recipes for Axion Hunters”. In: *JCAP* 10 (2017), p. 010. DOI: 10.1088/1475-7516/2017/10/010. arXiv: 1708.02111 [hep-ph].

[62] M. C. David Marsh et al. “A New Bound on Axion-Like Particles”. In: *JCAP* 12 (2017), p. 036. DOI: 10.1088/1475-7516/2017/12/036. arXiv: 1703.07354 [hep-ph].

[63] Christopher S. Reynolds et al. “Astrophysical limits on very light axion-like particles from Chandra grating spectroscopy of NGC 1275”. In: *Astrophys. J.* 890 (2020), p. 59. DOI: 10.3847/1538-4357/ab6a0c. arXiv: 1907.05475 [hep-ph].

[64] Júlia Sisk Reynés et al. “New constraints on light axion-like particles using Chandra transmission grating spectroscopy of the powerful cluster-hosted quasar H1821+643”. In: *Mon. Not. Roy. Astron. Soc.* 510.1 (2021), pp. 1264–1277. DOI: 10.1093/mnras/stab3464. arXiv: 2109.03261 [astro-ph.HE].

[65] Francesca Calore et al. “Bounds on axionlike particles from the diffuse supernova flux”. In: *Phys. Rev. D* 102.12 (2020), p. 123005. DOI: 10.1103/PhysRevD.102.123005. arXiv: 2008.11741 [hep-ph].

[66] Pierluca Carenza et al. “Enhanced Supernova Axion Emission and its Implications”. In: *Phys. Rev. Lett.* 126.7 (2021), p. 071102. DOI: 10.1103/PhysRevLett.126.071102. arXiv: 2010.02943 [hep-ph].

[67] Melissa Diamond et al. “Axion-sourced fireballs from supernovae”. In: *Phys. Rev. D* 107.10 (2023). [Erratum: Phys.Rev.D 108, 049902 (2023)], p. 103029. DOI: 10.1103/PhysRevD.107.103029. arXiv: 2303.11395 [hep-ph].

[68] Dion Noordhuis et al. “Novel Constraints on Axions Produced in Pulsar Polar-Cap Cascades”. In: *Phys. Rev. Lett.* 131.11 (2023), p. 111004. DOI: 10.1103/PhysRevLett.131.111004. arXiv: 2209.09917 [hep-ph].

[69] Sebastian Hoof and Lena Schulz. “Updated constraints on axion-like particles from temporal information in supernova SN1987A gamma-ray data”. In: *JCAP* 03 (2023), p. 054. DOI: 10.1088/1475-7516/2023/03/054. arXiv: 2212.09764 [hep-ph].

[70] Konstantin Springmann et al. “Universal bound on QCD axions from supernovae”. In: *Phys. Rev. D* 112.7 (2025), p. 075009. DOI: 10.1103/18t2-1w3b. arXiv: 2410.19902 [hep-ph].

[71] Zixuan Xu and Sibo Zheng. “Lyman-α limit on axionlike cold dark matter”. In: *Phys. Rev. D* 111.6 (2025), p. 063525. DOI: 10.1103/PhysRevD.111.063525. arXiv: 2410.15675 [hep-ph].

[72] Bryce Cyr, Jens Chluba, and Pranav Bharadwaj Gangrekalve Manoj. “Revisiting Constraints on Resonant Axion-Photon Conversions from CMB Spectral Distortions”. In: (Nov. 2024). arXiv: 2411.13701 [astro-ph.CO].

[73] Alessandro Lella et al. “Protoneutron stars as cosmic factories for massive axionlike particles”. In: *Phys. Rev. D* 107.10 (2023), p. 103017. DOI: 10.1103/PhysRevD.107.103017. arXiv: 2211.13760 [hep-ph].

[74] Alessandro Lella et al. “Getting the most on supernova axions”. In: *Phys. Rev. D* 109.2 (2024), p. 023001. DOI: 10.1103/PhysRevD.109.023001. arXiv: 2306.01048 [hep-ph].

[75] Alessandro Lella et al. “Supernova limits on QCD axionlike particles”. In: *Phys. Rev. D* 110.4 (2024), p. 043019. DOI: 10.1103/PhysRevD.110.043019. arXiv: 2405.00153 [hep-ph].

[76] Alessandro Lella et al. “Probing protoneutron stars with gamma-ray axionscopes”. In: *JCAP* 11 (2024), p. 009. DOI: 10.1088/1475-7516/2024/11/009. arXiv: 2405.02395 [hep-ph].

[77] Claudio Andrea Manzari et al. “Supernova Axions Convert to Gamma Rays in Magnetic Fields of Progenitor Stars”. In: *Phys. Rev. Lett.* 133.21 (2024), p. 211002. DOI: 10.1103/PhysRevLett.133.211002. arXiv: 2405.19393 [hep-ph].

[78] Pierluca Carenza et al. “Improved axion emissivity from a supernova via nucleon-nucleon bremsstrahlung”. In: *JCAP* 10.10 (2019). [Erratum: JCAP 05, E01 (2020)], p. 016. DOI: 10.1088/1475-7516/2019/10/016. arXiv: 1906.11844 [hep-ph].

[79] Gautham Adamane Pallathadka et al. “Reconciling hints on axion-like-particles from high-energy gamma rays with stellar bounds”. In: *JCAP* 11 (2021), p. 036. DOI: 10.1088/1475-7516/2021/11/036. arXiv: 2008.08100 [hep-ph].

[80] Pierluca Carenza. “Axion emission from supernovae: a cheatsheet”. In: *Eur. Phys. J. Plus* 138.9 (2023), p. 836. DOI: 10.1140/epjp/s13360-023-04484-2. arXiv: 2309.14798 [hep-ph].

[81] P. Carenza et al. “Detecting supernova axions with IAXO”. In: *JCAP* 07 (2025), p. 075. DOI: 10.1088/1475-7516/2025/07/075. arXiv: 2502.19476 [hep-ph].

[82] Júlia Sisk-Reynés et al. “Physics Beyond the Standard Model with Future X-Ray Observatories: Projected Constraints on Very-light Axion-like Particles with Athena and AXIS”. In: *Astrophys. J.* 951.1 (2023), p. 5. DOI: 10.3847/1538-4357/acd116. arXiv: 2211.05136 [astro-ph.HE].

[83] Giorgio Galanti et al. “ALP induced polarization effects on photons from galaxy clusters”. In: *Phys. Rev. D* 107.10 (2023), p. 103007. DOI: 10.1103/PhysRevD.107.103007. arXiv: 2202.12286 [astro-ph.HE].

[84] Giorgio Galanti. “Photon-ALP oscillations inducing modifications to photon polarization”. In: *Phys. Rev. D* 107.4 (2023), p. 043006. DOI: 10.1103/PhysRevD.107.043006. arXiv: 2202.11675 [astro-ph.HE].

[85] Andrea Caputo and Georg Raffelt. “Astrophysical Axion Bounds: The 2024 Edition”. In: *PoS* COSMICWISPers (2024), p. 041. DOI: 10.22323/1.454.0041. arXiv: 2401.13728 [hep-ph].

[86] Pierluca Carenza et al. “Axion astrophysics”. In: *Phys. Rept.* 1117 (2025), pp. 1–102. DOI: 10.1016/j.physrep.2025.02.002. arXiv: 2411.02492 [hep-ph].

[87] Alessandro Mirizzi, Georg G. Raffelt, and Pasquale D. Serpico. “Signatures of Axion-Like Particles in the Spectra of TeV Gamma-Ray Sources”. In: *Phys. Rev. D* 76 (2007), p. 023001. DOI: 10.1103/PhysRevD.76.023001. arXiv: 0704.3044 [astro-ph].

[88] Dan Hooper and Pasquale D. Serpico. “Detecting Axion-Like Particles With Gamma Ray Telescopes”. In: *Phys. Rev. Lett.* 99 (2007), p. 231102. DOI: 10.1103/PhysRevLett.99.231102. arXiv: 0706.3203 [hep-ph].

[89] Alessandro De Angelis, Marco Roncadelli, and Oriana Mansutti. “Evidence for a new light spin-zero boson from cosmological gamma-ray propagation?” In: *Phys. Rev. D* 76 (2007), p. 121301. DOI: 10.1103/PhysRevD.76.121301. arXiv: 0707.4312 [astro-ph].

[90] Alessandro De Angelis, Oriana Mansutti, and Marco Roncadelli. “Axion-Like Particles, Cosmic Magnetic Fields and Gamma-Ray Astrophysics”. In: *Phys. Lett. B* 659 (2008), pp. 847–855. DOI: 10.1016/j.physletb.2007.12.012. arXiv: 0707.2695 [astro-ph].

[91] Kathrin A. Hochmuth and Guenter Sigl. “Effects of Axion-Photon Mixing on Gamma-Ray Spectra from Magnetized Astrophysical Sources”. In: *Phys. Rev. D* 76 (2007), p. 123011. DOI: 10.1103/PhysRevD.76.123011. arXiv: 0708.1144 [astro-ph].

[92] Melanie Simet, Dan Hooper, and Pasquale D. Serpico. “The Milky Way as a Kiloparsec-Scale Axionscope”. In: *Phys. Rev. D* 77 (2008), p. 063001. DOI: 10.1103/PhysRevD.77.063001. arXiv: 0712.2825 [astro-ph].

[93] M. A. Sanchez-Conde et al. “Hints of the existence of Axion-Like-Particles from the gamma-ray spectra of cosmological sources”. In: *Phys. Rev. D* 79 (2009), p. 123511. DOI: 10.1103/PhysRevD.79.123511. arXiv: 0905.3270 [astro-ph.CO].

[94] Nicola Bassan and Marco Roncadelli. “Photon-axion conversion in Active Galactic Nuclei?” In: (May 2009). arXiv: 0905.3752 [astro-ph.HE].

[95] Alessandro Mirizzi and Daniele Montanino. “Stochastic conversions of TeV photons into axion-like particles in extragalactic magnetic fields”. In: *JCAP* 12 (2009), p. 004. DOI: 10.1088/1475-7516/2009/12/004. arXiv: 0911.0015 [astro-ph.HE].

[96] Alexander V. Belikov, Lisa Goodenough, and Dan Hooper. "No Indications of Axion-Like Particles From Fermi". In: *Phys. Rev. D* 83 (2011), p. 063005. DOI: 10.1103/PhysRevD.83.063005. arXiv: 1007.4862 [astro-ph.HE].

[97] Alessandro De Angelis, Giorgio Galanti, and Marco Roncadelli. "Relevance of axion-like particles for very-high-energy astrophysics". In: *Phys. Rev. D* 84 (2011). [Erratum: Phys.Rev.D 87, 109903 (2013)], p. 105030. DOI: 10.1103/PhysRevD.84.105030. arXiv: 1106.1132 [astro-ph.HE].

[98] Fabrizio Tavecchio et al. "Evidence for an axion-like particle from PKS 1222+216?" In: *Phys. Rev. D* 86 (2012), p. 085036. DOI: 10.1103/PhysRevD.86.085036. arXiv: 1202.6529 [astro-ph.HE].

[99] Dieter Horns et al. "Hardening of TeV gamma spectrum of AGNs in galaxy clusters by conversions of photons into axion-like particles". In: *Phys. Rev. D* 86 (2012), p. 075024. DOI: 10.1103/PhysRevD.86.075024. arXiv: 1207.0776 [astro-ph.HE].

[100] Manuel Meyer, Dieter Horns, and Martin Raue. "First lower limits on the photon-axion-like particle coupling from very high energy gamma-ray observations". In: *Phys. Rev. D* 87.3 (2013), p. 035027. DOI: 10.1103/PhysRevD.87.035027. arXiv: 1302.1208 [astro-ph.HE].

[101] A. Abramowski et al. "Constraints on axionlike particles with H.E.S.S. from the irregularity of the PKS 2155-304 energy spectrum". In: *Phys. Rev. D* 88.10 (2013), p. 102003. DOI: 10.1103/PhysRevD.88.102003. arXiv: 1311.3148 [astro-ph.HE].

[102] Manuel Meyer, Daniele Montanino, and Jan Conrad. "On detecting oscillations of gamma rays into axion-like particles in turbulent and coherent magnetic fields". In: *JCAP* 09 (2014), p. 003. DOI: 10.1088/1475-7516/2014/09/003. arXiv: 1406.5972 [astro-ph.HE].

[103] Manuel Meyer and J. Conrad. "Sensitivity of the Cherenkov Telescope Array to the detection of axion-like particles at high gamma-ray opacities". In: *JCAP* 12 (2014), p. 016. DOI: 10.1088/1475-7516/2014/12/016. arXiv: 1410.1556 [astro-ph.HE].

[104] Alexandra Dobrynina, Alexander Kartavtsev, and Georg Raffelt. "Photon-photon dispersion of TeV gamma rays and its role for photon-ALP conversion". In: *Phys. Rev. D* 91 (2015). [Erratum: Phys.Rev.D 95, 109905 (2017)], p. 083003. DOI: 10.1103/PhysRevD.91.083003. arXiv: 1412.4777 [astro-ph.HE].

[105] A. Kartavtsev, G. Raffelt, and H. Vogel. "Extragalactic photon-ALP conversion at CTA energies". In: *JCAP* 01 (2017), p. 024. DOI: 10.1088/1475-7516/2017/01/024. arXiv: 1611.04526 [astro-ph.HE].

[106] Manuel Meyer. "Searches for Axionlike Particles Using γ-Ray Observations". In: *12th Patras Workshop on Axions, WIMPs and WISPs*. 2017, pp. 102–111. DOI: 10.3204/DESY-PROC-2009-03/Meyer_Manuel. arXiv: 1611.07784 [astro-ph.HE].

[107] Hendrik Vogel, Ranjan Laha, and Manuel Meyer. "Diffuse axion-like particle searches". In: *PoS* NOW2018 (2019). Ed. by Antonio Marrone, Alessandro Mirizzi, and Daniele Montanino, p. 091. DOI: 10.22323/1.337.0091. arXiv: 1712.01839 [hep-ph].

[108] Kazunori Kohri and Hideo Kodama. "Axion-Like Particles and Recent Observations of the Cosmic Infrared Background Radiation". In: *Phys. Rev. D* 96.5 (2017), p. 051701. DOI: 10.1103/PhysRevD.96.051701. arXiv: 1704.05189 [hep-ph].

[109] Jhilik Majumdar, Francesca Calore, and Dieter Horns. "Search for gamma-ray spectral modulations in Galactic pulsars". In: *JCAP* 04 (2018), p. 048. DOI: 10.1088/1475-7516/2018/04/048. arXiv: 1801.08813 [hep-ph].

[110] Cun Zhang et al. "New bounds on axionlike particles from the Fermi Large Area Telescope observation of PKS 2155-304". In: *Phys. Rev. D* 97.6 (2018), p. 063009. DOI: 10.1103/PhysRevD.97.063009. arXiv: 1802.08420 [hep-ph].

[111] Giorgio Galanti et al. "Blazar VHE spectral alterations induced by photon–ALP oscillations". In: *Mon. Not. Roy. Astron. Soc.* 487.1 (2019), pp. 123–132. DOI: 10.1093/mnras/stz1144. arXiv: 1811.03548 [astro-ph.HE].

[112] G. B. Long et al. "Testing the CIBER cosmic infrared background measurements and axionlike particles with observations of TeV blazars". In: *Phys. Rev. D* 101.6 (2020), p. 063004. DOI: 10.1103/PhysRevD.101.063004. arXiv: 1912.05309 [astro-ph.HE].

[113] R. Buehler et al. "Search for the imprint of axion-like particles in the highest-energy photons of hard γ-ray blazars". In: *JCAP* 09 (2020), p. 027. DOI: 10.1088/1475-7516/2020/09/027. arXiv: 2004.09396 [astro-ph.HE].

[114] Leonardo Mastrototaro et al. "Constraining axion-like particles with the diffuse gamma-ray flux measured by the Large High Altitude Air Shower Observatory". In: *Eur. Phys. J. C* 82.11 (2022), p. 1012. DOI: 10.1140/epjc/s10052-022-10979-6. arXiv: 2206.08945 [hep-ph].

[115] L. J. Dong et al. “Photon-ALP beam propagation from Mrk 501”. In: *Phys. Rev. D* 111.6 (2025), p. 063073. DOI: 10.1103/PhysRevD.111.063073. arXiv: 2502.20804 [astro-ph.HE].

[116] Ji-Gui Cheng et al. “Revisiting the analysis of axion-like particles with the Fermi-LAT gamma-ray observation of NGC1275”. In: *Phys. Lett. B* 821 (2021), p. 136611. DOI: 10.1016/j.physletb.2021.136611. arXiv: 2010.12396 [astro-ph.HE].

[117] James Davies, Manuel Meyer, and Garret Cotter. “Relevance of jet magnetic field structure for blazar axionlike particle searches”. In: *Phys. Rev. D* 103.2 (2021), p. 023008. DOI: 10.1103/PhysRevD.103.023008. arXiv: 2011.08123 [astro-ph.HE].

[118] Junguang Guo et al. “Implications of axion-like particles from the Fermi-LAT and H.E.S.S. observations of PG 1553+113 and PKS 2155−304”. In: *Chin. Phys. C* 45.2 (2021), p. 025105. DOI: 10.1088/1674-1137/abcd2e. arXiv: 2002.07571 [astro-ph.HE].

[119] Christopher Eckner and Francesca Calore. “First constraints on axionlike particles from Galactic sub-PeV gamma rays”. In: *Phys. Rev. D* 106.8 (2022), p. 083020. DOI: 10.1103/PhysRevD.106.083020. arXiv: 2204.12487 [astro-ph.HE].

[120] Lin-Qing Gao et al. “Constraints on axionlike particles from observations of Mrk 421 using the CLs method”. In: *Phys. Rev. D* 109.6 (2024), p. 063003. DOI: 10.1103/PhysRevD.109.063003. arXiv: 2309.02166 [astro-ph.HE].

[121] Bhanu Prakash Pant et al. “Implications of photon-ALP oscillations in the extragalactic neutrino source TXS 0506+056 at sub-PeV energies”. In: *Phys. Rev. D* 108.2 (2023), p. 023016. DOI: 10.1103/PhysRevD.108.023016. arXiv: 2210.12652 [astro-ph.HE].

[122] Bhanu Prakash Pant. “Constraining axionlike particles with invisible neutrino decay using the IceCube observations of NGC 1068”. In: *Phys. Rev. D* 109.6 (2024), p. 063002. DOI: 10.1103/PhysRevD.109.063002. arXiv: 2311.14597 [astro-ph.HE].

[123] Bhanu Prakash Pant. “Probing photon-ALP oscillations from the MAGIC observations of FSRQ QSO B1420+326”. In: *Phys. Rev. D* 109.2 (2024), p. 023011. DOI: 10.1103/PhysRevD.109.023011. arXiv: 2310.16634 [astro-ph.HE].

[124] Yu-Chong Chen et al. “Constraining axionlike particles from observations of AGN B2 2234+28A and 3C 454.3”. In: *Phys. Rev. D* 111.8 (2025), p. 083002. DOI: 10.1103/PhysRevD.111.083002. arXiv: 2411.08577 [astro-ph.HE].

[125] Francisco R. Candón et al. “Probing the Axion-Nucleon Coupling with Supergiant Stars”. In: (Apr. 2025). arXiv: 2504.21107 [hep-ph].

[126] A. Pratts et al. “Axion-like Particles and their Possible Impact on the Very High-Energy Spectrum of M87 Observed by LHAASO”. In: (July 2025). arXiv: 2507.05637 [astro-ph.HE].

[127] M. Kachelriess and J. Tjemsland. “Detecting ALP wiggles at TeV energies”. In: *JCAP* 01 (2024), p. 044. DOI: 10.1088/1475-7516/2024/01/044. arXiv: 2305.03604 [hep-ph].

[128] Sunniva Jacobsen, Tim Linden, and Katherine Freese. “Constraining axion-like particles with HAWC observations of TeV blazars”. In: *JCAP* 10 (2023), p. 009. DOI: 10.1088/1475-7516/2023/10/009. arXiv: 2203.04332 [hep-ph].

[129] Rahul Cecil and Manuel Meyer. “Modeling the Magnetic Field of the Virgo Cluster For Axion Like Particle Search in Gamma Ray Energies”. In: *PoS* Gamma2022 (2023), p. 182. DOI: 10.22323/1.417.0182.

[130] Rahul Cecil et al. “Probing Gamma-Ray Propagation at Very-High Energies with H.E.S.S. Observations of M87”. In: *PoS* ICRC2023 (2024), p. 908. DOI: 10.22323/1.444.0908.

[131] James Davies, Manuel Meyer, and Garret Cotter. “Constraints on axionlike particles from a combined analysis of three flaring Fermi flat-spectrum radio quasars”. In: *Phys. Rev. D* 107.8 (2023), p. 083027. DOI: 10.1103/PhysRevD.107.083027. arXiv: 2211.03414 [astro-ph.HE].

[132] M. Ajello et al. “Search for Spectral Irregularities due to Photon–Axionlike-Particle Oscillations with the Fermi Large Area Telescope”. In: *Phys. Rev. Lett.* 116.16 (2016), p. 161101. DOI: 10.1103/PhysRevLett.116.161101. arXiv: 1603.06978 [astro-ph.HE].

[133] H. Abe et al. “Constraints on axion-like particles with the Perseus Galaxy Cluster with MAGIC”. In: *Phys. Dark Univ.* 44 (2024), p. 101425. DOI: 10.1016/j.dark.2024.101425. arXiv: 2401.07798 [astro-ph.HE].

[134] C. B. Adams et al. “Constraints on axionlike particles from VERITAS observations of a flaring radio galaxy in the Perseus cluster”. In: *Phys. Rev. D* 112.10 (2025), p. 103044. DOI: 10.1103/jydc-npy6. arXiv: 2510.19010 [astro-ph.HE].

[135] Hai-Jun Li et al. “Limits on axion-like particles from Mrk 421 with 4.5-year period observations by ARGO-YBJ and Fermi-LAT”. In: *Phys. Rev. D* 103.8 (2021), p. 083003. DOI: 10.1103/PhysRevD.103.083003. arXiv: 2008.09464 [astro-ph.HE].

[136] Hai-Jun Li, Xiao-Jun Bi, and Peng-Fei Yin. “Searching for axion-like particles with the blazar observations of MAGIC and Fermi-LAT *”. In: *Chin. Phys. C* 46.8 (2022), p. 085105. DOI: 10.1088/1674-1137/ac6d4f. arXiv: 2110.13636 [astro-ph.HE].

[137] Hai-Jun Li, Wei Chao, and Yu-Feng Zhou. “Upper limit on the axion-photon coupling from Markarian 421”. In: *Phys. Lett. B* 858 (2024), p. 139075. DOI: 10.1016/j.physletb.2024.139075. arXiv: 2406.00387 [hep-ph].

[138] Lin-Qing Gao et al. “Impact of Parameters in the Blazar Jet Magnetic Field Model on Axion-Like Particle Constraints”. In: (July 2024). arXiv: 2407.20118 [astro-ph.HE].

[139] Zi-Qing Xia et al. “Searching for spectral oscillations due to photon-axionlike particle conversion using the Fermi-LAT observations of bright supernova remnants”. In: *Phys. Rev. D* 97.6 (2018), p. 063003. DOI: 10.1103/PhysRevD.97.063003. arXiv: 1801.01646 [astro-ph.HE].

[140] Yun-Feng Liang et al. “Constraints on axion-like particle properties with TeV gamma-ray observations of Galactic sources”. In: *JCAP* 06 (2019), p. 042. DOI: 10.1088/1475-7516/2019/06/042. arXiv: 1804.07186 [hep-ph].

[141] Zi-Qing Xia et al. “Searching for the possible signal of the photon-axionlike particle oscillation in the combined GeV and TeV spectra of supernova remnants”. In: *Phys. Rev. D* 100.12 (2019), p. 123004. DOI: 10.1103/PhysRevD.100.123004. arXiv: 1911.08096 [astro-ph.HE].

[142] Xiao-Jun Bi et al. “Axion and dark photon limits from Crab Nebula high energy gamma-rays”. In: *Phys. Rev. D* 103.4 (2021), p. 043018. DOI: 10.1103/PhysRevD.103.043018. arXiv: 2002.01796 [astro-ph.HE].

[143] Jun Li et al. “Constraints on Axion-like Particles from the Observation of Galactic Sources by LHAASO”. In: (Jan. 2024). arXiv: 2401.01829 [astro-ph.HE].

[144] Kazunori Kohri and Haruki Takahashi. “New constraints on axion with gamma-ray observations of the Crab Nebula”. In: (Nov. 2025). arXiv: 2511.19848 [hep-ph].

[145] Jonathan Biteau and Manuel Meyer. "Gamma-Ray Cosmology and Tests of Fundamental Physics". In: *Galaxies* 10.2 (2022), p. 39. DOI: 10.3390/galaxies10020039. arXiv: 2202.00523 [astro-ph.CO].

[146] Giorgio Galanti and Marco Roncadelli. "Axion-like Particles Implications for High-Energy Astrophysics". In: *Universe* 8.5 (2022), p. 253. DOI: 10.3390/universe8050253. arXiv: 2205.00940 [hep-ph].

[147] Francesca Calore and Christopher Eckner. "Lecture Notes: WISPs in gamma-ray astrophysics". In: May 2025. arXiv: 2505.12905 [astro-ph.HE].

[148] Juan Francisco Macias-Perez et al. "Global spectral energy distribution of the Crab Nebula in the prospect of the Planck satellite polarisation calibration". In: *Astrophys. J.* 711 (2010), pp. 417–423. DOI: 10.1088/0004-637X/711/1/417. arXiv: 0802.0412 [astro-ph].

[149] I. De Looze et al. "The dust content of the Crab Nebula". In: *Mon. Not. Roy. Astron. Soc.* 488.1 (2019), pp. 164–182. DOI: 10.1093/mnras/stz1533. arXiv: 1906.02203 [astro-ph.HE].

[150] J. Aumont et al. "Measurement of the Crab nebula polarization at 90 GHz as a calibrator for CMB experiments". In: *Astron. Astrophys.* 514 (2010), A70. DOI: 10.1051/0004-6361/200913834. arXiv: 0912.1751 [astro-ph.CO].

[151] A. A. Abdo et al. "Fermi Large Area Telescope Observations of the Crab Pulsar and Nebula". In: *Astrophys. J.* 708 (2010), pp. 1254–1267. DOI: 10.1088/0004-637X/708/2/1254. arXiv: 0911.2412 [astro-ph.HE].

[152] A. U. Abeysekara et al. "Measurement of the Crab Nebula at the Highest Energies with HAWC". In: *Astrophys. J.* 881 (2019), p. 134. DOI: 10.3847/1538-4357/ab2f7d. arXiv: 1905.12518 [astro-ph.HE].

[153] E. Aliu et al. "A Search for Enhanced Very High Energy Gamma-Ray Emission from the 2013 March Crab Nebula Flare". In: *Astrophys. J. Lett.* 781.1 (2014), p. L11. DOI: 10.1088/2041-8205/781/1/L11. arXiv: 1309.5949 [astro-ph.HE].

[154] J. Aleksić et al. "Measurement of the Crab Nebula spectrum over three decades in energy with the MAGIC telescopes". In: *JHEA* 5-6 (2015), pp. 30–38. DOI: 10.1016/j.jheap.2015.01.002. arXiv: 1406.6892 [astro-ph.HE].

[155] M. Amenomori et al. "First Detection of Photons with Energy Beyond 100 TeV from an Astrophysical Source". In: *Phys. Rev. Lett.* 123.5 (2019), p. 051101. DOI: 10.1103/PhysRevLett.123.051101. arXiv: 1906.05521 [astro-ph.HE].

[156] Zhen Cao et al. “Peta–electron volt gamma-ray emission from the Crab Nebula”. In: *Science* 373.6553 (2021), pp. 425–430. DOI: 10.1126/science.abg5137. arXiv: 2111.06545 [astro-ph.HE].

[157] M. Meyer, D. Horns, and H. -S. Zechlin. “The Crab Nebula as a standard candle in very high-energy astrophysics”. In: *Astron. Astrophys.* 523 (2010), A2. DOI: 10.1051/0004-6361/201014108. arXiv: 1008.4524 [astro-ph.HE].

[158] Ludmilla Dirson and Dieter Horns. “Phenomenological modelling of the Crab Nebula’s broadband energy spectrum and its apparent extension”. In: *Astron. Astrophys.* 671 (2023), A67. DOI: 10.1051/0004-6361/202243578. arXiv: 2203.11502 [astro-ph.HE].

[159] F. Aharonian et al. “Spectrum and extension of the inverse-Compton emission of the Crab Nebula from a combined Fermi-LAT and H.E.S.S. analysis”. In: *Astron. Astrophys.* 686 (2024), A308. DOI: 10.1051/0004-6361/202348651. arXiv: 2403.12608 [astro-ph.HE].

[160] K. G. Begeman, A. H. Broeils, and R. H. Sanders. “Extended rotation curves of spiral galaxies: Dark haloes and modified dynamics”. In: *Mon. Not. Roy. Astron. Soc.* 249 (1991), p. 523. DOI: 10.1093/mnras/249.3.523.

[161] Tongyan Lin. “Dark matter models and direct detection”. In: *PoS* 333 (2019), p. 009. DOI: 10.22323/1.333.0009. arXiv: 1904.07915 [hep-ph].

[162] S. Abdollahi et al. “Combined dark matter search towards dwarf spheroidal galaxies with Fermi-LAT, HAWC, H.E.S.S., MAGIC, and VERITAS”. In: (Aug. 2025). arXiv: 2508.20229 [astro-ph.HE].

[163] R. Abbasi et al. “Search for dark matter from the center of the Earth with 10 years of IceCube data”. In: *Eur. Phys. J. C* 85.5 (2025), p. 490. DOI: 10.1140/epjc/s10052-025-14144-7. arXiv: 2412.12972 [astro-ph.HE].

[164] R. Abbasi et al. “Search for High-Energy Neutrinos From the Sun Using Ten Years of IceCube Data”. In: (July 2025). arXiv: 2507.08457 [hep-ex].

[165] M. Aguilar et al. “Towards Understanding the Origin of Cosmic-Ray Electrons”. In: *Phys. Rev. Lett.* 122.10 (2019), p. 101101. DOI: 10.1103/PhysRevLett.122.101101.

[166] M. Aguilar et al. “Towards Understanding the Origin of Cosmic-Ray Positrons”. In: *Phys. Rev. Lett.* 122.4 (2019), p. 041102. DOI: 10.1103/PhysRevLett.122.041102.

[167] Ming-Yang Cui et al. "Possible dark matter annihilation signal in the AMS-02 antiproton data". In: *Phys. Rev. Lett.* 118.19 (2017), p. 191101. DOI: 10.1103/PhysRevLett.118.191101. arXiv: 1610.03840 [astro-ph.HE].

[168] Bernard Carr et al. "Constraints on primordial black holes". In: *Rept. Prog. Phys.* 84.11 (2021), p. 116902. DOI: 10.1088/1361-6633/ac1e31. arXiv: 2002.12778 [astro-ph.CO].

[169] Ciaran O'Hare. *cajohare/AxionLimits: AxionLimits*. https://cajohare.github.io/AxionLimits/. Version v1.0. July 2020. DOI: 10.5281/zenodo.3932430.

[170] Ronnie Jansson and Glennys R. Farrar. "A New Model of the Galactic Magnetic Field". In: *Astrophys. J.* 757 (2012), p. 14. DOI: 10.1088/0004-637X/757/1/14. arXiv: 1204.3662 [astro-ph.GA].

[171] Zhen Cao et al. "Ultrahigh-energy photons up to 1.4 petaelectronvolts from 12 γ-ray Galactic sources". In: *Nature* 594.7861 (2021), pp. 33–36. DOI: 10.1038/s41586-021-03498-z.

[172] Georg Raffelt and Leo Stodolsky. "Mixing of the Photon with Low Mass Particles". In: *Phys. Rev. D* 37 (1988), p. 1237. DOI: 10.1103/PhysRevD.37.1237.

[173] Igor V. Moskalenko, Troy A. Porter, and Andrew W. Strong. "Attenuation of vhe gamma rays by the milky way interstellar radiation field". In: *Astrophys. J. Lett.* 640 (2006), pp. L155–L158. DOI: 10.1086/503524. arXiv: astro-ph/0511149.

[174] Silvia Vernetto and Paolo Lipari. "Absorption of very high energy gamma rays in the Milky Way". In: *Phys. Rev. D* 94.6 (2016), p. 063009. DOI: 10.1103/PhysRevD.94.063009. arXiv: 1608.01587 [astro-ph.HE].

[175] Troy A. Porter et al. "Galactic PeVatrons and helping to find them: Effects of Galactic absorption on the observed spectra of very high energy γ-ray sources". In: *Phys. Rev. D* 98.4 (2018), p. 041302. DOI: 10.1103/PhysRevD.98.041302. arXiv: 1808.07596 [astro-ph.HE].

[176] Manuel Meyer, James Davies, and Julian Kuhlmann. "gammaALPs: An open-source python package for computing photon-axion-like-particle oscillations in astrophysical environments". In: *PoS* ICRC2021 (2021), p. 557. DOI: 10.22323/1.395.0557. arXiv: 2108.02061 [astro-ph.HE].

[177] Kazunori Kohri, Yutaka Ohira, and Kunihito Ioka. "Gamma-ray flare and absorption in Crab Nebula: Lovely TeV–PeV astrophysics". In: *Mon. Not. Roy. Astron. Soc.* 424 (2012), p. 2249. DOI: 10.1111/j.1365-2966.2012.21388.x. arXiv: 1202.6439 [astro-ph.HE].

[178] R. Buehler et al. "Gamma-ray Activity in the Crab Nebula: The Exceptional Flare of April 2011". In: *Astrophys. J.* 749 (2012), p. 26. DOI: 10.1088/0004-637X/749/1/26. arXiv: 1112.1979 [astro-ph.HE].

[179] Masanori Arakawa et al. "Detection of Small Flares from the Crab Nebula with Fermi-LAT". In: *Astrophys. J.* 897.1 (2020), p. 33. DOI: 10.3847/1538-4357/ab9368. arXiv: 2005.07958 [astro-ph.HE].

[180] S. S. Wilks. "The Large-Sample Distribution of the Likelihood Ratio for Testing Composite Hypotheses". In: *Annals Math. Statist.* 9.1 (1938), pp. 60–62. DOI: 10.1214/aoms/1177732360.

[181] Thomas Junk. "Confidence level computation for combining searches with small statistics". In: *Nucl. Instrum. Meth. A* 434 (1999), pp. 435–443. DOI: 10.1016/S0168-9002(99)00498-2. arXiv: hep-ex/9902006.

[182] Alexander L. Read. "Presentation of search results: The CL_s technique". In: *J. Phys. G* 28 (2002). Ed. by M. R. Whalley and L. Lyons, pp. 2693–2704. DOI: 10.1088/0954-3899/28/10/313.

[183] Luca Lista. "Practical Statistics for Particle Physicists". In: *2016 European School of High-Energy Physics*. 2017, pp. 213–258. DOI: 10.23730/CYRSP-2017-005.213. arXiv: 1609.04150 [physics.data-an].

[184] Samuel T. Spencer, Alison M. W. Mitchell, and Brian Reville. "Hadronic emission from the environment of the Crab Pulsar Wind Nebula by re-accelerated particles". In: (Apr. 2025). arXiv: 2504.08432 [astro-ph.HE].